Analysis of the feasibility of using GPS carrier phase ambiguity resolution techniques for precision approaches

Christophe Macabiau

THESE

présentée

pour obtenir

LE TITRE DE DOCTEUR DE L'INSTITUT NATIONAL POLYTECHNIQUE DE TOULOUSE

SPECIALITE: SIGNAUX, IMAGES ET COMMUNICATIONS

par

M. Christophe MACABIAU

ETUDE DE L'APPLICABILITE DES TECHNIQUES DE LEVER D'AMBIGUITE DE LA MESURE DE PHASE GPS AUX APPROCHES DE PRECISION

(ANALYSIS OF THE FEASIBILITY OF USING GPS CARRIER PHASE AMBIGUITY RESOLUTION TECHNIQUES FOR PRECISION APPROACHES)

Soutenue le: 29 Septembre 1997 devant le jury composé de:

MM. Gérard MARAL, professeur à l'ENST	président du jury
Gunter HEIN, directeur de l'IfEN, University FAF Munich	rapporteur
Igor NIKIFOROV, professeur à l'Université Technologique de Troyes	rapporteur
Abdelahad BENHALLAM, enseignant-chercheur à l'ENAC	examinateur
Francis CASTANIE, professeur à l'INPT	examinateur
Jean-Louis JONQUIERE, chef de la subdivision STNA3EN	examinateur
Gérard ALCOUFFE, chargé des affaires STNA à SEXTANT AVIONIQUE	examinateur

Remerciements

Je remercie Francis Castanié, chef de la formation doctorale 'Signaux Images et Communications', pour m'avoir accordé une bourse pour ce doctorat, et pour avoir contribué à la résolution des problèmes administratifs de début et de fin de thèse. Mes remerciements vont aussi à Abdelahad Benhallam, chef du LTST et directeur de cette thèse, pour la qualité de son encadrement, la grande confiance qu'il m'a accordée, et pour sa considérable capacité d'écoute.

Je remercie Raymond Rosso, directeur des études de l'ENAC, pour avoir fourni l'énergie nécessaire à la mise en place de ce travail, Patrick Dujardin, chef du département Electronique de l'ENAC, pour son aide indispensable lors de la résolution des problèmes administratifs, Lucien Mazet, adjoint au chef du département Electronique, pour sa gentillesse, la confiance qu'il m'a témoignée et son aide pour la compréhension des concepts physiques complexes, Max Moulin, chef de la subdivision Radionavigation de l'ENAC, pour ses conseils et la confiance qu'il m'a témoignée, Robert Aladenyse, adjoint au chef du département Electronique au début de cette thèse et retraité depuis, pour son aide très précieuse et sa grande générosité, Stéphane Puechmorel, enseignant-chercheur en mathématiques au département Mathématiques et Informatique de l'ENAC, pour nous avoir fait profiter si généreusement de ses connaissances infinies en mathématiques et en informatique, Guy Lagarrigue, chargé des relations extérieures de l'ENAC, pour son soutien et pour la confiance qu'il m'a témoignée. Je remercie aussi Bertrand Spitz, Jean Donan, Michel Valençot, Claude Peyrard, Jean-Claude Guilbard, Jean-Claude Gille, Jean-Luc Puech, Jean-Charles Doriac, Jacky Miger, Jean-Claude Cano, Gérard Wils, ingénieurs instructeurs à l'ENAC pour leur aide. Je remercie aussi Jean-Pierre Daniel, chef de la subdivision Télécommunications de l'ENAC au début de cette thése, pour son aide logistique. Mes remerciements vont aussi à Bernard Souny, chef de la subdivision Hyperfréquences de l'ENAC, ainsi qu'à Benoît Roturier son adjoint, pour leur aide dans la compréhension des phénomèmes de propagation. Enfin, je remercie Béatrice Busuldo pour son aide administrative. De plus, je tiens à remercier Mike O'Donoghue, professeur d'anglais à l'ENAC, pour son aide indispensable lors de la préparation des présentations orales en anglais.

Je remercie Jean-Claude Valentin, chef de la division STNA3, pour avoir accepté de contribuer financièrement à cette étude, Pierre Pinson, chef de l'échelon toulousain de la division STNA3 à Toulouse, pour avoir fait de même ici à Toulouse et pour avoir supporté mes exploits rugbystiques. Je remercie aussi Jean-Louis Jonquière, chef de subdivision STNA3EN, pour avoir apporté le support du STNA à ce travail et l'avoir si farouchement défendu à maintes reprises. Sans lui, ce travail aurait été impossible.

J'adresse aussi mes remerciements à Eric Chatre, ingénieur au STNA. Il peut être considéré comme étant le co-auteur de cette thèse, puisqu'il a brillamment organisé les travaux de cette étude, apporté sans cesse des idées neuves, des astuces diaboliques, et un réalisme qui fut notre garde-fou pendant tous les travaux. Enfin, il a su apporter l'énergie nécessaire pour démêler bon nombre de tracasseries administratives et m'assurer sans ambages de son soutien et de son amitié. Je remercie aussi Cyril Dupouy, ingénieur au STNA, puisqu'il a lui aussi énormément contribué à ces travaux, apportant des informations indispensables sur les systèmes GPS différentiels locaux, sur les récepteurs et le simulateur Nortel.

Je remercie aussi Christophe Dehaynain, chef de la subdivision STNA3EA, et Nicolas Warinsko, assistant au chef de subdivision STNA3EN, pour l'apport de leurs compétences aéronautiques aussi bien théoriques que pratiques. J'adresse aussi mes remerciements à Jean-Marc Liszez, ingénieur au STNA3, pour avoir accepté de manoeuvrer les avions et les satellites GPS aussi souvent. Je remercie

aussi Jean-Marc Caner, pour sa contribution à la collecte et à l'exploitation des mesures rélles, et à Patrick Calmejane pour son assistance sur les interprétations des exigences.

Je remercie aussi Charles Dussurgey, chef du département Etudes Amonts de SEXTANT AVIONIQUE, pour avoir défendu cette thèse au moment opportun. Mes remerciements vont aussi à Gérard Alcouffe, responsable des affaires STNA de SEXTANT AVIONIQUE, qui a accepté cette collaboration avec nous, et a apporté son expérience, sa compétence et ses idées brillantes à ce travail. Je remercie aussi Patrice Guillard, expert GPS de SEXTANT AVIONIQUE, qui est notamment à l'origine de la méthode MAPAS. Je remercie aussi beaucoup Sandrine Mazoyer, ingénieur d'étude à SEXTANT AVIONIQUE, pour avoir participé à de nombreux travaux de cette thèse. Elle a écrit la première version de MAPAS, et a contribué à son évolution tout au long de la thèse. Je remercie encore Marc Portier, ingénieur chez SEXTANT AVIONIQUE, pour ses remarques constructives sur les algorithmes de lever d'ambiguïté. Je remercie aussi Gilles Guillotel, ingénieur d'étude à SEXTANT AVIONIQUE, pour m'avoir guidé lors de mes premières lignes de code au pays des ambiguïtés. Je remercie aussi Gilles Garnier, responsable du projet Phase Tracking de SEXTANT AVIONIQUE, pour son aide à la compréhension des principes de fonctionnement des récepteurs SEXTANT. Je remercie Jean-Pierre Arethens, ingénieur d'étude SEXTANT AVIONIQUE, pour son aide lors de l'exploitation des données TOPSTAR ARINC. Je remercie enfin Michèle Poncelet, ingénieur d'étude de SEXTANT AVIONIQUE, pour son aide lors de l'écriture de l'algorithme de calcul de la position des satellites et Guy Goberthier, effectuant le support utilisateur chez SEXTANT AVIONIQUE, pour son aide lors des campagnes de mesure TOPSTAR.

Je remercie Jean-Luc Issler, chef du département Radionavigation du CNES, pour les informations inestimables qu'il m'a transmises sur le fonctionnement des récepteurs et sur le système GPS en général. Je remercie Felix Perosanz, ingénieur au CNES, qui m'a gentiment fourni de très précieux documents, m'éclairant lors des périodes de trou noir complet. Je remercie aussi Laurent Lestarquit, ingénieur au CNES pour ses explications sur la détermination du retard ionosphérique.

I gratefully acknowledge Dr. Gunter Hein, director of the Institute of Geodesy and Navigation of the University FAF, Munich, for accepting to review this thesis, and for his constructive remarks on the accuracy of AROF procedures.

Je remercie aussi Igor Nikiforov, professeur de l'Université Technologique de Troyes, pour avoir accepté d'être rapporteur de cette thèse, et pour avoir apporté ses réflexions mathématiques et philosophiques si profondes à ce travail.

I want to thank Mr. Oleg Stepanov, from the Central Scientific and Research Institute of Russia 'Electropribor', for his contribution to the analysis of LSAST and MAPAS, and for having translated, corrected and published one of my papers in the review 'Gyroscopy and Navigation'.

Je tiens aussi à remercier Gérard Salut, du LAAS, pour son apport très important sur la philosophie du traitement des mesures de phase.

Je remercie Zuheir Altamimi, de l'IERS, pour m'avoir fourni des informations indispensables sur la définition des référentiels d'espace.

Thomas Kukys, engineer at ELSAT, deserves my thanks for his kindness and for his great help in München.

Je tiens particulièrement à remercier Olivier Charleux, Isabelle Chane-Hai et Célia Pougnet, stagiaires DEA au LTST que j'ai encadrés, car ils ont eux aussi largement contribué aux travaux de cette thèse. Je remercie aussi Abdelrazak Younes, thésard au LTST, pour son aide et sa contribution aux réflexions présentées dans ce rapport.

Je remercie Béatrice Hacquard pour sa gentillesse et pour son aide.

Je remercie aussi Marie-Line pour sa patience, son aide, son amour, pour son soutien lors des difficultés occasionnées par le long travail effectué sur cette thèse. Je remercie maman pour son aide, sa compréhension, son amour, notamment lors des week-ends annulés pour travailler sur cette thèse. Je remercie aussi mamie et papi, en espérant que mamie ne m'en veut pas trop d'avoir manqué certains rendez-vous familiaux. Je remercie ma soeur pour sa grande aide pour les frappes de texte et pour les recherches d'emploi.

Je remercie ensuite Roger Bouchères, sans qui je n'aurais certainement pas fait cela, en tous cas pas dans les mêmes conditions. Il m'a beaucoup appris, et restera un exemple. Je remercie aussi très chaleureusement toute l'entreprise, y compris celui qui nous a quittés.

Je remercie aussi Marie-Claude pour son aide, sa compréhension, sa générosité. Je remercie Robert, qui est un sage et un guide, Josette pour sa gentillesse, et Jeannette pour l'exemple qu'elle nous donne.

Je remercie aussi Philippe Calcagno pour son amitié, son aide, malgré le peu de temps que nous avons passé ensemble pendant cette thèse. Je remercie Jean-Luc Testut pour m'avoir beaucoup appris, sa femme Nadine pour son entremise et son aide dactylographique, et tous mes ami(e)s que j'ai dû délaisser quelques fois pour ce travail et qui témoignent malgré tout de leur fidélité.

Abstract

The US Global Positioning System (GPS) provides an accurate positioning service anywhere in the world at any time, but its features are far from being sufficient for it to constitute the Global Navigation Satellite System (GNSS) expected by the civil aviation community. The horizontal accuracy is below 100 m 95% of the time, which is adequate for oceanic, enroute and non precision approaches phases of flight, although additional autonomous integrity monitoring is required to improve safety. The position estimate is computed by measuring the distance to all the visible satellites of the constellation, from the observations of pseudo random noise code modulations. When corrected using a ground reference station, the GPS code pseudorange measurements should provide an accuracy of a few meters. This is sufficient for low accuracy precision approaches (Category I), but guidance during the high accuracy precision approaches (Category II and III) requires the use of a sub-meter positioning system with a high integrity.

Since the beginning of the years 1980s, the GPS carrier phase measurements have been used in geodetic applications to pinpoint the location of the survey sites with a centimeter accuracy, after resolution of the intrinsic ambiguities of these measurements. Such techniques are attractive to the civil aviation community as they appear to have the accuracy required for its most demanding applications. However, as the ambiguity resolution process appears to be fragile especially in real-time kinematic applications, several questions remain unanswered about the reliability of these specific techniques, called AROF (Ambiguity Resolution On-the-Fly) procedures.

The aim of this study is to contribute to the analysis of the feasibility of using GPS carrier phase measurements ambiguity resolution procedures during precision aircraft landings. The starting point of this analysis is the presentation of the requirements for a GNSS based precision landing system, and the determination of a model for the carrier phase measurements. Then, the data pre-processing operations are reviewed, and the resulting quality of the data is assessed. Then, a classification of AROF procedures is proposed, and theoretical principles of several techniques, including the new MAPAS procedure developed during this study, are described. Next, the characteristics of AROF procedures are identified, enabling the determination of the requirements of AROF procedures. Afterwards, the difficulty of the determination of theoretical performance is discussed, and mathematical expressions of the performance parameters of MAPAS are presented. Next, the performance of AROF procedures is evaluated on a practical basis using simulated measurements, using measurements collected from a Nortel GPS signal generator, and using field measurements. Finally the characteristics are checked against the constraints, and a conclusion is drawn from this study.

Résumé

Le système américain GPS (Global Positioning System) fournit à tout utilisateur dans le monde entier un service de positionnement précis, mais ses caractéristiques sont trop éloignées de celles d'un GNSS (Global Navigation Satellite System) pour l'aviation civile. La précision atteinte est inférieure à 100 m 95 % du temps, et est suffisante pour les phases de vol océanique, en route, et pour les approches de non précision, mais une surveillance autonome complémentaire de l'intégrité est nécessaire pour améliorer la sécurité. L'estimation de position est effectuée en utilisant les mesures de distance entre l'utilisateur et les satellites visibles de la constellation GPS, obtenues grâce à l'observation des modulations de code pseudo-aléatoires du signal émis par les satellites. Après correction grâce aux données d'une station de référence, ces mesures de pseudo-distance de code devraient permettre un positionnement d'une précision de quelques mètres. Ceci est suffisant pour les approches de faible précision (Catégorie I), mais le guidage des avions pendant les approches de haute précision (Catégorie II et III) requiert l'utilisation d'un système de positionnement sub-métrique ayant une très grande intégrité.

Depuis le début des années 80, les mesures de phase de la porteuse du signal GPS sont utilisées lors des applications géodésiques pour déterminer précisément la position des points de mesure, avec une précision centimétrique après la résolution des ambiguïtés intrinsèques aux mesures de phase. De telles techniques sont attirantes pour l'aviation civile, puisqu'elles semblent avoir la précision nécessaire pour ses applications les plus exigeantes. Cependant, le processus de résolution des ambiguïtés s'avère fragile, surtout dans les applications dynamiques en temps réel, et des questions subsistent concernant la fiabilité des ces techniques spécifiques, appelées méthodes AROF (Ambiguity Resolution On-the-Fly).

Le but de cette étude est d'apporter une contribution à l'analyse de l'applicabilité des méthodes de lever d'ambiguïté de la mesure de phase GPS au guidage des avions en phase d'atterrissage de précision. Le point de départ de cette analyse est constitué par les exigences opérationnelles des systèmes d'atterrissage de précision basés sur un système GNSS, et par un modèle mathématique des mesures de phase GPS. Puis, les opérations de pré-traitement des mesures sont présentées, et la qualité des données obtenues est évaluée. Ensuite, on propose une classification des méthodes AROF, et on décrit les principes théoriques de plusieurs techniques, y compris de la méthode MAPAS, développée au cours de cette thèse. Puis, les caractéristiques des procédures AROF sont identifiées, permettant l'établissement des exigences. Puis, la difficulté de l'établissement des performances théoriques de ces méthodes est analysée, et des expressions mathématiques des performances de MAPAS sont présentées. Enfin, les performances de MAPAS sont évaluées sur un plan pratique, en utilisant des mesures simulées, des mesures collectées sur un générateur de signaux GPS Nortel, et des mesures réelles en situation aéroportuaire. Finalement, les caractéristiques de ces procédures sont comparées aux contraintes, et une conclusion est tirée de cette analyse.

Contents

Chapter 1

INTRODUCTION

In the beginning of the years 1980s, the *International Civil Aviation Organization (ICAO)* realized the increasing limitations of the current air navigation systems, and recognized the need for improvement. In 1983, the ICAO formed a new committee called the *Future Air Navigation Systems (FANS)*, and asked this group to study, identify and assess new concepts and techniques, and make recommendations for the coordinated development of air navigation in the next 25 years. The FANS committee analyzed the characteristics, potentials and difficulties of operation of the current *Communication*, *Navigation* and *Surveillance (CNS)* systems and understood their insufficiencies. In 1988, after four meetings, this committee proposed the development of new CNS means, and the elaboration of a new method for *Air Traffic Management (ATM)*. This proposition was called the CNS/ATM concept [FAN88].

Among the new solutions proposed by the FANS committee, the navigation concept is based on a worldwide position and time determination system : the *Global Navigation Satellite System (GNSS)*. This system is composed of one or several satellite constellations, of receivers installed in aircraft, of an integrity monitoring system, and it is augmented if necessary to satisfy the specific requirements of each phase of flight. The existing satellite navigation systems, *GPS (Global Positioning System)* and *GLONASS (GLObal NAvigation Satellite System)*, along with their augmentations, already provide an unchallenged positioning and timing service. Although the GPS positioning service is less accurate, it is far more used than GLONASS that still has to demonstrate its reliability, because GPS receivers are much more widely spread than GLONASS receivers. An increasing number of aircraft worldwide use this GPS information as an additional aid to find their way through the sky.

In both systems, the position of the user is determined through the measurement of distances between the receiver and several satellites of known positions. These distances are simply derived from measurements of the time of propagation of the signal from the satellite to the user. The propagation delays can be accurately estimated through the use of *pseudo random noise codes* modulating the signal carrier that provide obvious time marks to the receiver. The obtained horizontal accuracy is about 50 m 95% of the time with GLONASS, and around 100 m 95% of the time for users of the GPS Standard Positioning Service (SPS). Only authorized users of the GPS precise positioning service (PPS) can benefit from a 20 m horizontal accuracy 95 % of the time.

However, due to technical and institutional limitations, this service remains insufficient for the most demanding civil aviation applications. Apart from its lack of reliability, the nominal 100 m accuracy of the GPS standard positioning service is insufficient for guidance during landings. Dramatic improvement of this accuracy to a few meters can be obtained by the use of a *reference station* providing *differential corrections* to all the users in the service area. Although this accuracy can be

sufficient for many applications, precision landings call for the use of advanced solutions to reach the sub-meter accuracy required during the final part of the procedure.

In addition to the *code range measurements* presented earlier, *carrier phase measurements* can be made on the GPS signals. The carrier phase shift also contains range information, as its rotation is representative of the distance traveled since the transmission. However, this information is *ambiguous*, and proper exploitation of the geometrical information contained within the measurements requires the resolution of the *ambiguities*. Once achieved, this resolution helps refining the differential position and provides centimeter level positioning, thanks to the millimeter accuracy of the GPS carrier phase measurements. Until the end of the years 1980s, resolution of the ambiguities could be achieved only in static applications. Since then, new techniques have been developed, and ambiguities can be solved very quickly in real time even in mobile applications. A large diversity of experiments were conducted to examine the potential use of such techniques, including precision approaches.

It appears from experience that resolution of the ambiguities is a complex and fragile process, mostly because of its high sensitivity to the perturbations affecting the propagation, such as *atmospheric disturbances* and *multipath*. Thus, questions still remain about the true capacity of these methods in providing reliable accurate positioning information to landing aircraft, and many studies are being carried out to assess their performance [BHW94, WDR95].

The aim of the study presented in this report is the evaluation of the performance of GPS carrier phase *Ambiguity Resolution On-the-Fly (AROF)* techniques to help determine the feasibility of using these methods to guide aircraft during precision approaches. This study was performed by the *Laboratoire de Traitement du Signal et des Télécommunications (LTST)* of the *Ecole Nationale de l'Aviation Civile (ENAC)*, with the support of the *Service Technique de la Navigation Aérienne (STNA)* and of *SEXTANT AVIONIQUE*. The first part of the study consisted in the analysis of the theoretical principles of the most representative and promising methods. The analysis is essentially focused on a new technique, jointly developed by the LTST, the STNA and SEXTANT AVIONIQUE, called the *Maximum A Posteriori Ambiguity Search (MAPAS)* method. Then, characteristics of these techniques were identified and a theoretical analysis of performance was initiated, with a view to check the compliance of these methods with stringent civil aviation requirements. Afterwards, data collected from GPS receivers connected to a *Nortel GPS* signal simulator were analyzed, and finally evaluation from field measurements were performed.

This report is a synthesis of the work performed during this study. After this introduction, the requirements of a GNSS based precision landing system are presented in chapter two, with an explanation of the different parameters used to express the requirements. In chapter three, a model of carrier phase measurements is derived from the expression of the received signal. Then, in chapter four, the main pre-processing operations to be applied on the acquired data are presented, and their effect on the performance of the AROF procedure is emphasized. Next, in chapter five, a classification of AROF procedures is proposed, and theoretical principles of several techniques, including MAPAS are described. In the next chapter, the requirements of AROF procedures are determined by applying the constraints derived from the operational requirements on the identified characteristics of the AROF procedures. Afterwards, in chapter seven, the difficulty of the determination of theoretical performance is discussed, and expressions of the performance parameters of MAPAS are presented. In the next chapter, the performance of AROF procedures is evaluated on a practical basis using simulated measurements, then using measurements collected from a Nortel GPS simulator and finally from field measurements. At the end, the characteristics are checked against the constraints, and a conclusion is drawn from this study.

Chapter 2

OPERATIONAL REQUIREMENTS

This chapter introduces the parameters used to express the requirements for landing aids such as the *Instrument Landing System (ILS)* and the *Microwave Landing System (MLS)*. Then, the analysis is focused on the latest requirements issued for precision landing aids based on satellite navigation systems.

The civil aviation requirements for landing aids are issued by international organizations such as the International Civil Aviation Organization (ICAO) and its sub-committies. These requirements reflect the quality of the guidance service to be provided to the aircraft. The most demanding instrument approaches are those that require azimuth and glide path information and are called *precision approaches*. These approaches are divided into three main operational categories named *Category I, II* and *III (CAT I, II and III)*, defined according to different parameters, and in particular the level of confidence that can be placed by the pilot in the landing aid (see appendix A). Current precision landing aids include the Instrument Landing System (ILS) and the Microwave Landing System (MLS). Requirements for these systems are specified in [ICA96] and are recalled in appendix B.

The requirements for a GNSS based precision landing system have yet to be defined by ICAO. However, several propositions have been made, the latest of which was issued during the Working Groups meeting of the ICAO *Global Navigation Satellite System Panel (GNSSP)*, as reported in [ICA97]. The requirements stated are based on constraints imposed on the *Required Navigation Performance (RNP)* of the aircraft (see appendix C). The RNPs are expressed in terms of operational parameters such as *accuracy*, *integrity*, *availability* and *continuity of service* of the whole landing system (see appendix C). This defines volumes of expected position of the aircraft, also called *tunnels*, as presented in [ICA94a] and recalled in appendix D. The size of these volumes is defined by the maximum specified *Total System Error (TSE)*. The TSE represents the deviation between the true aircraft position and its desired flight path. This deviation is the composition of the *Navigation Sensor Error (NSE)* with the *Flight Technical Error (FTE)*, the latter representing the accuracy with which the aircraft is controlled using the information provided by the navigation sensor (see appendix D). The latest proposition of the ICAO GNSSP is presented in table 2.1.

It must be noted that the figures presented in table 2.1 specify the operational requirements of the landing system at the decision height associated with the landing category. The possibility to allow looser performance further away from the decision threshold is currently being discussed at an international level.

As we can see from table 2.1, the vertical accuracy requirements are very stringent. It is anticipated that code pseudorange differential corrections will provide the required CAT I accuracy, although the

Category	CAT I	CAT II	CAT III
RNP Type TSE 95 (Lat./Vert.)	0.02 Nm/40 ft (37 m/ 12 m)	0.01 Nm/15 ft (18.5 m/ 5.0 m)	0.003 Nm (5.6 m)
NSE 95% (Lat./Vert.)	18.2 m/4.4 m	6.5 m/1.7 m	3.9 m/0.8 m
Time-To-Alert	6 sec	1 sec	1 sec
Continuity risk	$1{\cdot}10^{-5}$ in any 15 sec	$8{\cdot}10^{-6}$ in any 15 sec	$6{\cdot}10^{-6}$ in any 30 sec
Integrity risk	$3.5{\cdot}10^{-7}$ per approach	$2.5{\cdot}10^{-9}$ per approach	$2{\cdot}10^{-9}$ per approach
Availability of Signal-In-Space	0.9975	0.9985	0.9990

Table 2.1: *Operational requirements on total CAT I/II/III landing equipment at corresponding decision height, as proposed in [ICA97].*

best integrity monitoring techniques are still to be developed. To fulfill CAT II and CAT III vertical accuracy requirements, it is necessary to use complementary techniques. As GPS carrier phase AROF procedures can provide centimeter level accuracy, they are good candidates to form the basis of such a system. However, it is necessary to evaluate their characteristics, and to compare them with the requirements presented in table 2.1.

Hence, carrier phase measurements are presented in chapter 3, then the principles of AROF procedures are described in chapter 5, characteristics are identified in chapter 6, and constraints on parameters are derived from table 2.1 in chapter 6.2.

Chapter 3

OBSERVATION MODELS

This chapter contains a determination of the mathematical models of the *code* and *phase pseudo-range measurements* based on the structure of the GPS signals and on the procedures of the measuring devices. It is assumed that fundamentals of GPS are known. In the other case, the reader can refer to publications such as [PSAE96], [LEI95] or [HWLC93] for example.

Estimation of the position of the user is achieved using the range measurements made by the receiver. These distance measurements are computed from the characteristics of the RF satellite signals collected by the antenna of the receiver. The user signals transmitted by the GPS satellites are two *spread spectrum* modulated carriers in the L-band. The range measurements are derived from the estimate of the time of propagation of these signals from the satellite to the antenna of the receiver. These propagation delays are measured using the code and phase tracking loops driven by the internal clock of the receiver, which are not synchronized with the satellite's clock. These clock offsets alter the range estimates, which are called pseudo-range measurements. In addition to these clock biases, several errors affect the code and phase pseudo-range measurements, such as *atmospheric perturbations*, *multipath propagation* and intentional degradation of accuracy, also called *Selective Availability (SA)*. In order to remove most of the errors affecting these observations, measurements from another receiver located in the same area are used.

3.1 Structure of GPS signal

The GPS satellites transmit two L-band carriers called *L1* and *L2* modulated by *binary data* and *pseudo random noise codes*. A model of the L1 and L2 signal radiated by the antenna of satellite i is presented in [SPI96a] and is recalled in equations (3.1) and (3.2).

$$S^i_{L1}(t) = \sqrt{2P}D^i(t)C^i(t)cos(2\pi f_1 t + \theta) + \sqrt{P}D^i(t)P^i(t)sin(2\pi f_1 t + \theta) \tag{3.1}$$

$$S^i_{L2}(t) = \sqrt{\frac{P}{2}}D^i(t)P^i(t)cos(2\pi f_2 t + \theta') \tag{3.2}$$

where

- P is the mean radiated power.
- D^i is the P/NRZ/L pulse coding of the 50 bps navigation message.
- C^i is the P/NRZ/L pulse coding of the C/A code. This code has a chip rate $f_c = \frac{1}{T_c}$=1.023 MHz.

- P^i is the P/NRZ/L pulse coding of the 10.23 Mbps P code. This public code is usually encrypted into the secret military Y code, and is called the P(Y) code.

- f_1=1575.42 MHz is the L1 carrier frequency and f_2=1227.6 MHz is the L2 carrier frequency. The associated wavelengths are $\lambda_1 \approx 19$ cm and $\lambda_2 \approx 24.4$ cm.

- t is the time in seconds, expressed in the satellite generated time scale. We can write

$$t = t_{GPS} - \Delta t_S^i \tag{3.3}$$

  where t_{GPS} is the time expressed in GPS time scale, and Δt_S^i is the satellite's clock offset.

- θ and θ' are respectively the angle equivalent calibration errors of the L1 and L2 channels. These terms are small phase noise and oscillator drift components.

Civilian GPS receivers usually track only one component of the L1 signal received from a particular satellite, composed of the carrier modulated by the data sequence and the C/A code, as other components are modulated by the unknown P(Y) code. However, special techniques can be used by so called *codeless* receivers to make measurements on these other components without knowledge of the P(Y) code, as presented in [LEI95]. These PRN code modulations allow *Code Division Multiple Access (CDMA)* to the signal of each satellite. The power spectral density of this signal is the result of the *spreading* of the 50 Hz data spectrum by the 1 kHz periodic C/A code clocked at 1.023 MHz. The power spectral density of the C/A component of the L1 signal is shown in figures 3.1(a), 3.1(b) and 3.1(c).

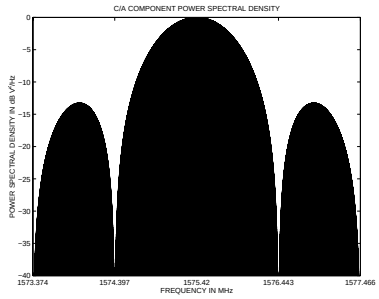

(a) *Power Spectral Density of C/A component of L1 signal.*

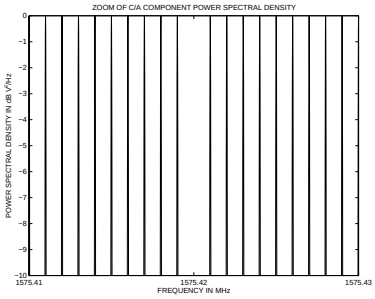

(b) *Detail of figure 3.1(a): the C/A spectrum is composed of the 50 Hz data spectrum repeated every kHz within the envelope shown in figure 3.1(a).*

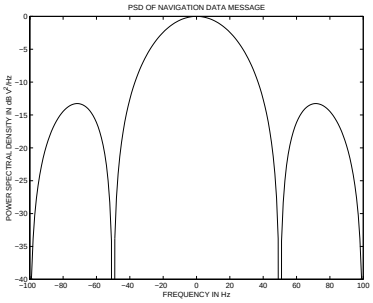

(c) *Power Spectral Density of navigation data message.*

Figure 3.1: *Power Spectral Density of C/A component of L1 signal.*

Using basic propagation theory as presented in [LEI95], a symbolic model of the C/A component of the received signal can be derived from (3.1) in order to introduce the group and phase propagation delays:

$$S_R(t) = \sqrt{2P}D(t - \tau_g)C(t - \tau_g)cos\left(2\pi f\left(t - \tau_\varphi\right) + \theta\right) + n_e(t) \tag{3.4}$$

where

- P is the power of the received C/A component. The minimum strength C specified at the output of a 0 dB gain antenna is C=-160 dBW [DoD95].

- t is the time in seconds expressed in the receiver time scale. We can write

$$t = t_{GPS} - \Delta t_U \tag{3.5}$$

  where t_{GPS} is the time expressed in GPS time scale, and Δt_U is the receiver clock offset.

- τ_g is the *apparent* time dependent *group delay* due to propagation along the actual distance ρ:

$$\tau_g = \frac{\rho}{v_g} + \Delta t_S^i - \Delta t_U \tag{3.6}$$

  where v_g is the *group velocity* and $\frac{\rho}{v_g}$ is the true group delay. This group delay is biased by the difference between the satellite and the receiver clock offset.

- τ_φ is the *apparent* time dependent *phase delay* due to propagation along the actual distance ρ:

$$\tau_\varphi = \frac{\rho}{v_\varphi} + \Delta t_S^i - \Delta t_U \tag{3.7}$$

  where v_φ is the *phase velocity* and $\frac{\rho}{v_\varphi}$ is the true phase delay. The apparent carrier phase shift is denoted $\varphi(t) = -2\pi f \tau_\varphi + \theta$.

- n_e is the noise affecting the signal collected by the antenna.

This shows that the propagation delay can be observed either on code phase shift τ_g or on carrier phase shift τ_φ. However, these two delays are not identical, as the group velocity differs from the phase velocity due to non linear variation of the propagation velocity as a function of frequency.

The overall frequency of the received carrier is

$$f(t) = \frac{1}{2\pi}\frac{d(2\pi f t + \varphi(t))}{dt} = f - f\frac{d\tau_\varphi}{dt} \tag{3.8}$$

Thus, variation of the phase delay over time changes the apparent frequency of the received carrier by an amount $f_d(t) = -f\frac{d\tau_\varphi}{dt}$, known as the *Doppler frequency offset*.

These code and carrier phase offsets τ_g and τ_φ are usually estimated using *code* and *phase tracking loops*, providing measurements for further determination of position. Nevertheless, it has been suggested by [SAL97] that straight optimal estimates of position and velocity could be directly obtained as components of the complete state vector through non linear filtering of the received signal with noise. Such an approach avoids the usual separation of the tracking loops and position estimation, merging them into a single estimation problem. To our knowledge, this technique has not been implemented in any receiver yet. A summary of this non linear filtering technique can be found in [CMMS97].

3.2 Structure of GPS receiver

A basic GPS receiver is designed to deliver in real time an estimate of the position, velocity and time of the user in a given space and time *reference frame*. The current GPS space reference frame was established in 1984 and is called the *World Geodetic System 1984 (WGS-84)*. The WGS-84 reference frame is defined in [DMA87]. It is used to express the ephemeris data of the GPS satellites broadcast in the navigation message. The GPS time scale is a generation of the *Universal Coordinated Time*

(UTC) achieved by a set of atomic clocks at the United States Naval Observatory (USNO). This practical time scale is called *UTC(USNO)*.

The organization of tasks in a GPS receiver is as illustrated in figure 3.2. The signal is collected, filtered and amplified by the antenna, then transmitted to the receiver through the RF cable. Afterwards, the signal is down-converted to intermediate frequency and sampled by the RF front end, processed by each tracking channel to extract raw code and carrier measurements as well as navigation data bits, which are finally processed to deliver position, velocity and time estimates.

Apart of the active antenna, its *Low Noise Amplifier (LNA)*, and the RF cable, a receiver is composed of three main parts :

- the RF section down-converts the amplified signal to a digital sequence.
- the specialized GPS chipset is an *Application Specific Integrated Circuit (ASIC)* that contains the specific code and phase tracking loops hardware for each channel.
- the microprocessor controls the tracking loops and processes the data to compute the position estimates.

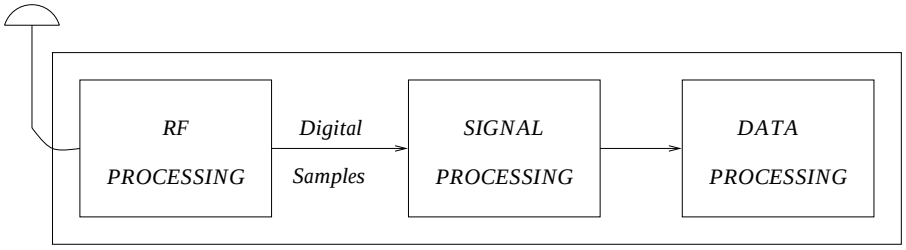

Figure 3.2: *Typical organization of tasks in a GPS receiver.*

As presented in section 3.1, the GPS signals are composed of *spread spectrum* modulated carriers. Thus, proper exploitation of these signals is performed through the use of a suppressed carrier *Phase Lock Loop (PLL)* like a *Costas loop*, and of a *Delay Lock Loop (DLL)*.

A PLL is a tracking device that continuously estimates the phase of a carrier. The main structure of an analog Costas loop is presented in figure 3.3.

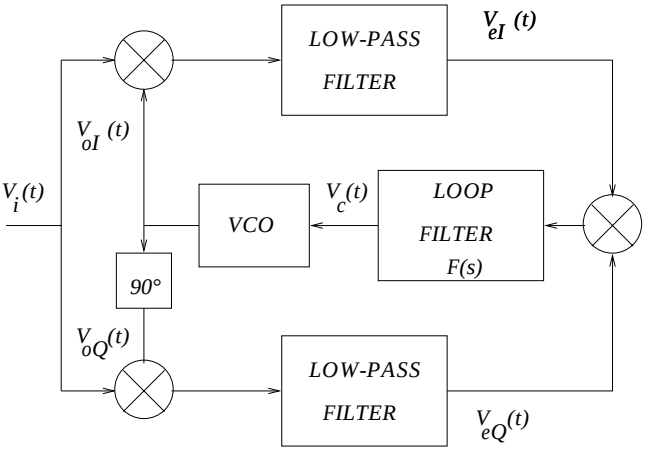

Figure 3.3: *Structure of an analog Costas loop.*

The incoming GPS signal, denoted $V_i(t)$ is modeled as :

$$V_i(t) = \sqrt{2P}C(t-\tau_g)D(t-\tau_g)sin\left(2\pi f(t-\tau_\varphi)+\theta\right)+n_i(t) \tag{3.9}$$

also noted

$$V_i(t) = \sqrt{2P}C(t-\tau_g)D(t-\tau_g)sin\left(2\pi ft+\varphi(t)\right)+n_i(t) \tag{3.10}$$

where

- t is the time in seconds expressed in the receiver time scale including the phase noise of the local oscillator.
- θ is the only phase bias modeled here, as it is assumed that other propagation delays experienced by the signal from the antenna to the PLL input line have no significant effect on the positioning accuracy. Indeed, most of these delays, including delays in the RF cable, are common to each satellite measurement and only affect the receiver clock offset estimate. Other delays within the receiver can be calibrated and compensated for in the settings of the tracking loops oscillators.
- $\varphi(t)$is the apparent phase shift due to propagation: $\varphi(t) = -2\pi f\tau_\varphi + \theta$.

This signal is mixed with an *In-phase (I)* and *Quadrature (Q)* replica of the output of the *Voltage Controlled Oscillator (VCO)* on each arm of the loop. The VCO delivers a sine wave with a center frequency set to the nominal carrier frequency, whose phase is the integrated value of the control signal $V_c(t)$:

$$V_{o_I}(t) = 2sin\left(2\pi ft + \int_{t_0}^{t} V_c(u)du + \frac{\pi}{2} + \varphi_L\right) \tag{3.11}$$

or equivalently

$$V_{o_I}(t) = 2sin\left(2\pi ft + \hat{\varphi}(t) + \frac{\pi}{2}\right) \tag{3.12}$$

where

- t is the time in seconds, expressed in the GPS time scale.
- $\hat{\varphi}(t)$ is the carrier phase estimate delivered by the VCO, with $\hat{\varphi}(t) = \int_{t_0}^{t} V_c(u)du + \varphi_L$.
- φ_L is the phase offset of the local oscillator combined with the initial value $\hat{\varphi}(t_0)$: $\varphi_L = \hat{\varphi}(t_0)$.

As shown for example in [HOL81], this loop has the ability to drive the local VCO so that it generates a signal with an equivalent unbiased phase estimate $\hat{\varphi}$ that matches the phase of the incoming signal with a resulting accuracy represented by the approximate phase uncertainty:

$$\sigma^2_{\varphi_e} = \frac{N_0 B_L}{C} \tag{3.13}$$

where

- $\varphi_e = \hat{\varphi} - \varphi$ is the phase estimation error.
- $C = P$ is the carrier signal power.
- N_0 is the value of the single-sided power spectral density of noise n_i
- $B_L = \frac{1}{2}\int_{-\infty}^{+\infty} \left|H_{LP}(f)\right|^2 df$ is the equivalent bandwidth of the loop where H_{LP} is the equivalent low-pass filter with Laplace transform: $H_{LP}(s) = \frac{F(s)}{1+\frac{F(s)}{s}}$ assuming all gains are set to 1. $F(s)$ is the central loop filter shown in figure 3.3

A typical value of N_0 is -205 dBW/Hz [SPI96a]. Therefore, for a minimum power signal C=-160 dBW, the phase tracking error with a 10 Hz loop bandwidth is σ_{φ_e}= 0.5 mm.

Using (3.11) and the definitions of $\varphi(t)$, $\hat{\varphi}(t)$ and the phase tracking error $\varphi_e(t)$, we derive:

$$\hat{\varphi}(t) = \int_{t_0}^{t} V_c(u)du + \varphi_L = -2\pi f \tau_\varphi + \theta + \varphi_e \tag{3.14}$$

Thus, the phase estimate is proportional to the phase propagation delay τ_φ. In consequence, the carrier phase tracking loop is the basic device for the elaboration of the *carrier phase observations* used in precise positioning, provided that the tracking error is kept within low values. As a result, the measurement accuracy is of the order of the phase tracking error φ_e.

Actual techniques to perform measurements integrate samples of the digital signal $V_c(t)$, that represents the Doppler shift of the received signal, as presented in figure 3.4.

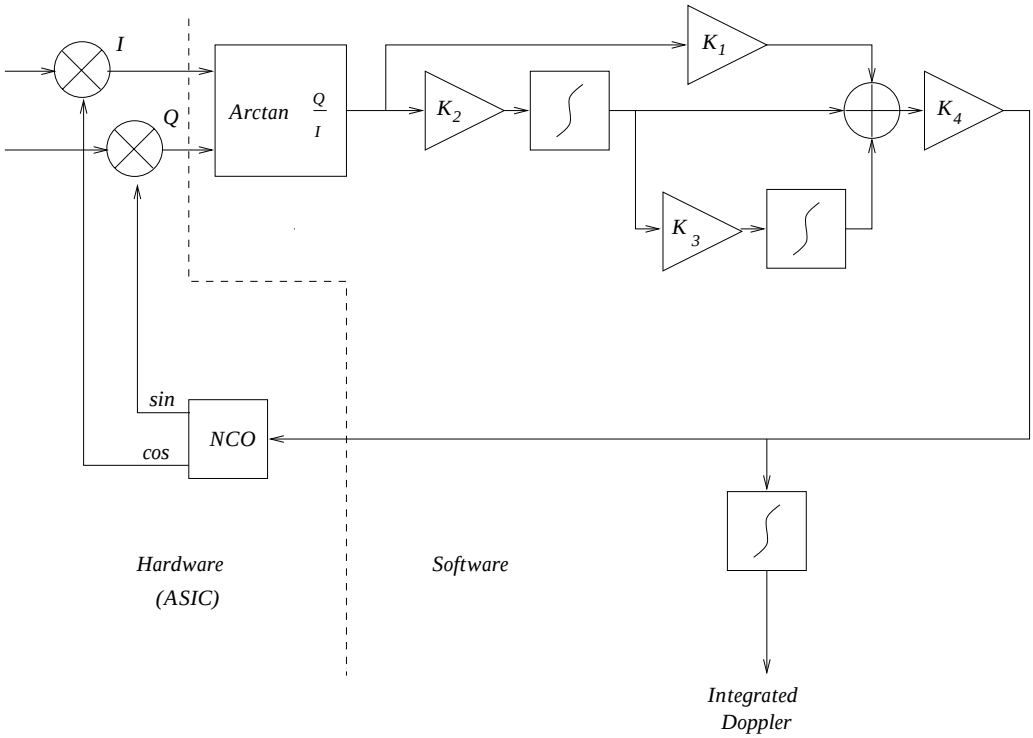

Figure 3.4: *Example of structure of a carrier phase tracking loop (courtesy SEXTANT AVIONIQUE).*

The phase measurement is initialized with the value $\hat{\varphi}(t_0)$ which is obtained as $\hat{\varphi}(t_0) = tan^{-1}\left(\frac{V_{o_I}(t_0)}{V_{o_Q}(t_0)}\right)$. Of course, determination of $\hat{\varphi}(t_0)$ is *ambiguous* because of the periodicity of trigonometric functions. Therefore $\hat{\varphi}(t_0)$ is biased by an unknown but fixed *integer number of cycles* N. This measurement bias is called the *ambiguity of the phase measurement*. The ambiguity is fixed at the initialization of the phase measuring device, and is constant over time as long as the PLL does not lose lock on the carrier.

The measurement value delivered at the observation epoch k is defined as:

$$\varphi(k) = \int_{t_0}^{t_0+kT_e} V_c(u)du + \hat{\varphi}(t_0) - 2\pi N \tag{3.15}$$

where T_e is the measurement sampling period.

Expanding (3.15) using the definition of φ_L and (3.14) , we get :

$$\varphi(k) = -2\pi f \frac{\rho}{v_\varphi} - 2\pi f(\Delta t_{S_i} - \Delta t_U) - 2\pi N + \theta + \varphi_e \tag{3.16}$$

This equation shows the relationship between the carrier phase measurement $\varphi(k)$ and the slant range ρ. Moreover, it emphasizes the fact that this measurement is biased by the relative offset of the satellite and user clocks, and by the integer ambiguity N. θ is usually neglected, as its value is very small and can be compensated using the parameters broadcast in the navigation message. When continuous tracking is achieved, φ_e appears as a phase measurement noise, with standard deviation σ_{φ_e}, as presented in (3.13).

Code phase tracking is achieved with a similar device, called a *Delay Lock Loop (DLL)*. Two types of DLLs can be implemented to track code phase, depending on whether the incoming signal has been converted to baseband or not. The first type of DLL is called a *coherent DLL*. Operation of a coherent DLL requires an estimate of the carrier phase for proper elimination before processing with the DLL. The other type of DLL is called a *non coherent DLL*.

The principle of a coherent DLL is illustrated in figure 3.5.

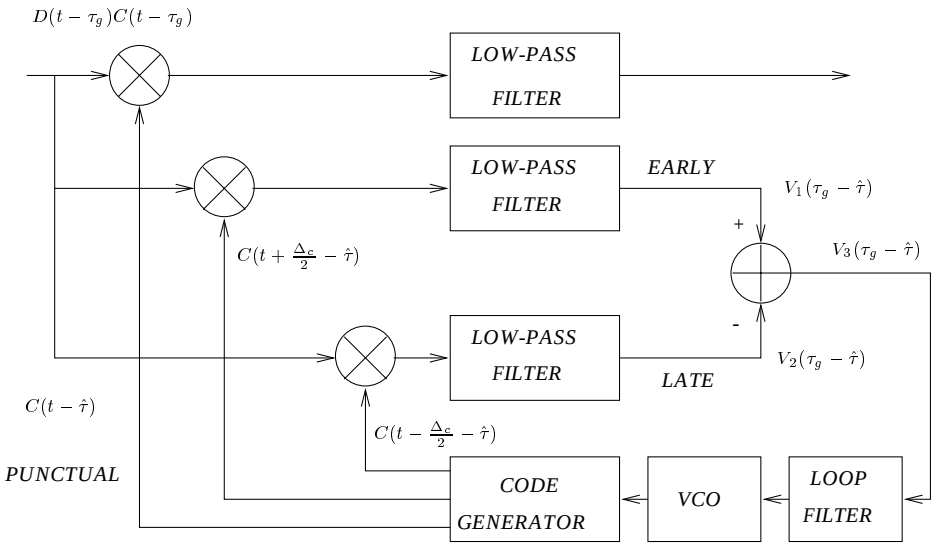

Figure 3.5: *Principle of a coherent DLL: Δ_c is the Early-Late time difference, also called Early-Late chip spacing. Classical receivers are designed with $\Delta_c = T_c$, but enhanced multipath rejection can be obtained when $\Delta_c < T_c$.*

The incoming code and data signals are correlated with early and late replicas of the code, driven by the control signal V_3. Lock is achieved when this control signal is zero, which is obtained for $\hat{\tau} = \tau_g$, as V_3 is linear around 0.

Code tracking can also be performed without demodulation of carrier signal. A typical non-coherent DLL is presented in figure 3.6.

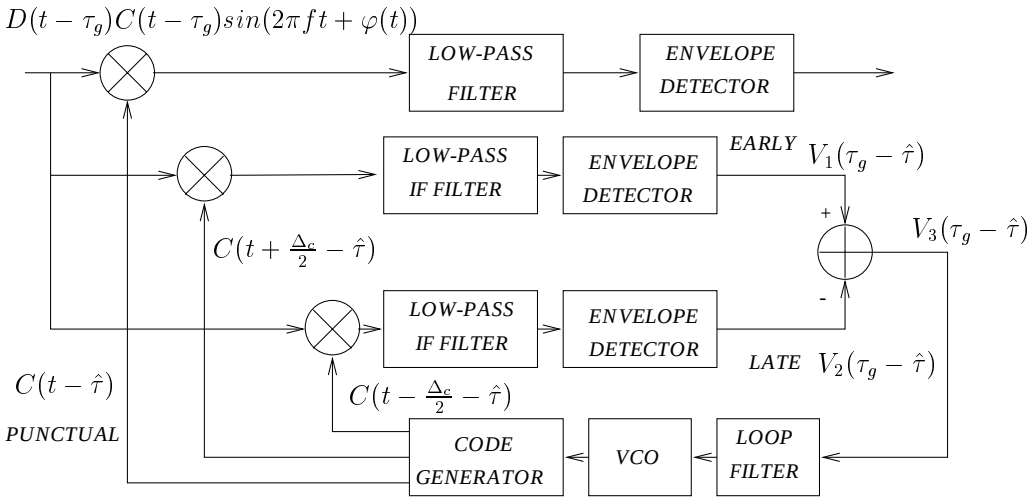

Figure 3.6: *Typical structure of a non coherent Delay Lock Loop (DLL).*

When the Early-Late chip spacing is $\Delta_c = T_c$ the performance of the coherent DLL is characterized by the variance [HOL81]:

$$\left(\frac{\sigma_{\tau_e}}{T_c}\right)^2 = \frac{N_0 B_N}{2C} \tag{3.17}$$

where

- $\tau_e = \hat{\tau} - \tau_g$ is the DLL tracking error.
- B_N is the equivalent closed loop noise bandwidth.

For example, in the previous case where $\frac{C}{N_0}$=45 dB Hz, if the noise bandwidth is B_N=3 Hz, the tracking error has a standard deviation $\sigma_{\tau_e} \approx$ 2m.

Similarly, when $\Delta_c = T_c$, the performance of the non coherent DLL is characterized by [HOL81]:

$$\left(\frac{\sigma_{\tau_e}}{T_c}\right)^2 = \frac{N_0 B_L}{2C}\left(1 + \frac{2N_0 B_{IF}}{C}\right) \tag{3.18}$$

where B_{IF} is the bandwidth of the intermediate frequency filter located on each arm of the DLL shown in figure 3.6. Using the same example, with an intermediate frequency filter bandwidth B_{IF}=10 kHz, the tracking error is $\sigma_{\tau_e} \approx$ 2.6 m.

In figures 3.5 and 3.6, $\hat{\tau}$ is the code propagation delay estimate, that can be expressed as :

$$\hat{\tau} = \tau_g + \tau_e \tag{3.19}$$

This model can be expanded using the expression of the group delay presented in (3.6):

$$\hat{\tau} = \frac{\rho}{v_g} + (\Delta t_{S_i} - \Delta t_U) + \tau_e \tag{3.20}$$

An example of integration of code and phase tracking loops in a receiver is presented in figure 3.7.

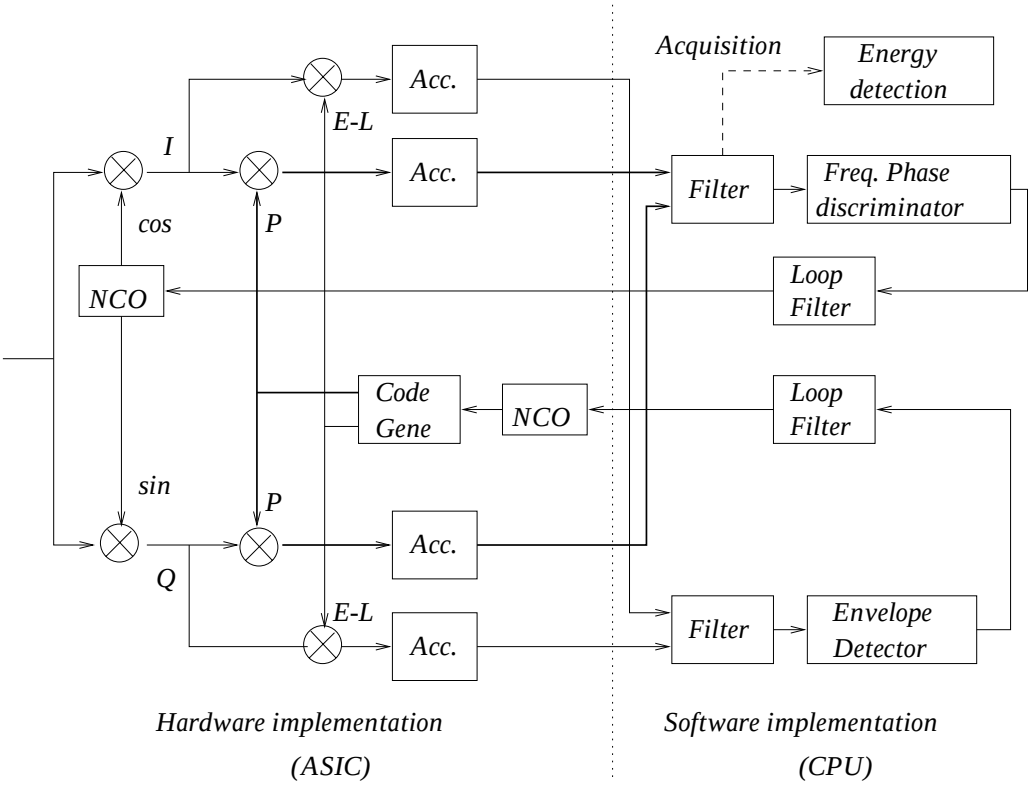

Figure 3.7: *Typical architecture of a modern GPS receiver.*

In the architecture presented in figure 3.7, only two copies of the code are generated : the Early minus Late (E-L) replica and the punctual (P) sequence.

3.3 Model of range measurements

Range measurements are elaborated using the estimate of the time of propagation that the code and phase tracking loops of the receiver are delivering.

As we saw in section 3.2 with equations (3.16) and (3.20), when lock is maintained, the tracking loops deliver estimates of the propagation delays, all biased by the difference between the local oscillator time offset and the satellite time offset. Thus, the code and carrier distance measurements made on satellite i at epoch k can be modeled as :

$$P^i(k) = c\tau_g^i(k) + c(\Delta t_u(k) - \Delta t_S^i(k)) + n^i(k) \tag{3.21}$$

$$\varphi^i(k) = -c\tau_\varphi^i(k) - c(\Delta t_u(k) - \Delta t_S^i(k)) + e^i(k) \tag{3.22}$$

The noise terms n^i and e^i represent the tracking errors of the DLL and of the PLL respectively. These errors are due to the noise affecting the signals fed to these synchronization modules. Therefore, they are modeled as random variables. It is usually assumed that these random variables have a Gaussian distribution. In addition, the code noise n^i is assumed independent from the phase noise e^i, as the synchronization process of the DLL is very different from that of the PLL. Furthermore, n^i and e^i are assumed to be white noise processes, uncorrelated over time.

The propagation velocities are dependent on the nature of the environment encountered by the wave during propagation. The main differences between group and phase velocities are due to the slight ionization of the *ionosphere*, as this medium contains ionized particles that have different effects

depending on the frequency of the signal. The different effects of the perturbations of the propagation experienced by the signal are usually modeled as delays, assuming that the propagation velocity, both for the modulation and for the carrier, is the vacuum speed of light.

Neglecting the second order effects as presented in[REM84], a first order model of the pseudo-range measurements can be expanded from (3.21) and (3.22) as :

$$P^i(k) = \rho^i(k) + c(\Delta t_u(k) - \Delta t^i_S(k)) + c(I^i(k) + \tau^i(k)) + SA^i(k) + D^i_{mult}(k) + n^i(k) \quad (3.23)$$

$$\varphi^i(k) = -\rho^i(k) + c(\Delta t^i_S(k) - \Delta t_u(k)) + c(I^i(k) - \tau^i(k)) - SA^i(k) + \varphi^i_{mult}(k) - \lambda N^i + \lambda b^i(k) \quad (3.24)$$

where

- I^i is the *ionospheric* delay in seconds. As seen in appendix G, the ionosphere delays the code and advances the phase.
- τ^i is the *tropospheric* delay in seconds. The influence of the troposphere can be considered as identical for code and phase measurements (see appendix H).
- SA^i is the intentional range measurement error due to the *Selective Availability*. It is identical on code and phase measurements.
- D^i_{mult} is the code pseudo-range measurement error induced by *multipath propagation*.
- φ^i_{mult} is the phase measurement error due to multipath propagation.
- λ is the L1 carrier wavelength.
- N^i is the carrier phase measurement *ambiguity*, constant over time as long as the PLL does not lose lock on the signal.

In order to take profit from the integer nature of the ambiguities, carrier phase measurements are usually expressed in units of cycles, dividing the previous quantities by the wavelength λ:

$$\varphi^i(k) = -\frac{\rho^i(k)}{\lambda} + f(\Delta t^i_S(k) - \Delta t_u(k)) + f(I^i(k) - \tau^i(k)) - \varepsilon^i_{SA}(k) + \varepsilon^i_{mult}(k) - N^i + b^i(k) \quad (3.25)$$

For one additive scattered ray, the measurement error D_{mult} induced by the multipath propagation of the signal can range from 0 m to 150 m in the worst case. Several techniques have been proposed to mitigate the effect of this perturbation as presented in [DB96] and [DOR97] and recalled in appendix E.

In the case of one specular ray, the measurement error $\varepsilon_{mult}(k)$ can be expressed as in (3.26), as presented in [BRA96] :

$$\varepsilon^i_{mult}(k) = \frac{1}{2\pi} arctan\left(\frac{\alpha^i(k) R\left(\tau^i(k) - \Delta\tau^i(k)\right) sin\left(\theta^i(k)\right)}{R\left(\tau^i(k)\right) + \alpha^i(k) R\left(\tau^i(k) - \Delta\tau^i(k)\right) cos\left(\theta^i(k)\right)}\right) \quad (3.26)$$

where

- $\alpha^i(k)$ and $\theta^i(k)$ are the relative amplitude and phase terms with respect to the direct ray
- $\Delta\tau^i(k)$ is the relative delay of the reflected signal
- $\tau^i(k)$ is the time equivalent pseudo-range measurement error
- R is the autocorrelation function of the C/A code

In the simple case of one specular ray, if we model the Earth's surface as a flat plate, the difference in path length between the direct and the reflected ray is δs

$$\delta s = 2h \sin\theta \text{ in meters} \tag{3.27}$$

where h is the height of the antenna above the ground and θ is the elevation angle of the satellite.

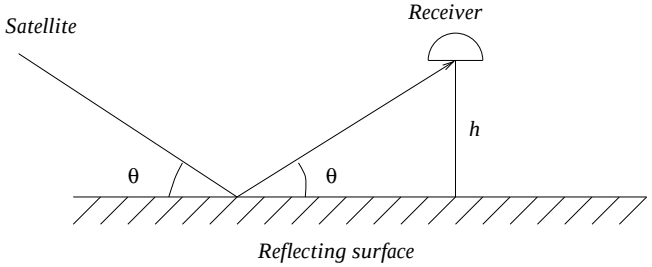

Figure 3.8: *Reflection of satellite signal on the Earth's surface*

Therefore, the lines of constant phase in space may be distorted as shown in figure 3.9.

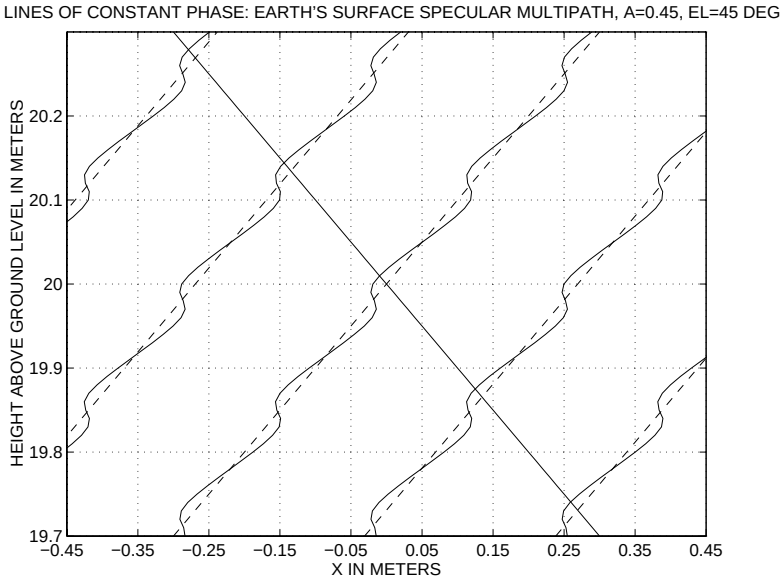

Figure 3.9: *Example of the deformation of the lines of constant phase in space in the case of one specular reflected signal from the Earth's surface. We chose here $\alpha = 0.45$, for a satellite with an elevation angle of 45^o. The curved continuous lines are the lines of constant phase resulting of the presence of the reflected signal, and are to be compared with the dashed lines in the ideal case. The straight line is the line of sight of the satellite.*

Using 3.26, it can be shown that, in the case of one specular reflected ray, the error $\varepsilon^i_{mult}(k)$ is bounded E:

$$-0.25 < \varepsilon^i_{mult}(k) < 0.25$$

Thus, this error will not cause a change in ambiguity, if left unmodeled. However, when several delayed signals interact, the error may be large enough to cause a full-cycle error and lead the ambiguity resolution procedure to raise wrong ambiguities.

Most of the ambiguity resolution procedures assume $\varepsilon^i_{mult}(k)$=0. We will examine the effects of this assumption on the performances of these methods in chapters 8 and 9.

As we saw in this chapter, access to the geometrical information using the code and phase measurements is difficult due to all the errors affecting these observations. Two approaches can be adopted to reduce the effect of these errors on the position estimate : the errors can be *estimated* or *compensated*.

Estimation of the errors can be made using models of the perturbations. Satellite clock errors and ionospheric delays can be estimated using the parameters broadcast in the navigation message. Tropospheric delays can be estimated using various models, such as published in [NAT93] or [SPI96b] (see appendix H). The receiver clock error can be estimated as an additional unknown. However, these estimates are not accurate enough as compared with the level of the carrier phase measurement noise. Thus, in practice, for precise positioning applications, these errors are canceled using measurements performed by another receiver located in the same area. Elimination of common errors is the fundamental principle of *differential GPS (DGPS)*, based on the fact that most measurement errors exhibit a large *correlation* in the position domain at the same time. For carrier phase processing, these techniques are extended to the definition of *single differencing* and *double differencing*.

Chapter 4

DATA PRE-PROCESSING METHODS

Once the carrier phase measurements are delivered to the navigation software, a few preliminary operations must be carried out on these observations to ensure that their format and their quality is sufficient for the AROF procedure to raise the correct ambiguities in a minimal number of epochs, and for the positioning module to estimate a precise position.

These preliminary operations are the synchronization of the reference and user data, single differencing, double differencing and detection and correction of cycle slips.

The data pre-processing operations are critical operations, and their quality is a driving factor for the performance of the AROF procedure.

4.1 Time-matching of user and reference data

The acquisition of measurements is triggered by signals that are proper to each receiver. Therefore, the data sent by the reference station characterize the errors at a time that differs from the time of the user measurements. In consequence, it is required to extrapolate the reference measurements to obtain a prediction of their value at the same time as the user measurements, as shown in figure 4.1.

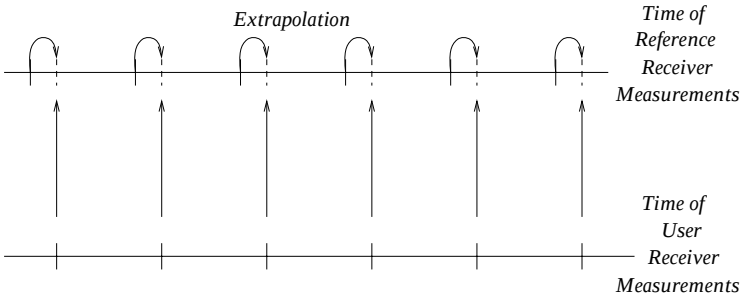

Figure 4.1: *Extrapolation of reference measurements* .

Several extrapolation techniques were tested, and the most efficient one was found to be a second order polynomial fitting for a data rate of 1 Hz.

4.2 Single differencing

In order to cancel most of the observation errors common to all the receivers performing measurements on the same satellites at the same time, a first set of quantities is computed called the *single*

differenced measurements. In our case, the user receiver uses measurements from a *reference station*, usually located on the ground on a surveyed point. These raw measurements are transmitted by the reference station to the mobile receiver through an RF data link. An illustration of the principle of computation of these single differences is presented in figure 4.2.

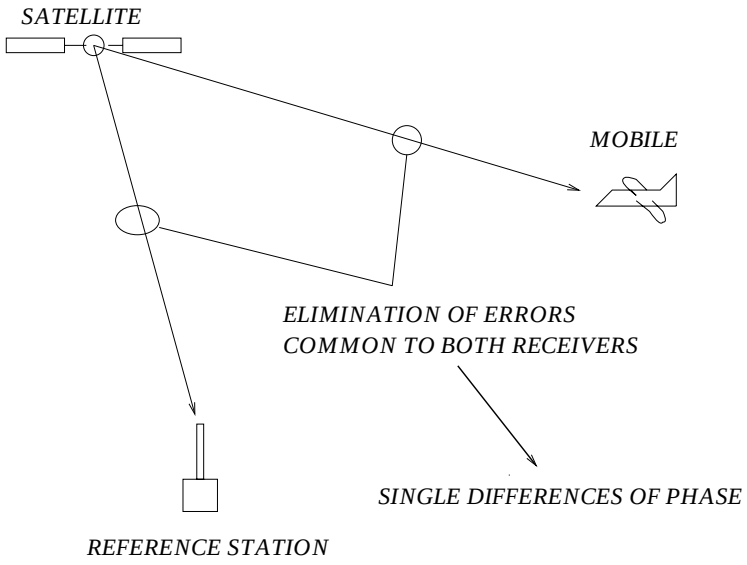

Figure 4.2: *Principle of single differencing.*

A model of these single differences is :

$$\begin{aligned}\Delta P^i(k) &= P_R^i(k) - P_U^i(k) \\ &= \Delta\rho^i(k) + c(\Delta t_{RU}(k) - \Delta t^i_{S_{RU}}(k)) + c(\Delta I^i(k) + \Delta\tau^i(k)) \\ &\quad +\Delta SA^i(k) + \Delta D^i_{mult}(k) + \Delta n^i(k) \end{aligned} \tag{4.1}$$

$$\begin{aligned}\Delta\varphi^i(k) &= \varphi_R^i(k) - \varphi_U^i(k) \\ &= -\frac{\Delta\rho^i(k)}{\lambda} + f(\Delta t^i_{S_{RU}}(k) - \Delta t_{RU}(k)) + f(\Delta I^i(k) - \Delta\tau^i(k)) \\ &\quad -\Delta\varepsilon^i_{SA}(k) + \Delta\varepsilon^i_{mult}(k) - \Delta N^i + \Delta b^i(k) \end{aligned} \tag{4.2}$$

where

- upperscript i denotes the satellite number
- subscripts R and U are used to denote respectively the Reference measurements and the User measurements,
- the Δ operator is used to symbolize the differentiation operation performed between the ground and the user quantities.

Cancellation or reduction of errors can only be achieved if differenced quantities are related to the same GPS time, and if these errors are highly correlated for both receivers.

As presented in section 4.1, time matching of measurements requires that a special re-synchronization procedure be operated between the reference and the user measurements, as measurement events are not identical for both receivers. Usually, this procedure performs an extrapolation of ground measurements at the time tags of the user measurements. Proper re-synchronization of measurements at reception times, through second order polynomial fitting for example, ensures that satellite clock

offset and *SA-dither* component are identical for both receivers if their relative distance is lower than 20 km (see appendix F).

Ionospheric propagation delays are usually highly correlated for separations lower than 10 km, depending on the solar activity (see appendix G). The correlation between both the tropospheric propagation delays decreases rapidly with the difference in height between the receivers (see appendix H). In order to reduce the amount of atmospheric residuals in the single differenced measurements, tropospheric and ionospheric errors are usually estimated from atmospheric models, and withdrawn from the user and reference measurements before single differencing.

Errors in the computation of the position of each satellite get projected on the user line of sight, and add up in the worst case, but induce small range errors if specific precautions are taken (see appendix I).

Thus, provided that proper compensation is achieved, satellite clock offsets and SA get canceled. The only remaining errors are the atmospheric residuals, the receiver clock offset and the multipath errors. However, as we can note in equations (4.1) and (4.2), the variance of the noise Δn^i and Δb^i is doubled. Thus, the model can be written as :

$$\begin{aligned} \Delta P^i(k) &= P_R^i(k) - P_U^i(k) \\ &= \Delta\rho^i(k) + c\Delta t_{RU}(k) + c(\Delta I^i(k) + \Delta\tau^i(k)) \\ &\quad + \Delta D_{mult}^i(k) + \Delta n^i(k) \end{aligned} \tag{4.3}$$

$$\begin{aligned} \Delta\varphi^i(k) &= \varphi_R^i(k) - \varphi_U^i(k) \\ &= -\frac{\Delta\rho^i(k)}{\lambda} - f\Delta t_{RU}(k) + f(\Delta I^i(k) - \Delta\tau^i(k)) \\ &\quad + \Delta\varepsilon_{mult}^i(k) - \Delta N^i + \Delta b^i(k) \end{aligned} \tag{4.4}$$

4.3 Double differencing

In order to remove the user receiver clock offset, differences of single differences can be computed. The resulting quantities are called the *double differences*. The most usual method is to subtract single differences of all satellites from single differences of one particular satellite called the *reference satellite*. The principle of computation of these double differences is illustrated in figure 4.3.

The reference satellite is usually chosen as the satellite with the highest elevation angle, as the probability of a distortion of the signal (atmospheric perturbation, multipath, ...) increases as the elevation decreases.

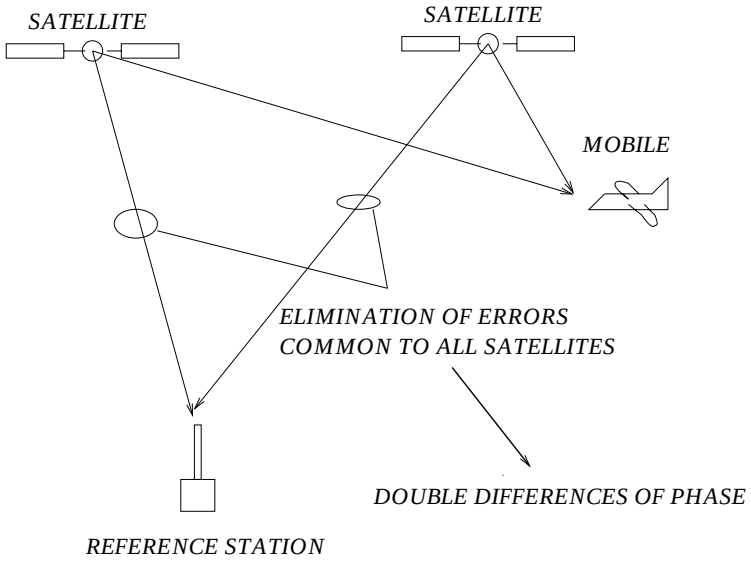

Figure 4.3: *Principle of computation of double differences.*

Assuming the reference satellite is satellite 1, a model of these quantities is as follows :

$$\begin{aligned} \nabla\Delta P^i(k) &= \Delta P^1(k) - \Delta P^i(k) \\ &= \nabla\Delta\rho^i(k) + c(\nabla\Delta I^i(k) + \nabla\Delta\tau^i(k)) + \nabla\Delta D^i_{mult}(k) + \nabla\Delta n^i(k) \end{aligned} \tag{4.5}$$

$$\begin{aligned} \nabla\Delta\varphi^i(k) &= \Delta\varphi^1(k) - \Delta\varphi^i(k) \\ &= -\frac{\nabla\Delta\rho^i(k)}{\lambda} + f(\nabla\Delta I^i(k) - \nabla\Delta\tau^i(k)) + \nabla\Delta\epsilon^i_{mult}(k) - \nabla\Delta N^i + \nabla\Delta b^i(k) \end{aligned} \tag{4.6}$$

The double differenced measurements are the observations used by the precise positioning algorithms to determine an accurate position of the user receiver. As we can see, these measurements are affected by atmospheric residuals $\nabla\Delta I^i$ and $\nabla\Delta\tau^i$, and by the double differenced multipath errors $\nabla\Delta D^i_{mult}$ and $\nabla\Delta\epsilon^i_{mult}$, that add up with the tracking noise n^i and b^i to distort the data.

Therefore, the resulting noise has a very complex distribution, which is in general very different from the distribution of $\nabla\Delta b^i$. However, most of the carrier phase processing algorithms assume that this resulting noise is a gaussian white noise stochastic process.

4.4 Detection and correction of cycle slips

As presented in section 3.2, the GPS carrier phase measurements are taken from the carrier phase lock loop. Therefore, the quality of these measurements is conditioned on the capability of the loop to track closely the evolutions of the phase of the carrier. Usually, the loop is able to follow rapidly these evolutions, and measurement errors are small. But in some cases, the loop may suddenly lose lock on the signal for a brief instant and re-acquire the signal very quickly after this. This problem, called a *cycle slip*, occurs when the signal is blocked by an obstacle, or when the dynamics of the mobile are too high for the tracking loop to follow. Such a phenomenon produces an abrupt jump in the carrier phase measurements, and can be modeled as a sudden change in the ambiguity from one measurement to the other. This change can have a very disastrous effect at two stages of the carrier phase processing. If the ambiguities are not solved yet, then an abrupt change of the ambiguity of a tracked satellite makes all the phase data on this satellite appear inconsistent, and the procedure will have a very hard time to achieve the resolution. If the ambiguities were already solved, then the

positioning module will suddenly use a false ambiguity value to determine the position of the mobile.

Therefore, it is mandatory to check the measurements fed to the carrier phase processing module for cycle slips. Detection of cycle slips on measurements made by a mobile receiver is difficult, because it may be hard to decide whether a change in the carrier phase measurement is due to a cycle slip or is due to a change in the distance between the satellite and the antenna. This detection is easier if the ambiguities are already solved because the redundancy check is more accurate. If cycle slips are detected, then it is important to estimate the value of the change in order to correct the phase measurements to be processed.

The analysis of the phase measurements cycle slips detection and correction techniques is not the main objective of the study presented in this report. However, several new techniques were analyzed and implemented, and are still undergoing development. We first tried to analyze the capability to detect and estimate cycle slips after the ambiguities are solved, and we are now developing software to detect and estimate cycle slips before the ambiguities are determined. Therefore, the main objective of this section is to present the principles of the detection and estimation of cycle slips. The details of the techniques developed during this study will be presented in future publications.

4.4.1 Cycle slips detection and estimation technique

The objective of the cycle slips detection and estimation techniques is similar to the objective of the integrity monitoring techniques such as those used in *Receiver Autonomous Integrity Monitoring (RAIM)* algorithms for example. The main goal is to detect the presence of cycle slips, then to isolate the channel affected by the problem, and finally to reconfigure the receiver for proper future exploitation.

Several methods for detection and estimation of cycle slips can be found in the literature. Some of them are only usable in static applications, like for example the efficient method presented in [BLE90]. In the dynamic case, the method presented in [LL92] performs a global approach, based on hypothesis testing of biases in Kalman filter innovations. However, the testing presented used this method is only based on the residuals observed at the current epoch. Therefore, we developed a technique based on the same basic principle, using a more optimal bias testing procedure, inspired on the technique presented in [VK96]. The testing procedures we have used are two sequential tests based on the computation of the likelihood ratio between the initial and the final distribution called the *CUmulative SUM (CUSUM)* test, and one of its adapted versions called the $\chi^2 - CUSUM$ test. These tests are not detailed here, as they can be found in numerous publications such as [PAG54] for the definition of the CUSUM test, and [NVK93, BN93] for modern developments. It was shown that both the CUSUM and the $\chi^2 - CUSUM$ test are asymptotically optimal in the sense that they minimize the worst case mean detection delay when the mean time before false alarms is infinite [NIK94].

The first developments made aimed at detecting and correcting cycle slips occuring after the ambiguities are solved. We are currently working on the development of a technique for detection and correction of cycle slips before the resolution of the ambiguities.

Each procedure is designed to work in the differential mode (DGPS), therefore the measurements processed are double differenced in order to remove most of the errors, as presented in section 4.3.

A model of these double differenced measurements is presented in (4.5) and (4.6). The cycle slip detection and correction procedure presented here assumes that the double differenced measurements

are only affected by tracking noise. In consequence the mathematical model is as follows:

$$\nabla\Delta P^i(k) = \nabla\Delta\rho^i(k) + \nabla\Delta n^i(k) \tag{4.7}$$

$$\nabla\Delta\varphi^i(k) = -\frac{\nabla\Delta\rho^i(k)}{\lambda} - \nabla\Delta N^i + \nabla\Delta b^i(k) \tag{4.8}$$

The cycle slips are modeled as sudden changes in the value of the ambiguities. Therefore, the ambiguities vary with time, and we can model the double differenced carrier phase measurements as:

$$\nabla\Delta\varphi^i(k) = -\frac{\nabla\Delta\rho^i(k)}{\lambda} - \nabla\Delta N^i + \nabla\Delta\tilde{N}^i(k) + \nabla\Delta b^i(k) \tag{4.9}$$

where

$$\begin{cases} \nabla\Delta\tilde{N}^i(k) = 0 \text{ if } \ k < k^i \\ \nabla\Delta\tilde{N}^i(k) = \delta N^i \text{ if } k \geq k^i, \text{ where } \delta N^i \in \mathbb{Z} \end{cases} \tag{4.10}$$

and k^i is the epoch of arrival of the cycle slip for satellite i, and δN^i is the associated jump.

The bias δN^i is an integer value, that can have a value as low as 1 cycle or several millions of cycles [LEI95].

When a cycle slip occurs on the carrier phase measurements of a particular satellite, only the measurements related to that particular tracking channel are affected. Therefore, this change only affects the double difference of that particular satellite, except if this satellite is the reference satellite. In that latter case, all the double differences are affected by the same cycle slip.

4.4.2 Detection and estimation of cycles slips occuring after resolution of the ambiguities

In this chapter, we try to detect and estimate the cycle slips that occur after the resolution of the ambiguities. The procedure designed detects a bias on the innovations delivered by a Kalman filter. The observations used by the Kalman filter are the unambiguous double differenced carrier phase measurements. The state of the system is composed of the position and velocity of the mobile. The state transition equation corresponds to the integrated random walk model presented in section L.

$$X_{k+1} = F_k X_k + W_k \tag{4.11}$$

$$Y_k = h(X_k) + V_k \tag{4.12}$$

where

- $X_k = [x_k, \dot{x}_k, y_k, \dot{y}_k, z_k, \dot{z}_k]$
- $Y_k = \Phi(k) + N$ where $\Phi(k) = [\nabla\Delta\varphi^2(k) \dots \nabla\Delta\varphi^{n_k}(k)]^T$ and $N = [N^2 \dots N^{n_k}]^T$, assuming satellite 1 is the reference satellite used to compute the double differences.
- $h(X_k) = -\frac{\nabla\Delta\rho^i(k)}{\lambda}$, as presented in appendix L
- F_k is the integrated random walk transition matrix presented in appendix L
- W_k is the state noise, with covariance matrix Q_k, as presented in appendix L
- V_k is the observation noise, with covariance matrix R_k, as presented in appendix L

At each epoch, the Kalman filter delivers the vector of the innovations I_k (see appendix L) to the cycle slip detection procedure:

$$I_k = Y_k - h\left(\hat{X}_{k+1|k}\right) \tag{4.13}$$

When no cycle slip is present, the innovation vector is centered. Note that this is only true as a first order approximation, as the extended Kalman filter is based on first order Taylor series expansion (see appendix L) although the system may not very closely follow that assumption. If a cycle slip occurs, the component of the innovation vector corresponding to the affected satellite is affected by a bias constant over time. The other components are affected by a small bias corresponding to the phase prediction error generated by the position error made by the filter, as one of the measurements is corrupted. If the cycle slip occurs on the measurements of the satellite used as a reference to compute the double differences, then all the components of the innovation vector are affected by the bias. In that case, detection fo the cycle slip may be very difficult.

Let's assume the tracking channel affected by the cycle slip does not correspond to the reference satellite. An example of the evolution of the innovation of that satellite is presented in figure 4.4.

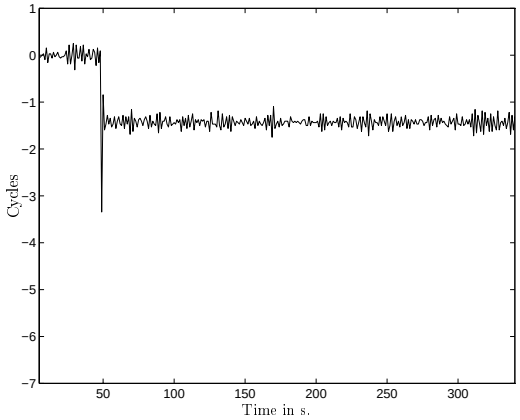

Figure 4.4: *Innovation of the double differenced carrier phase measurements of a satellite affected by a cycle slip of 2 cycles.*

A χ^2-CUSUM test is conducted on these innovations. The χ^2-CUSUM test is designed to test abrupt changes on a sequence of input data with the following assumptions:

- the data has an independent gaussian distribution with a known variance.
- the expected value of the data before the cycle slip occurs is well-known.
- the expected value of the data changes to an unknown value after the jump.
- the Kullback-Leibler distance between the initial and the final distribution is well-known (see appendix J).

In our case, the Kullback-Leibler distance between the two distributions is not known. Therefore, as our objective is to detect cycle slips of a minimal amplitude of 1 cycle, we designed the test for a Kullback-Leibler distance corresponding to that worst case. To perform the isolation function, as any channel can be affected by a cycle slip, we run $(N-1)$ tests in parallel, each one trying to detect a cycle slip on a particular double difference. The likelihood ratios obtained for each hypothesis are compared, and the channel associated with the maximum ratio larger than a predefined threshold is isolated as the affected channel.

Two different forms of this test were implemented:

- a χ^2-CUSUM test is run globally on the innovation vector to detect a possible bias in any of the components.
- a scalar χ^2-CUSUM test is run separately on each component of the innovation vector.

In both cases, the decision threshold is set so that the algorithm tries to detect at least a bias of one cycle on one innovation component.

Unfortunately, the results obtained using both of these χ^2-CUSUM test implementations were not satisfactory because the test had to be tuned to the specific value of the cycle slip affecting the measurements in order to have a sufficient efficiency.

4.4.3 Detection and estimation of cycles slips occuring before resolution of the ambiguities

Presentation of the method

The procedure presented here uses all the available measurements to try and detect any cycle slip occuring on the carrier phase measurements. Like the procedure described in section 4.4.2, this technique detects a bias on the innovations delivered by a Kalman filter. However, the observations used are the double differenced code and phase measurements, and the ambiguities are incorporated into the state of the system, in addition to the position and velocity components. As in section 4.4.2, the state transition equation used corresponds to the integrated random walk model presented in appendix L.

As the ambiguities are incorporated in the state of the system, they are continuously estimated. Therefore, when the change occurs, the filter is taken by surprise and will generate a biased innovation, which progressively returns to zero as the filter compensates the bias, as shown in figure 4.5(a).

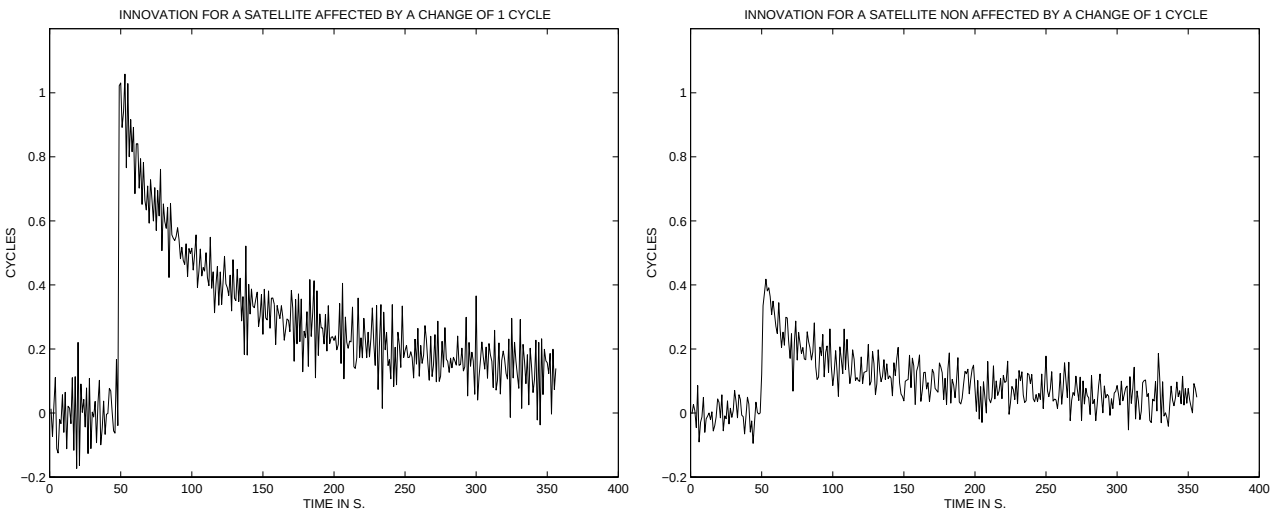

(a) *Innovation of the double differenced carrier phase measurements of a satellite affected by a cycle slip of 1 cycle.*

(b) *Innovation of the double differenced carrier phase measurements of a satellite not affected by the cycle slip of 1 cycle.*

Figure 4.5: *Evolution of two components of the innovation vector when a cycle slip occurs. The affected innovation exhibits a sudden change with an amplitude equal to the amplitude of the cycle slip. Then, the Kalman filter compensated the change. The innovations related to the other satellites are also affected, but to a smaller extent, depending on the geometry.*

We can see that the innovations do not present the general constant offset required as an assumption of the bias detection algorithms. Nevertheless, this bias has a significant amplitude for a long period, and detection by an algorithm such as the CUSUM test could be achieved. Tuning of the algorithm was possible, and the initial results are reported in the next section.

Preliminary results

A preliminary evaluation of the performance of the method proposed is carried out using simulations of the approach of an aircraft over the Toulouse-Blagnac airport. Measurements are generated using the computed positions of the satellites, and the simulated trajectory of the aircraft. The approach generated is a straight approach with a constant velocity of 70 m.s^{-1} initiated 20 Nm before the runway, and a cycle slip is inserted in one of the phase measurements 50 seconds after the beginning of the approach. The ability of the procedure to detect and estimate the bias is assessed by running these landing scenarios with an 8 second interval during 24 h for a total of 30 times. Therefore, this scenario was run for a total of 10801*30=324030 times.

Performance	Value
Probability of non detection	0
Detection delay	Min: 0 s Mean: 0.001 s Max: 5 s
Probability of False Isolation	3.10^{-7}
Probability of Isolation of Faulty Satellite at least with at least 3 satellites remaining	0.996
Probability of Proper Isolation	0.872
Probability of Correct Estimation of Cycle Slip	0.995

Table 4.1: *Preliminary simulation results for the capacity of detection and correction of cycle slips.*

These results can be compared to the operational requirements stated for the integrity and the continuity, presented in table 2.1. As the availability requirements for the carrier phase landing systems are not clearly defined, they are not taken into account in the present analysis.

The integrity risk was evaluated in the worst case where it is certain that a cycle slip occurs on 1 satellite signal during the approach. The integrity risk is defined as

$$\text{Integrity Risk} = 1 - P[\text{Isolation of affected channel at least}] \tag{4.14}$$

The continuity risk is the sum of the probability of occurence of a false alarm and the probability that fewer than 4 satellites remain after isolation of faulty signals. Therefore we can write:

$$\text{Continuity risk} = P[\text{Number of remaining satellites} < 4 \text{ after isolation}] + P[\text{False Alarm}] \tag{4.15}$$

Required Performance				Observed value
Category	CAT I	CAT II	CAT III	
Max Detection delay	6 s	1 s	1 s	5 s
Integrity Risk	$3.5{\cdot}10^{-7}$	$2.5{\cdot}10^{-9}$	$2{\cdot}10^{-9}$	$3{\cdot}10^{-3}$
Continuity Risk	$1{\cdot}10^{-5}$	$8{\cdot}10^{-6}$	$6{\cdot}10^{-6}$	$7.19{\cdot}10^{-2}$

Table 4.2: *Comparison of initial results with required performance.*

As we can see from table 4.4.3, the observed performance is good, although it remains far away from the operational requirements. However, several limits to this conclusion must be drawn. First of all, the jump simulated in all the landing scenarios has an amplitude of 1 cycle, which is the smallest possible value. Morevover, the integrity and continuity risks were calculated in a worst case scenario where a cycle slip always occurs during the approach. On the other hand, these results are based on simulations that are incomplete, as the approach path is straight with a constant velocity, and no perturbation such as multipath or atmospheric decorrelation were added.

Chapter 5

PRINCIPLES OF AROF PROCEDURES

Ambiguity Resolution On-the-Fly (AROF) procedures determine the ambiguities of the double differenced phase measurements made by a moving receiver. The solved ambiguities provide the basis for centimeter level positioning of the receiver. Since the design of the first resolution procedures, the mathematical approaches adopted to achieve this determination have gone from *integer searching* to *integer estimation* using specific optimization techniques. Based on this evolution, this chapter presents a proposed classification of AROF procedures. Then, four procedures are described, namely the Least Squares Ambiguity Search Technique (LSAST) [HAT91], the Maximum A Posteriori Ambiguity Search (MAPAS) [MAC95], the Fast Ambiguity Search Filter (FASF) [CHE95] and the Direct Integer Ambiguity Search (DIAS) [WS95].

5.1 Classification of AROF procedures

The ambiguities affecting the carrier phase measurements performed by a GPS receiver prevent the access to the geometrical information contained within these measurements. Elimination of these ambiguities can be achieved through time differentiation of the measurements. The resulting observations are called the *triple differences*, and do not include the ambiguities. However, in the dynamic case, processing the triple differences to determine the position is complex because they depend on the time derivatives of the user position. Another technique to determine the position of a mobile consists in solving the equation model for the ambiguities. This approach lead to the elaboration of numerous ambiguity resolution procedures since the beginning of years 1980.

The problem of the resolution of the ambiguities is a general problem of *statistical inference* where we need to process some observation to extract information from it. Upon examination of all the techniques proposed for resolution of the ambiguities, it appears that two distinct approaches were adopted. These two approaches correspond to the two major areas of statistical inference, which are *decision theory* and *estimation theory*. In the first case, a decision is taken among some finite number of possible situations, while in the second case an estimate of a quantity that is not observed directly is computed [TRE68, POO94].

This distinction can provide the basis for a classification of AROF procedures. These procedures process the double differenced carrier phase measurements presented in section 4.3 with the simplified model 4.6 recalled here:

$$\nabla\Delta\varphi^i(k) = -\frac{\nabla\Delta\rho^i(k)}{\lambda} + \nabla\Delta\epsilon^i_{mult}(k) + f(\nabla\Delta I^i(k) - \nabla\Delta\tau^i(k)) - \nabla\Delta N^i + \nabla\Delta b^i(k) \quad (5.1)$$

The procedures that adopt the decision approach, like the Ambiguity Function Method (AFM) [REM91, MAD92], the Least Squares Ambiguity Search Technique (LSAST) [HAT91, LCL92], the Maximum A Posteriori Ambiguity Search (MAPAS) method [MAC95] and the Ambiguity Resolution using Constraint Equation (ARCE) [PKLJ97] are *multiple hypotheses tests* that check thousands of *integer combinations* to find the most consistent one.

On the other hand, estimating procedures, like the Fast Ambiguity Search Filter (FASF) [CHE95], the Direct Integer Ambiguity Search technique (DIAS) [WS95] and the Fast Ambiguity Resolution Approach (FARA) [FB90] use the measurement model 5.1 presented in section 4.3 to estimate in two stages the best integer vector. The vector is first estimated as a floating point quantity, then fixed using specific procedures based on integer optimization theory, such as the Lambda method [TEU94] or the technique based on the optimized Cholesky decomposition method presented in [LE92] for example. A specific class of ambiguity estimating procedures are the methods that only make the first estimation step, providing a good floating point estimate of the ambiguities that enables the receiver to reach decimeter-level positioning after a few seconds. The first class of estimating procedures is referred herein as *integer estimating* procedures, and the second one is called *float estimating procedures*. In this report, float ambiguity estimation procedures have not been studied.

The proposed classification of AROF procedures is summarized in table 5.1.

Decision	Integer Estimation
AFM	FARA
LSAST	DIAS
MAPAS	FASF
ARCE	

Table 5.1: *Proposed classification of AROF procedures.*

However, integer estimating procedures can be viewed as decision-making techniques, considering that any integer estimating procedure comes with a final *validation stage* that has the structure of a multiple hypothesis sequential test, as the best candidates are sorted and tested for consistency for several epochs before the election of the best one.

The principle of AROF procedures is to extract the ambiguity information from the double differenced observations that are corrupted by the measurement errors and noises. In the next sections, the LSAST and MAPAS methods are presented as examples of decision techniques, and the DIAS and FASF methods are presented as examples of integer estimation techniques.

5.2 LSAST and MAPAS: two decision making techniques

The concept of the Least Squares Ambiguity Search Technique (LSAST) was first presented in [HAT91] and reformulated in [LCL92]. The Maximum A Posteriori Ambiguity Search (MAPAS) method, jointly developed by SEXTANT AVIONIQUE, the French Service Technique de la Navigation Aérienne (STNA) and the LTST is a method for ambiguity resolution on-the-fly inspired from the technique presented in [BH84], which is based on the same principles as the LSAST.

These two procedures perform an active search of the value of the double differenced ambiguities of four particular satellites called the *primary satellites*. They both are multiple hypotheses sequential tests that process as many carrier phase measurements as necessary to isolate the best candidate in a predetermined set of *three-integer combinations*. However, the LSAST and MAPAS methods use different decision criteria to check the hypotheses: the LSAST is based on the *weighted sum of the*

squared prediction errors obtained for the tested combination, while the MAPAS method uses the *a posteriori probability* of this candidate, conditionally on the prediction errors obtained for that candidate.

Thus these two algorithms have the same overall structure and only differ by the steps performing the calculation of the decision criterion. This results in different implementation constraints and running capabilities. Both of them can raise ambiguities in seconds when the data conforms to the mathematical model employed. However, they show different performances when applied to data affected by unmodeled noise such as multipath.

The measurements used by LSAST and MAPAS are the double differenced phase observations made by the user receiver formed using the observations obtained by a reference receiver as depicted in figure 5.1.

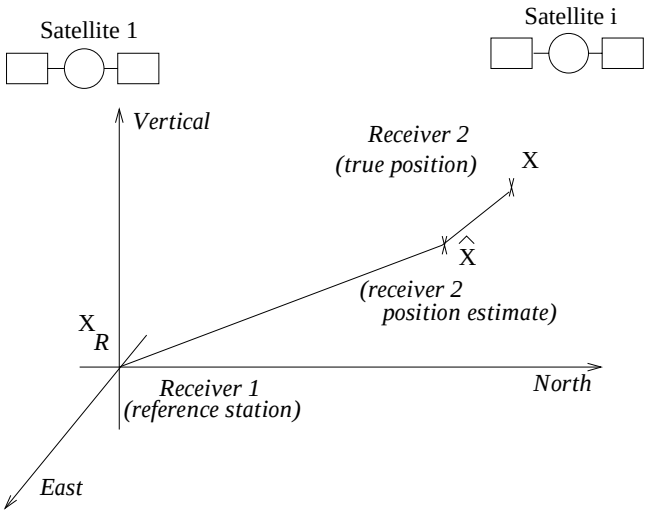

Figure 5.1: *Illustration of the situation of the receivers in a local coordinate system.*

These observations were presented in section 4.3, in equation 5.1. However, both of these procedures assume that the measurements are not affected by multipath and that atmospheric residuals are properly compensated, thus that $\nabla\Delta\epsilon^i_{mult}(k) = 0$ and $\nabla\Delta I^i(k) = 0$, $\nabla\Delta\tau^i(k) = 0$. Of course, these assumptions do not correspond to reality in general, as multipath and atmospheric residuals distort the distribution of the noise. Therefore, in most of the cases, the measurement model is not adapted to reality. The influence of the inadequacy of these assumptions will be evaluated in chapters 8 and 9.

$$\nabla\Delta\varphi^i(k) = -\frac{\nabla\Delta\rho^i(k)}{\lambda} - \nabla\Delta N^i + \nabla\Delta b^i(k) \tag{5.2}$$

In reality, multipath errors and atmospheric residuals will be accounted for in the error term $\nabla\Delta b^i(k)$, although the assumed distribution does not correspond to the complex distribution.

These double differenced measurements are linearized around a position estimate $\hat{X}(k)$, generally obtained by the use of DGPS (see appendix K).

A vector model of these quantities is

$$\Phi(k) = -C(k)\delta X(k) - N + B(k) \tag{5.3}$$

where

- n_k is the number of visible satellites at epoch k
- $\Phi(k)$ is the vector of the $(n_k - 1)$ double differenced carrier phase measurements.

- $\delta X(k)$ is the 3×1 vector of the position estimation error: $\delta X(k) = \hat{X}(k) - X(k)$.
- N is the $(n_k - 1) \times 1$ vector of the double differenced ambiguities.
- $C(k)$ is the $(n_k - 1) \times 3$ vector of the *direction cosines*.
- $B(k)$ is the $(n_k - 1) \times 1$ vector of the phase measurement noise.

The linear model given in (5.3) is the mathematical model used by both the LSAST and MAPAS methods.

Once the measurements are linearized, the problem of the resolution of the double differenced ambiguities can be illustrated as in figure 5.2. We need to search the best position around the inital position estimate such that the surfaces of constant double differenced carrier phase measurements intersect as closely as possible. At each epoch, several candidates can be isolated, where the surfaces intersect almost perfectly. But after several epochs, only one candidate has been gathering the surfaces around itself. This point is the true solution.

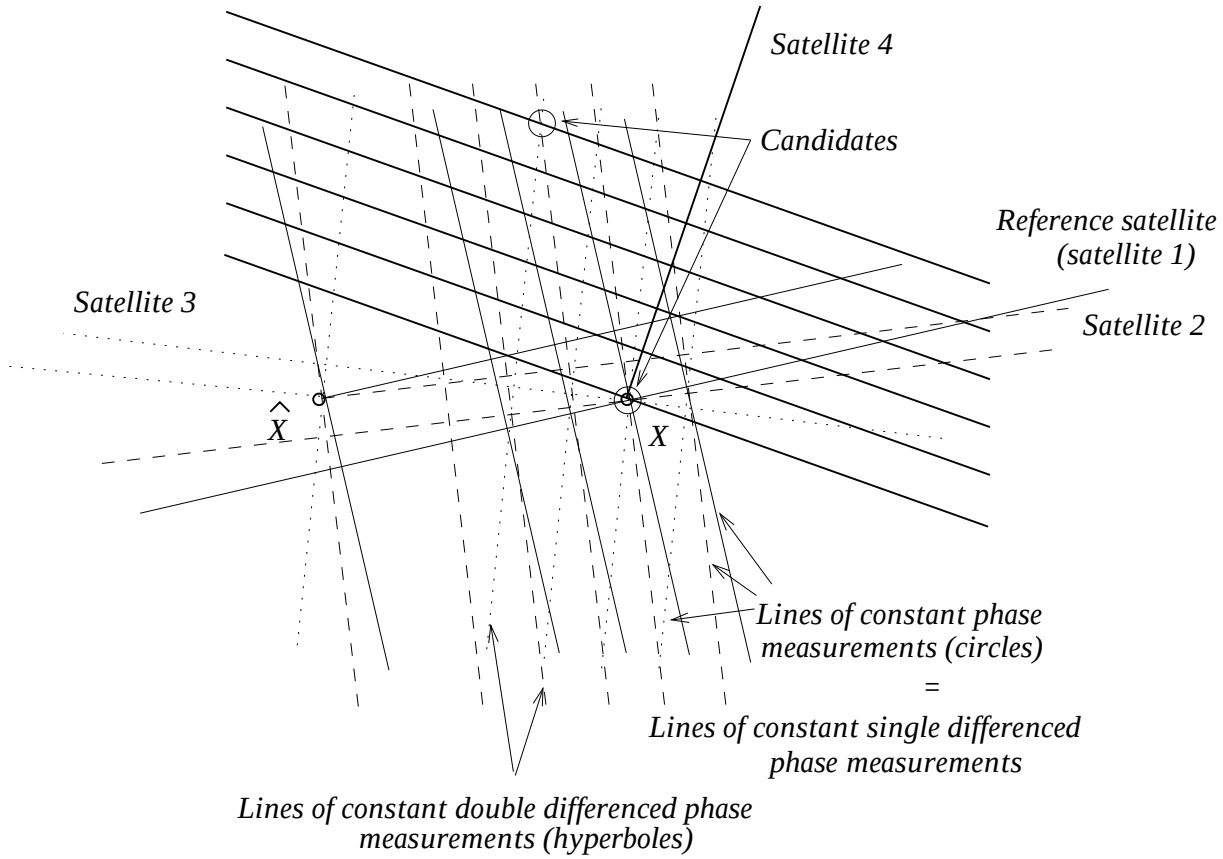

Figure 5.2: *Illustration of the problem of ambiguity resolution in a two dimensional case.*

As the observations are affected by measurement errors, the emergence of the solution may not be clear. If these errors are distributed as white noise with known variance, then by searching the candidate yielding the most improbable prediction errors, we can isolate the true solution after collecting several measurements. However, if the noise samples are time-correlated, then the same error may appear several times, and a false solution may accidently emerge.

5.2.1 Common principles of LSAST and MAPAS

The determination of the position is conditioned on the resolution of the double differenced ambiguity vector N. This resolution is done by testing thousands of possible values of N. These values are determined as the integer vectors associated with a position contained within a predefined search volume. This search volume is centered around the position estimate $\hat{X}(k)$, and its size depends on the uncertainty of that estimate.

The size of the trial set can be reduced if we note that only three of these ambiguities are independent in the noise-free model derived from (5.3). Thus the procedure looks for the best three-integer combination to be affected to the double differenced ambiguities of four particular satellites.

These satellites, called the primary satellites, are chosen according to their degree of visibility and their *Position Dilution Of Precision (PDOP)* factor. They must stay visible as long as the resolution is not done, and their PDOP must not be too low nor too large, to guarantee a small computation time and a sufficient integrity. Indeed, in a given search volume the number of candidates increases when the PDOP decreases, as depicted in figure 5.3. Therefore, if we choose the primary satellites

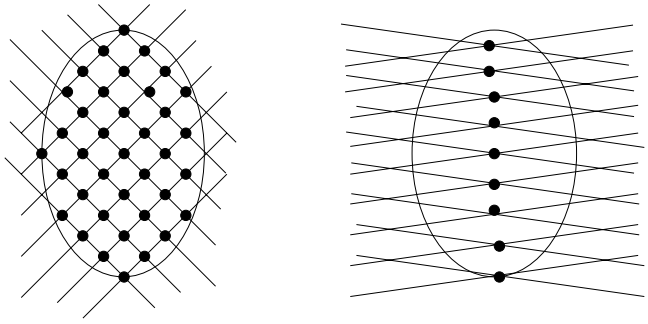

Figure 5.3: *Influence of the geometry of the primary satellites on the number of solutions in the inital search set.*

with the objective to minimize the PDOP, we are left with a very large number of candidates, and the computational burden is highly increased. However, there is a limit in selecting the primary satellites with a high PDOP, as the integrity will decrease. This compromise is also reported in [ABI91].

For example, the primary satellites can be chosen among the satellites of elevation greater than 7.5^o as the satellites yielding the closest PDOP to the arbitrary but reasonable value of 7.5.

Once the primary satellites are identified, the model (5.3) can be split into 2 systems of equations:

$$\Phi_P(k) = -C_P(k)\delta X(k) - N_P + B_P(k) \tag{5.4}$$

$$\Phi_S(k) = -C_S(k)\delta X(k) - N_S + B_S(k) \tag{5.5}$$

where the first system 5.4 is the system of the primary satellites, and the system 5.5 is the system of the non primary satellites, called the *secondary satellites*.

The initial search set, denoted N_0, can be built as the set of the three-integer combinations $N_{P_{abc}} = [a\,b\,c]^\top$ associated with a position contained within the search volume using (5.4) as:

$$\delta\hat{X}_{P_{abc}}(k) = -S_P(k)\Phi_P(k) - S_P(k)N_{P_{abc}}$$

where $S_P(k)$ is the pseudo-inverse of the primary system (5.4).

Thus, at each measurement epoch k, for each candidate $N_{P_{abc}} = [a\,b\,c]^\top$ in the set N_k at epoch k, the value of the associated secondary ambiguities $N_{S_{abc}}$ has to be determined.

This can be done using only the phase measurements at epoch k, although a more robust estimate can be elaborated using all of the previous measurements.

The first method is based on the assumption that, for the true solution $N_{P_{abc}} = N_P$, the vector

$$\tilde{N}_{S_{abc}}(k) = -\Phi_S(k) - C_S(k)\delta\hat{X}_{P_{abc}}(k) \tag{5.6}$$

should be very close to N_S under normal low noise conditions. Thus we can choose to set

$$\hat{N}_{S_{abc}}(k) = Round\left[\tilde{N}_{S_{abc}}(k)\right]$$

But if the data is affected by multipath, $\hat{N}_{S_{abc}}(k)$ may be different from N_S.

A more robust estimate can be obtained if all the $\hat{N}_{S_{abc}}(k)$ are averaged over time. We will then have, for each secondary satellite i:

$$\hat{N}_{S_{abc_i}}(k) = Round\left[\frac{1}{k-k_i}\sum_{j=k_i}^{k-1}\tilde{N}_{S_{abc_i}}(j)\right] \tag{5.7}$$

where k_i is the first epoch of lock on the signal transmitted by satellite i.

5.2.2 LSAST specific steps

The estimate $\hat{N}_{S_{abc}}(k)$ is used by the LSAST to determine the phase measurements predictions for all the visible satellites, while the MAPAS method uses them to compute the phase measurements for the secondary satellites only.

Using the candidate ambiguity and its associated secondary ambiguity prediction, the LSAST computes the corresponding phase prediction error z_{abc} and its associated squared norm, then checks its validity against χ^2 values.

The complete ambiguity candidate is

$$\hat{N}_{abc}(k) = \begin{bmatrix} N_{P_{abc}} \\ \hat{N}_{S_{abc}}(k) \end{bmatrix}$$

This candidate is inserted in the complete model (5.3) to determine a prediction of the complete double differenced observations. We have

$$\hat{\Phi}_{abc}(k) = -C(k)\delta\hat{X}_{abc}(k) - \hat{N}_{abc}(k)$$

with $\delta\hat{X}_{abc}(k) = -S(k)\Phi(k) - S(k)\hat{N}_{abc}(k)$, where $S(k)$ is the pseudo-inverse of the complete model.

Therefore, the prediction error z_{abc} is:

$$z_{abc} = \delta\hat{X}_{abc}(k) - \delta X_{abc}(k) \tag{5.8}$$

As presented in [LEI95] for example, if $N_{P_{abc}} = N_P$, then

$$R_{L_{abc}}(k) = z_{abc}^{\top}(k)\Sigma_c^{-1}(k)z_{abc}(k) \sim \chi^2_{n_k-4}$$

where $\Sigma_c(k)$ is the covariance matrix of the complete vector of observations $\Phi(k)$.

Therefore $R_{L_{abc}}(k)$ can be checked against a likelihood threshold $\chi_{1-\alpha_L,(n_k-4)}$. But this test, called the *local test*, uses only the current prediction errors and may not be very reliable.

This problem can be overcome if we note that

$$R_{G_{abc}}(k) = \sum_{j=1}^{k} R_{L_{abc}}(j) \sim \chi^2_{N_T(k)}$$

where $N_T(k) = \sum_{j=1}^{k}(n_j - 4)$. Thus we can build a more reliable test, based on all the previous residuals. This test is called the *global test*.

Improper solutions are progressively rejected from the search set, and the best solution is rapidly identified as the candidate associated with the lowest global residual. Confidence in the fact that this candidate is the correct one can be gained by performing the following approximate verification, as presented in [FRE91]:

$$\frac{R_G^*(k)}{R_{G_{abc}}(k)} \sim F_{\alpha_F, N_T(k), N_T(k)} \tag{5.9}$$

where $R_G^*(k)$ is the second lowest global residual at epoch k.

5.2.3 MAPAS specific steps

The MAPAS method uses the predicted value of the secondary ambiguities to compute the associated secondary phase observations

$$\hat{\Phi}_{S_{abc}}(k) = -C_S(k)\delta\hat{X}_{P_{abc}}(k) - \hat{N}_{S_{abc}}(k)$$

and the corresponding phase prediction errors $z_{S_{abc}}(k)$:

$$z_{S_{abc}}(k) = \hat{\Phi}_{S_{abc}}(k) - \Phi_{S_{abc}}(k) \tag{5.10}$$

Then, the value of the a *priori probability density function* is computed as

$$f\left(z_{S_{abc}}(k) \mid N_{P_{abc}} = N_P\right) = \frac{1}{2\pi^{\frac{n_k-4}{2}}\sqrt{det\left(\Sigma(k)\right)}} \times exp\left(-\frac{1}{2} z_{S_{abc}}^{\top}(k)\Sigma^{-1} z_{S_{abc}}(k)\right) \tag{5.11}$$

where

$$\begin{aligned}\Sigma(k) = {} & C_S(k)S_P(k)\Sigma_{PP}(k)S_P(k)^{\top}C_S(k)^{\top} \\ & +\Sigma_{SS}(k) - C_S(k)S_P(k)\Sigma_{PS}(k) \\ & -\Sigma_{PS}(k)^{\top}S_P(k)^{\top}C_S(k)^{\top}\end{aligned}$$

$\Sigma_{PP}(k)$ and $\Sigma_{SS}(k)$ are the covariance matrices of the primary and the secondary observations.

The a posteriori probability is computed using Bayes' rule:

$$P\left[N_{P_{abc}} = N_P \mid (z_{S_{abc}}(k)\right] = \frac{f\left(z_{S_{abc}}(k) \mid N_{P_{abc}} = N_P\right)}{\sum\limits_{abc \in N_k} f\left(z_{S_{abc}}(k) \mid N_{P_{abc}} = N_P\right)} \tag{5.12}$$

Thus, if the *a posteriori probability* of a candidate is lower than a *predefined threshold* denoted P_{min}, then it is rejected from the set and will not be tested for at the next epoch. If this probability is larger than a preset decision threshold denoted P_0, then this candidate is elected as the correct solution.

Figures 5.4(a) and 5.4(b) illustrate the behavior of the algorithm.

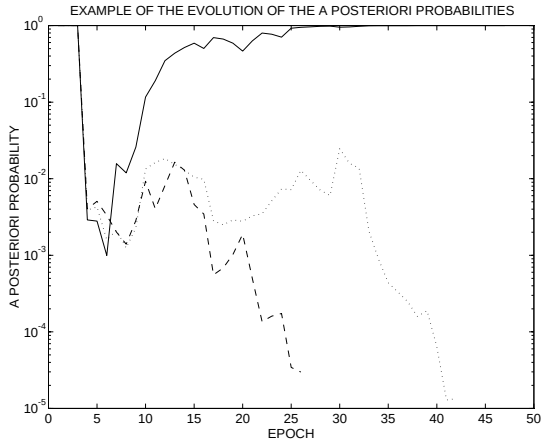

(a) *Example of the evolution of the a posteriori probabilities over time. The solid line corresponds to the correct combination. The dashed and the dotted lines correspond to two wrong solutions that are rejected sooner or later.*

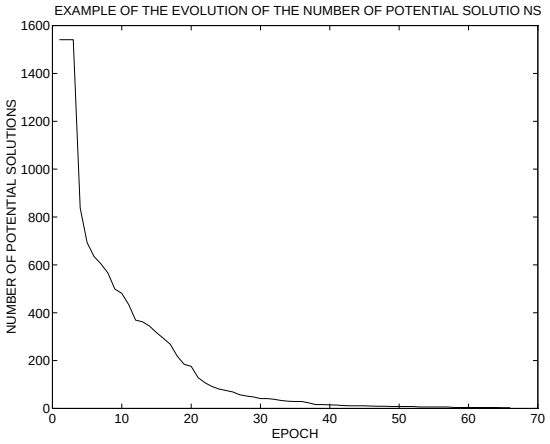

(b) *Example of the evolution of the number of potential solutions in the set. The set contains 1541 initial potential solutions. The program waits for 3 epochs before beginning the rejection of the low probability candidates.*

Figure 5.4: *Evolution of internal parameters of MAPAS.*

A subtile tradeoff must be achieved when specifying the rejection threshold P_{min} and the decision threshold P_0. Both of them must be adjusted so that false solutions are quickly rejected from the set, while the correct combination is kept. Assigning a high value to P_{min} will make the algorithm reject quickly the false solutions. However, it will increase the chances for the true combination to be accidentally eliminated as well, and the error probability will be larger. If that value is set too low, then the time of convergence, also called the time to first fix the ambiguities, will be slightly higher, and a prohibitive number of operations will have to be performed by the processor. Similarly, setting P_0 with too low a value may enable a false solution to be elected, and the error probability will increase. On the other hand, setting it with a high value will increase the time of convergence.

It appears that for reasonable values of P_0 and P_{min}, P_0 has a strong influence on the time to first fix the ambiguities while P_{min} directly affects the error probability.

As the abnormal transient values of posterior probability are mostly observed during the first ten epochs, when all the candidates share the unit probability, it happens very often that the a posteriori probability of the true solution reaches a low value. But it is very rare to see a false solution pass the upper acceptance threshold P_0 when the true solution is still in the set.

Thus, if a low error probability is to be reached, it is important that the rejection threshold P_{min} be set to a very low value. However, as the quantity of operations depends strongly on the number of candidates handled by the procedure, specifying too low a value for P_{min} may prevent the use of the algorithm for real time applications. Indeed, if P_{min} is set to a very low value, then a high number of candidates will be kept in the search set for a long time because low probability candidates will not be rejected. Therefore, if P_{min} is decreased, the computational burden is increased, and it may exist a point at which the computation time is larger than the time of convergence.

5.2.4 Implementation of LSAST and MAPAS

The algorithms of LSAST and MAPAS only differ by the steps dedicated to the evaluation of the criterion. These algorithms are presented in figures 5.5 and 5.6.

```
selection of primary satellites
read data
construction of 𝒩
while best P(k) < P_0
    read data
    compute Σ(k)
    for each N_P = [a b c] ∈ 𝒩(k)
        if f(k−1) is available then
            compute P(k−1)
            reject N_P if P(k−1) < P_min
        end if
        if N_P ∈ 𝒩(k) then
            update best P(k−1)
            compute N̂(k)
            compute z_abc(k)
            compute f(k)
            update s(k) = Σf(k)
        end if
    end for
end while
```

Figure 5.5: *Main steps of the MAPAS algorithm.*

```
selection of primary satellites
read data
construction of 𝒩
while best R_G(k) / R*_G(k)<F
    read data
    compute Σ(k)
    for each N_P = [a b c] ∈ 𝒩(k)
        if R_L(k−1) is available then
            eliminate N_P if R_L(k−1) > χ²_L
                          or R_G(k−1) > χ²_G
        end if
        if N_P ∈ 𝒩(k) then
            update value of best R_G(k−1)
            compute N̂(k)
            compute z_abc(k)
            compute R_L(k)
            update R_G(k) = ΣR_L(k)
        end if
    end for
end while
```

Figure 5.6: *Main steps of the LSAST algorithm.*

The algorithms of LSAST and MAPAS can be adapted to improve the efficiency of their selection. The main improvement is obtained by setting a rejection threshold that is tolerant at the beginning, and becomes more and more selective as time goes. Such an adaptation is described here:

LSAST. The rejection of the candidates is made through the local and the global test. The threshold of the local test was set as a constant, in such a way that the error probability is satisfying. The threshold of the global test is lowered over time, so that the procedure is sped up. The evolution of this threshold is plotted in figure 5.7.

MAPAS. The rejection of the candidates is based on a test on the posterior probabilities of the combinations. The minimum probability used to obtain this rejection is increased over time, as indicated in figure 5.7.

5.3 DIAS and FASF: two integer estimation techniques

Considering that the ambiguity resolution presented in section 5.2 is a complex process, it may sound natural to simply try to estimate the ambiguities. A vector model of the carrier phase measurements is as recalled in 5.3:

$$\Phi(k) = -C(k)\delta X(k) - N + B(k) \tag{5.13}$$

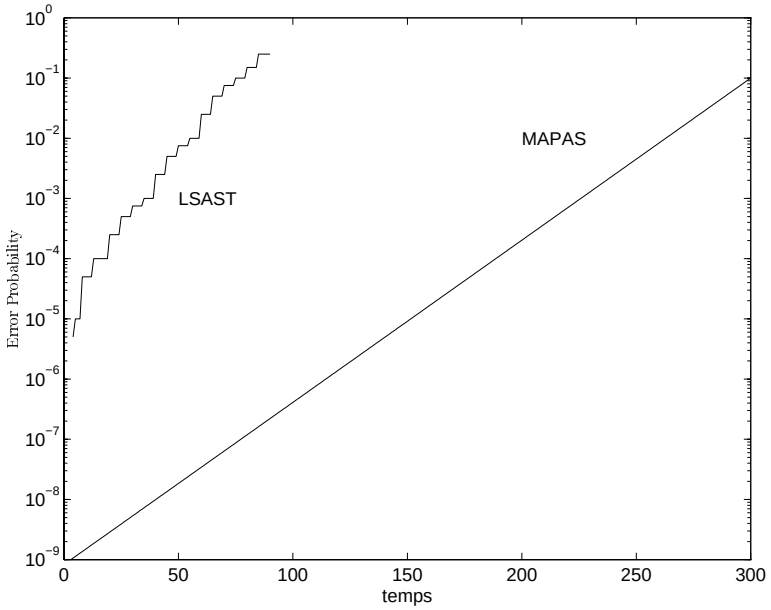

Figure 5.7: *Evolution of the rejection threshold of LSAST and MAPAS*

In this equation, we can think of $\delta X(k)$ and N as two components of a more global vector that would gather position and ambiguity unknowns. In this approach, we can use an identification procedure to estimate these two components. However, to date, there is no analytical solution to the identification of real and integer variables in an equation such as 5.13. Therefore, the most common strategy is to achieve this estimation in two stages. The mixed floating point and integer estimation problem represented in 5.13 is split in two successive identification problems: first, a classical analytical procedure is used to estimate the position and ambiguities as floating point quantities, then a specific algorithm is run to fix the ambiguities as integers. Several algorithms were developed to achieve this resolution, among which is the Lambda method, presented in [TEU94]. A comparison of specific algorithms can be found in [HW95a].

The Fast Ambiguity Search Filter (FASF) is a technique for resolution of GPS carrier phase ambiguities On-the-Fly that uses a *Kalman filter* combining position and ambiguities in its state vector to fix recursively the float ambiguities included in the *state vector* [CHE95].

The Direct Integer Ambiguity Search (DIAS) estimates in two stages the ambiguity vector. It uses a classical identification technique (Least Squares or Kalman) to estimate position and ambiguity values, then uses the integer constraint to solve the ambiguities with an integer least squares optimization procedure [WS95]. The ambiguity vector can only be released by the procedure after it was shown consistent with the measurements made on several epochs.

This section does not present the details of the principles of these techniques, as they can be found in the related publications [CHE95, CL94, WS95].

Both of these techniques comprise three main steps:

- a classical floating point estimation stage (Least Squares or Kalman)
- a specific integer selection stage
- a validation stage before releasing the value of the selected integer combination

These three steps are described in the following three sections.

5.3.1 Position and floating point ambiguity estimate

The first step of both procedures consists in processing the carrier phase measurements to determine at each epoch an estimate of the position and ambiguities as floating point quantities.

The estimation of $\delta X(k)$ and N can be made using any of the available identification techniques. The most common technique is the Kalman filter (see appendix L).

The identification procedure provides an optimal estimate $[\delta\hat{X}(k)^T\hat{N}^T]^T$ of the state of the system on the basis of the observation model recalled in 5.13. Some particular techniques, like Kalman filtering, require the additional assumption of an observation model. The procedure also provides the covariance matrix of the state estimate:

$$\Sigma_k = \begin{bmatrix} \Sigma_{\delta\hat{X}_k} & \Sigma_{\delta\hat{X}_k,\hat{N}_k} \\ \Sigma_{\hat{N}_k,\delta\hat{X}_k} & \Sigma_{\hat{N}_k} \end{bmatrix} \tag{5.14}$$

where

- $\Sigma_{\delta\hat{X}_k}$ is the covariance matrix of the position estimate.
- $\Sigma_{\hat{N}_k}$ is the covariance matrix of the ambiguity estimate.
- $\Sigma_{\delta\hat{X}_k,\hat{N}_k}$ and $\Sigma_{\hat{N}_k,\delta\hat{X}_k}$ are the cross-covariance matrices of the position and ambiguity estimates.

This covariance matrix is used in conjunction with $\hat{N}$ in the next step.

5.3.2 Integer fixing

The second step of the resolution consists in fixing the floating point ambiguities as integer numbers at each measurement epoch.

FASF specific steps

The principle of the FASF algorithm is to fix recursively several components of the ambiguity vector and to determine the confidence interval of the remaining ambiguity components. This process is called the Recursive Computation of the Search Range (RCSR) for the ambiguities. The RCSR is comprised of the following recursive steps at each epoch.

Step 1 of the algorithm consists in determining the integer search range of the first component of the ambiguity vector. This is done by choosing a set of integer values centered on the floating point integer, with an amplitude proportional to the standard deviation of this estimate, as provided by $\Sigma_{\hat{N}_k}$. Then the first integer in the set is selected, and is assigned to the first ambiguity component. At this point, this first ambiguity is considered as known, and removed from the unknowns. The state of the system now comprises the position and the $n_k - 2$ ambiguities. The Kalman filter is re-run, and a new covariance matrix is provided for this reduced state vector. Therefore, the same process can be applied on the first component of the new ambiguity vector, and will be applied recursively on each first component. The exploration stops at a particular vector component when the confidence interval of the estimate does not contain any integer, or if all the possible integers of the interval have been searched. In this case, the algorithm backs up one node and tries the next integer of the confidence interval of the upper level component.

After the recursion is complete, all the possible ambiguity vectors are formed by collecting the combinations that successfully reached the last exploration level. If this number is zero, or if it is larger than a preset threshold (four, ten, ...), unability to fix the ambiguities is declared, because two many candidates are still competing. If this number is one, the obtained combination is elected as the true combination. In the other case, a validation procedure is carried out, as explained in section 5.3.3.

DIAS specific steps

DIAS uses a numerical least squares optimization procedure to find the integer vector $\hat{\hat{N}}$ such that

$$\left(\hat{\hat{N}} - \hat{N}\right) \Sigma_{\delta \hat{N}_k} \left(\hat{\hat{N}} - \hat{N}\right) \text{ is minimum} \tag{5.15}$$

A large number of procedures are available to accomplish this task. The most popular procedures are based on the branch and bound algorithm.

When this resolution is achieved, a candidate ambiguity vector is fed to the validation stage. Note that this vector may not be the same at each epoch.

5.3.3 Validation stage

The final step of the ambiguity estimation procedures is a validation stage that uses statistical properties to sort all the candidates delivered by the previous stage.

In the case of FASF, when several candidates are available at the end of the RCSR, the ambiguity solutions that emerged correspond to all the combinations that could be formed after the tree exploration. The technique used to sort between all of them is to compute the ratio of the second minimum weighted squared sum of the prediction residuals over the minimum weighted squared sum of the prediction residuals. This ratio is compared with a preset confidence threshold, as in expression 5.9 for example. The combination elected is the one with the minimum weighted squared sum, that passes the test.

In the case of DIAS, the ambiguity candidates to be validated are the different vectors that came out of the integer optimization procedures at different epochs. The election of a combination is declared when it successfully came out of a 3 step validation process. First, the solution must be detected. This detection period ends when the optimal solution coming out of the integer estimaiton procedure is the same for several epochs, and when the ratio test described in the previous paragraph is passed. Then, this solution is confirmed: the candidate must pass the ratio test for a period lasting 30 s to 60 s. After this, the candidate is elected as the true solution.

We can see that the validation procedure is based on hypothesis testing, that requires knowledge of the statistical distributions of the observations. As these distributions cannot be identified with a good confidence level because of the complexity of the porcesses driving the evolution of the noises affecting the double differenced observations, the validation procedures are usually based on wrong assumptions. Therefore, as the ambiguity candidates are validated using unrealistic assumptions, the problem of the validation stage still remains unsolved [HW95b, TEU94].

Chapter 6

REQUIREMENTS OF AROF PROCEDURES

The adequacy of the AROF procedures for the precision approaches must be assessed by comparing their performance with the required performance presented in table 2.1. To perform this comparison, it is necessary to establish a link between the characteristics of the AROF procedures and the operational parameters that are used to express the requirements.

In the first part of this chapter, the characteristics of the AROF procedures are identified and gathered into four main groups of parameters. Then, in the second part, the requirements presented in table 2.1 are used to determine constraints on the identified characteristics.

6.1 Characteristics of AROF procedures

This section presents an identification of the characteristics of the AROF procedures. The aim of this identification is to evaluate their suitability for a particular application and to compare them. Four groups of parameters are identified.

An AROF procedure is mainly characterized by its *performance* and *working assumptions*. Performance parameters are the *accuracy*, *time of convergence* and *error probability*. Working assumptions are the *nature* and the *mathematical model* of the measurements used. However, as the determination of the performance parameters is usually very difficult, it is important to have knowledge of the *internal characteristics* of the procedure in order to predict its potentials or limitations. Thus, the *processing method*, which induces the *nature* and the *quantity* of information extracted from the observations, as well as the *computational burden*, is an important feature of the procedure. Finally, as presented in [HE94], it is desirable that the procedure provides a *means of control* of the solution proposed under the form of a relationship between the decision thresholds of the algorithm and the obtained performance, and of a quantified criterion. Thus, the performance, working assumptions, processing method and means of control constitute four sets of parameters that we can use to characterize each AROF procedure and evaluate its adequacy to the desired application.

6.1.1 Performance

Ambiguity resolution procedures use the precise carrier phase measurements to improve the position accuracy. The position accuracy is evaluated as the deviation between the true position and the position computed using the information delivered by the AROF procedure. Both decision and integer estimation techniques presented in section 5.1 provide the same accuracy, as their final output is the

selected integer ambiguity vector. For float ambiguity resolution procedures, the accuracy is not of the same level, as the ambiguities are estimated as floating point quantities, not exploiting the integer nature of the ambiguities. In the first case, the accurate position can only be computed after the ambiguities are raised, while in the second case, the position accuracy is continuously improved.

As we know, the position accuracy obtained using any of the integer AROF procedures is of the order of a few centimeters at the most when the correct ambiguities are raised. However, if the procedures raise wrong ambiguities, the impact of this error on the resulting position is different depending on the structure of the procedures. Some of the procedures are always wrong by a lot of ambiguities on several tracking channels, while others can be wrong only on one tracking channel. Thus the obtained accuracy is an important parameter for selection of integer resolution procedures.

According to the analysis performed in section 5.1, the integer AROF procedures appear as *multiple hypotheses tests*. The final ambiguity selection is made at the epoch n after processing the phase measurements $\Phi_1^n = [\Phi(0) \dots \Phi(n)]$ when a preset decision condition is satisfied. Thus the size of the sample Φ_1^n is not known before the test is performed, and a compromise must be made between the delay in making the decision and the accuracy of that decision by specifying the *decision condition*. This kind of test is called a *sequential test*. This section identifies the parameters useful to characterize the performance of such tests.

The set of the potential integer vectors constitutes the set of the unknown parameters of the probability density function of the observations. Let us call this set $\mathcal{N}$. Thus, the procedure is built to decide between the hypotheses :

$$H_{a^1 \dots a^{n_k}} = \{[a^1 \dots a^{n_k}] : \left[N^1 \dots N^{n_k}\right] = [a^1 \dots a^{n_k}]\} \tag{6.1}$$

for each integer vector $[a^1 \dots a_{n^k}] \in \mathcal{N}$.

The decision is taken using the raw data

$$\Phi_1^n = [\Phi(1) \dots \Phi(n)] \tag{6.2}$$

The test is a *mapping* g that associates to the observation data Φ_1^n a particular hypothesis H_N :

$$g\left(\Phi_1^n\right) = H_{a^1 \dots a^{n_k}} \tag{6.3}$$

The important sets of parameters used to assess the quality of a sequential test are the set of the *error probabilities*, that characterize the reliability of the test, and the set of the *Average Sample Numbers (ASNs)*, that characterize its rapidity.

The set of the error probabilities is the set of the conditional probabilities:

$$\alpha_{a^1 \dots a^{n_k}} = P\left[g\left(\Phi_0^n\right) \neq H_{a^1 \dots a^{n_k}} \mid H_{a^1 \dots a^{n_k}} \ \ true\right] \tag{6.4}$$

We can build the weighted error probability as

$$\alpha(g) = \sum_{a^1 \dots a^{n_k} \in \mathcal{N}} P\left[H_{a^1 \dots a^{n_k}} \ \ true\right] \alpha_{a^1 \dots a^{n_k}} \tag{6.5}$$

The set of the ASNs is the set of the conditional expectations :

$$ASN_{a^1 \dots a^{n_k}} = E\left[n \mid H_{a^1 \dots a^{n_k}} \ \ true\right] \tag{6.6}$$

where E is the expectation operator.

A sequential test is usually built by specifying values for the error probabilities. These values are inserted into the theoretical expressions of the decision thresholds to design the test. The ASNs are also determined using their own theoretical expressions.

In the case of the ambiguity searching algorithms, like in the case of most multiple hypotheses sequential tests, these theoretical expressions are hard to derive, and the design is made with empirical threshold values. These values are set so that the measured error probabilities and ASNs are as low as required. The error probabilities and the ASNs thus become estimated criteria used to assess the performance of the test.

6.1.2 Working assumptions

The working assumptions of the AROF procedure are the nature and the mathematical models of the observations used by the algorithm.

The signals used by the procedure can be the L1 only signal or the L1 and L2 signals or maybe even an additional signal from a pseudolite or two. The measurements made on these signals can be phase only observations or code and phase observations.

The mathematical model can include a discrete white gaussian noise model for the observation noise, or maybe a more complex noise model adapted to the unavoidable time correlation of noise terms.

Usually, the noise is modeled as a discrete white gaussian noise. In this case, an important parameter is the a priori variance of the noise affecting the carrier phase measurements.

6.1.3 Processing method

The processing method is described by its mathematical principles. It is characterized by the nature and the quantity of information extracted from the observations, and the computational burden generated by the algorithm. In the case where the procedure relies on the knowledge of a position estimate fed to the procedure, another important parameter is the mathematical relationship between the uncertainty of the estimate and the size of the search volume.

6.1.4 Means of control

The means of control of the procedure are two-fold.

The first category of means of control contains the features of the procedure that provide a way to drive the final performance of the procedure. The most important parameter in this category is the theoretical link between the performance of the procedure and the internal decision thresholds of the algorithm. Note that this theoretical relationship may not be known.

The second set of means of control contains all the output parameters that enable the user to monitor the performance of the procedure. This set comprises the parameters that enable to quantify the confidence that can be placed in the solution provided, and to identify the cause for failure if this happens.

6.1.5 Summary

A summary of the characteristics of AROF procedures is presented in table 6.1.

Characteristics of AROF procedures	Description
Performance parameter	Accuracy, Time of convergence, Error Probability
Working assumptions	Nature and model of processed measurements
Processing method	Functional principle, nature and quantity of information extracted from observations, computational burden size of search volume
Means of control	Relationship between performance and decision thresholds, Quantification of error, Error indicators

Table 6.1: *Summary of identified characteristics of AROF procedures.*

6.2 Constraints on characteristics

The aim of the study reported here is to contribute to the evaluation of the potentials of AROF procedures for application to aircraft precision landing. Therefore, it is important to understand what are the implications of the operational requirements presented in chapter 2 on the characteristics of AROF procedures presented in chapter 6. The requirements are expressed using four parameters: accuracy, integrity, continuity of service and availability. In this chapter, each of these parameters is analysed, and constraints are derived from the requirements expressed on these parameters. It must be noted that the distinction between the availability and the continuity of service of such techniques has not yet been fully agreed upon.

The analysis performed in this chapter consists in the application of the requirements presented in chapter 2 on the AROF procedures. These requirements are expressed for the *whole landing system*. The complete system is composed of the *space* and *control* segment of the GPS satellites, of the *ground equipment*, of the *data-link*, and of the *airborne landing equipment*. As the AROF procedure is one component of the airborne landing equipment, only part of the requirements presented in table 2.1 should apply to the procedure itself.

6.2.1 Accuracy

The position *accuracy* obtained after correct resolution of the carrier phase ambiguities by an integer AROF procedure is of the order of a few centimeters, which is highly satisfactory for CAT II/III landings. Nevertheless, the resolution of the ambiguities down to a few L1 integer cycles might also be acceptable, if we consider the accuracy requirement stated in table 2.1. We will see in this section that the consideration of all the requirements stated in table 2.1 implies that ambiguities have to be solved down to the last L1 cycle.

The required accuracy of the ambiguity solution proposed is dependent upon the influence of an error in the ouput ambiguity on the accuracy of the position computed using this ambiguity. This influence depends on the processing method of the procedure. For example, for procedures like LSAST or MAPAS, that search the ambiguities of a set of four satellites called the primary satellites, the impact of a one cycle error on the primary ambiguities is large on the output secondary ambiguities. Thus, a one cycle error on the primary ambiguities induces a large positioning error. In chapter 8, we show that the vertical position error induced by a minimal ambiguity error ambiguity on the primary satellites is of the order of one meter. Therefore, it is desirable that such procedures solve the ambiguities down to the last cycle to fulfill the CAT II and CAT III vertical accuracy requirements. However, this is not true for procedures like DIAS and FASF that directly solve the ambiguities of

all the satellites as a whole, and the position error induced by a one cycle error on one or several satellites is most of the time less than 30 cm (see chapter 8). In this case, CAT II vertical requirements can be fulfilled if the ambiguities are solved down to $\pm$ 5 L1 cycles 95 % of the time, and CAT III vertical requirements can be fulfilled if ambiguities are solved down to $\pm$ 2 L1 cycles 95 % of the time.

However, in order to fulfill the safety and reliability requirements, it is mandatory to reduce the maximum tolerable ambiguity error. A complete analysis of the connection between the integrity and the continuity risks, presented in table 2.1, and the accuracy requirement is still to be carried out. But it is foreseen that all these two requirements force the landing system to have at least a decimeter accuracy, as shown in [HE95]. Therefore, in this study, the ambiguities are required be solved down to the last L1 cycle.

6.2.2 Integrity

The *integrity risk* of the procedure is directly related to its error probability, which is the probability that the procedure raises out of bounds ambiguities. Thus, the error probability of the AROF procedure has to be at least lower than the integrity specified for the CAT II/III landing system as whole.

The *time-to-alarm* constraint applies on the precise positioning module once the ambiguities have been delivered by the procedure. It requires the implementation of a quality control procedure that checks continuously the consistency of the ambiguity solved, and monitors the measurements for detection of cycle slips and abnormal observations as presented for example in [LL92]. This module has to be extremely efficient, and provide alarms in less than 1 second after occurence of a dangerous event.

As the time of convergence of the AROF procedure is usually of several tens of seconds, the verification of the ambiguity delivered cannot be made only by a second AROF procedure that would be launched after the convergence of the first one. Instead, the quality control module should use all of the output means of control of the procedure to check the consistency of the solution.

6.2.3 Continuity of service

The precise positioning service can only be provided once the ambiguities have been raised by the AROF procedure. As there is no means to check the capacity of the AROF procedure to raise the ambiguities in due time, the aircraft starts the precision approach if all the other necessary means are declared as available. However, at one point on the approach path, the aircaft will need a precise position information to proceed safely to the runway as specified by the operational constraints. This point, which we call the *High Accuracy Decision Threshold (HADT)*, is the lowest point on the approach path at which the ambiguities have to be declared as raised by the AROF procedure. It must be located before the decision threshold of the approach phase, in order to ensure proper stabilization of the aircraft when crossing the CAT II or CAT III decision threshold. In the evaluations performed during this study, this point has been taken as the CAT I decision threshold, although it is probable that this point would have to be moved further away from the runway threshold to ensure safe stabilization of the aircraft when switching from the code DGPS to the phase DGPS.

While descending towards the runway, a failure of the AROF procedure to raise the ambiguities before the High Accuracy Decision Threshold (HADT), or an incapacity to correct a detected cycle slip is considered as a *discontinuity of the service*.

Thus the AROF procedure must deliver its ambiguities in the time interval defined as the period starting with the entrance of the aircraft within the coverage area of the phase DGPS and ending with the time of crossing of the HADT. Here, the coverage area is not defined by the quality of RF transmission of the data, but by the validity of application of the carrier phase corrections or measurements, driven by the spatial decorrelation of errors. Thus the continuity of service requirement can be translated as a bound on the time of convergence of the procedure, based on the size of the coverage area, as presented in figure 6.1.

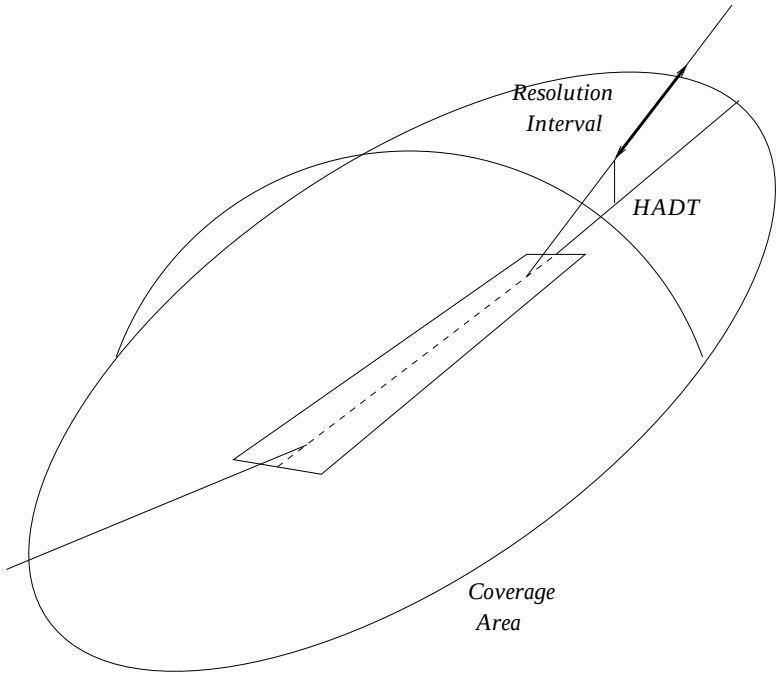

Figure 6.1: *Illustration of the resolution interval allowed to the procedure: the resolution starts at the entrance in the coverage area and must be achieved before the planes reaches the High Accuracy Decision Threshold (HADT).*

6.2.4 Availability

The *availability* requirement presented in table 2.1 concerns the availability of the signal in space used for the intended landing category at the initiation of the approach. As the accuracy requirements at the beginning of the approach are much looser than the final ones, the accurate ambiguity solution does not have to be available from the very first beginning of the approach. Nevertheless, the user has to make sure that the procedure would be able to perform the ambiguity resolution for the whole duration of the operation. This means that any predicted outage will be interpreted as a lack of availability. Thus, for example, a predicted degradation of geometry, or a scheduled maintenance of the ground or space segment has to be accounted for in the availability computation.

It must be emphasized that the availability expressed here is the availability of the signal in space used by the *landing system as a whole*, which differs from the *availability of the precise position* conditioned by the availability of the ambiguities.

6.2.5 Summary

A summary of the constraints imposed on the characteristics of the AROF procedures is presented in table 6.2.

Characteristic	Constraint
Accuracy	Resolution down to last L1 cycle
Time of convergence (Time To First Fix the ambiguities)	Lower than interval defined by coverage area and HADT
Error Probability	Lower than integrity risk
Nature and model of processed measurements	As many measurements as possible
Functional principle	Robust and Optimal
Nature and quantity of information extracted from observations	Use all information collected from initialization
Computational burden	Computation time lower than Time of convergence
Relationship between performance and decision thresholds	Theoretical link recommended
Quantification of error	Required
Error indicators	Required

Table 6.2: *Summary of constraints on characteristics of AROF procedures derived from operational requirements.*

Chapter 7

THEORETICAL PERFORMANCE

All of the AROF procedures can solve ambiguities in seconds in optimum operating conditions. However, these procedures are likely to fail raising the ambiguities in due time, or may even provide the user with incorrect ambiguities. Thus, in order to determine the suitability of a particular procedure for a specific application, it is desirable to know its *time of convergence* and *failure rate*, which are directly related to the required *availability* and *integrity* of the solution. These performance parameters can be evaluated from theoretical considerations, or using simulated data, or from extensive experiments in the field. This chapter focuses on the evaluation of theoretical performance of AROF procedures. Because of the sequential structure of these procedures, it is very difficult to perform such an analysis on AROF procedures, and very little material has been published on this subject. To our knowledge, the only publications available on this topic were made by the LTST on the MAPAS procedure.

7.1 Determination of theoretical performance

As we saw in section 5.1, AROF procedures all behave like multiple hypotheses sequential tests. The ambiguities are delivered after a variable number of observations are processed, depending on the value of the *decision threshold* cast in the algorithm. The performance of these procedures is characterized by their error probability and time of convergence, also called time to first fix the ambiguities. Many factors influence the values of these parameters, such as the number of tracked satellites, the satellite constellation geometry and the adequacy of the noise model used by the procedure. Therefore, the theoretical evaluation of the impact of these factors on the performance of the procedure is very difficult and is hardly ever done. To our knowledge, the only publications available on this topic were made by the LTST on the MAPAS procedure in [MB96]. This evaluation is presented in the next section.

7.2 Analysis of theoretical performance of MAPAS

This section presents a theoretical analysis of the performance parameters of the Maximum A Posteriori Ambiguity Search (MAPAS) procedure using results derived for a multiple hypotheses sequential test called the *M-ary Sequential Probability Ratio Test (MSPRT)*. In particular, expressions of *bounds* and *asymptotic values* of the expected stopping time and error probability of MAPAS are determined as functions of the decision threshold, thus providing a means to control the performance. This study shows the influence of the number of satellites as well as the importance of the mode of selection of the primary satellites. The figures obtained are checked against observed values, showing the validity

of the determined bounds and the consistency of the asymptotic values, although they lack accuracy when the number of satellites is low.

7.2.1 The MAPAS method as an MSPRT

The MAPAS method is a multiple hypotheses test that sorts between thousands hypotheses represented by their associated three-integer vector:

$$H_{abc} = \{[a\ b\ c]^T : Np = [a\ b\ c]^T\} \tag{7.1}$$

The selection is done using the posterior probability of the secondary prediction errors, as presented in section 5.2.3.

The MSPRT (M-ary Sequential Probability Ratio Test) is a more general multiple hypotheses sequential test designed by Baum and Veeravalli [BV94] that they formulated in the following way.

Let $X_1, X_2, \ldots, X_n$ be an infinite sequence of random variables, independent and identically distributed (i.i.d.) with density f, and let H_j be the hypothesis that $f = f_j$ for $j = 0, 1, \ldots, M-1$. Assume that the prior probabilities of the hypotheses are known, and let π_j denote the prior probability of hypothesis H_j for each j.

The stopping time of the MSPRT is

$$Na = \text{ first } n \geq 1 \text{ such that } p_n^k > \frac{1}{1+A_k} \tag{7.2}$$

for at least one k, and the final decision is δ such that

$$\delta = H_m \text{ , where } m = arg\ \max_j\ p_{Na}^j$$

where

- $p_n^k = P[H = H_k \mid X_1, X_2, \ldots, X_n]$ is the posterior probability of H_k.
- $\frac{1}{1+A_k}$ is the decision threshold. A_k is a component of this threshold.

The MSPRT is a generalization of the *Sequential Probability Ratio Test (SPRT)*. Although the SPRT is *optimal* in the sense that it provides a *minimal stopping time for a given error probabilities set*, the MSPRT is an approximation of the *Bayesian optimal* solution. However, Baum and Veeravalli showed in [BV95] that the MSPRT is *asymptotically efficient* as, for a given error probabilities set, it becomes the *fastest decision making test* when the threshold components A_k decrease towards 0.

Several theoretical results concerning this test are presented by Baum and Veeravalli [BV94]. In particular, expressions are given for bounds and asymptotic values of the ASN and error probability.

The MAPAS method can be viewed as a particular application of the MSPRT to the observation sequence formed by the secondary phase prediction errors. However, comparing 5.12 with 7.2 shows that the observation sequences $z_{S_{abc}}(k)$ used by MAPAS depends on the tested hypothesis $[a\,b\,c]^T$, which is not true for the MSPRT. This problem can be solved by noting that the a posteriori probability of a candidate is independent of the three-integer vector used to compute the prediction error. To show this, we can write

$$z_{S_{abc}}(k) = -C_S(k)S_P(k)[N_{P_{abc}}(k) - N_P + B_P(k)] + N_S - \hat{N}_{S_{abc}}(k) - B_S(k) \tag{7.3}$$

thus

$$E\left[z_{S_{abc}}(k) \mid N_p = [\alpha\,\beta\,\gamma]^T\right] = -C_S(k)S_P(k)\left[N_{P_{abc}}(k) - N_{P_{\alpha\beta\gamma}}(k)\right] + N_{S_{\alpha\beta\gamma}}(k) - \hat{N}_{S_{abc}}(k) \quad (7.4)$$

and the argument of the exponential in the gaussian probability density function is

$$z_{S_{abc}}(k) - E\left[z_{S_{abc}}(k) \mid N_p = [\alpha\,\beta\,\gamma]^T\right] = -C_S(k)S_P(k)\left[N_{P_{\alpha\beta\gamma}}(k) - N_P\right] + N_S - N_{S_{\alpha\beta\gamma}}(k) \quad (7.5)$$

which is independent on $[a\,b\,c]^\top$. Thus, we can write

$$f\left(z_{S_{abc}}(k) \mid N_{P_{abc}}\right) = f\left(z_{S_{\alpha\beta\gamma}}(k) \mid N_{P_{abc}}\right)$$

allowing us to reformulate MAPAS using the decision criterion

$$P\left[N_P = N_{P_{abc}} \mid {z_{S_{\alpha\beta\gamma}}}_1^k\right] = \frac{f\left({z_{S_{\alpha\beta\gamma}}}_1^k \mid N_P = N_{P_{abc}}\right)}{\sum_{abc \in N_k} f\left({z_{S_{\alpha\beta\gamma}}}_1^k \mid N_P = N_{P_{abc}}\right)} \quad (7.6)$$

which is identical to the decision criterion (7.2) used by the MSPRT, considering that the prior probabilities of each hypothesis are equal. Here, $[\alpha\,\beta\,\gamma]^T$ can be any fixed three-integer vector.

Several hypotheses have to be made for the MAPAS method to be called an MSPRT:

1. We must assume that the *direction cosines* of the satellites from the moving receiver's point of view are *constant* during the whole resolution process. This is necessary if we want to consider that the residuals $z_{S_{\alpha\beta\gamma}}(k)$ are identically distributed over time. This hypothesis is a *pessimistic* assumption, as the evolution of the satellite geometry, although slow for vehicles of classical dynamics, enhances the selectivity of the procedure.

2. We must suppose that the phase measurement noise $B_i(k)$ is an *independent sequence* over time. This is a quite strong assumption, as usually the double differenced noise has slowly varying components which are mainly due to the carrier phase tracking error induced by multipath. This hypothesis *limits the range* of the theoretical developments presented in this work to the applications using measurements unaffected by low-frequency noise.

3. We need to consider that the *rejection process* of the MAPAS method, performed through the comparison of the posterior probabilities with the threshold P_{min}, has *no influence* on the structure of the test. That is, we must consider that the influence of the rejected combinations would have been negligible in the selection process if they had been kept in. Thus, we assume that all the M_0 hypotheses are considered at each measurement epoch. This hypothesis is *optimistic* for the *error probability* and *pessimistic* for the *expected stopping time*.

In the MAPAS case, all the A_k values are identical since all prior probabilities are assumed to be equal, as we assume that all the primary ambiguities in the search set have the chances to be the true ones. Therefore, there is no need to distinguish between them. Also, this threshold component will be simply denoted A. Furthermore, we can note that

$$P_0 = \frac{1}{1+A} \text{ and } A = \frac{1-P_0}{P_0}$$

which means that $P_0 \approx 1 - A$ when A is small.

7.2.2 Bounds on the stopping time and error probability

Baum and Veeravalli have determined bounds on the expected stopping time and error probability of the MSPRT. They can be applied to the MAPAS method as shown in this section.

Let N_a denote the stopping time, and δ the decision taken at time N_a. It can be proven that the ASN of the MAPAS method is finite by showing first that it is exponentially bounded, as the probability that t exceeds any N_a decreases exponentially with n. The demonstration, given for a general case in [BV94], results for the MAPAS method in

$$P\left[N_a > n \mid H_{abc} \text{ true}\right] \leq \frac{(M_0 - 1)^{\frac{3}{2}}}{\sqrt{A}} \max_{[ijk]\neq[abc]} (\rho_{ijk})^n$$

where

- $\rho_{ijk} = E_{f_{abc}}\left[\sqrt{\frac{f\left(z_{S_{\alpha\beta\gamma}}|N_P=N_{P_{ijk}}\right)}{f\left(z_{S_{\alpha\beta\gamma}}|N_P=N_{P_{abc}}\right)}}\right]$. E is the expectation operator.
- M_0 refers to the value M presented in equation 7.2: it is the number of hypotheses in the search set at epoch 0.

By the Cauchy-Schwartz inequality, it can be shown that

$$\rho_{ijk} < 1 \text{ for } [ijk] \neq [abc]$$

Consequently, for an assumed correct ambiguity value the corresponding stopping time is exponentially bounded. Then, N_a is necessarily finite.

Let $P\left[N_P = [a\,b\,c]^T \mid [i\,j\,k]^T\right]$ be the probability that the candidate $[a\,b\,c]^T$ is accepted assuming $[i\,j\,k]^T$ is the correct ambiguity. Then, $P\left[N_P = [a\,b\,c]^T \mid [a\,b\,c]^T\right]$ is the probability to retain the correct ambiguity. If α denotes the total error probability introduced in (6.5), then we have

$$\alpha = 1 - \sum_{[ijk]\in\mathcal{N}} P\left[N_P = [i\,j\,k]^T\right] P\left[N_P = [i\,j\,k]^T \mid [i\,j\;\;k]^T\right]$$

and

$$P\left[N_P = [a\,b\,c]^T \mid [a\,b\,c]^T\right] = \sum_{n=0}^{N_a} P\left[N_P = [a\,b\,c]^T \mid [a\,b\,c]^T, N_a = n\right] \tag{7.7}$$

Due to the MSPRT formulation, this probability is shown to be bounded in [BV94], as follows:

$$P\left[N_P = [a\,b\,c]^T \mid [a\,b\,c]^T\right] \geq \frac{1}{1+A} \sum_{[ijk]} P\left[N_P = [a\,b\,c]^T \mid [i\,j\,k]^T\right] \tag{7.8}$$

A summation over the vectors $[a, b, c]^T$ leads to

$$1 - \alpha \geq \frac{1}{1+A}$$

that is

$$\alpha \leq \frac{A}{1+A} \tag{7.9}$$

The deduced upper bound of α depends only on the decision parameter A. Furthermore, it can be shown that

$$\alpha \leq A \tag{7.10}$$

which is equivalent to (7.9) for small values of A.

Thus, it can already be determined that, if the desired error probability is approximately 10^{-10}, like for aircraft landing for example, then by setting $A = 10^{-10}$, which is $P_0 = 1 - 10^{-10}$, this objective can theoretically be fulfilled.

7.2.3 Expression of the asymptotic values of the expected stopping time and error probability

When the decision criterion P_0 is close to 1, that is when A is small, an expression of the value of the ASN and of the error probability is given in [BV94] using non linear renewal theory.

These asymptotic expressions all depend on the quality of the discrimination that can be made between the different hypotheses by observing the data. The level of separation is quantified by a parameter called the *Kullback-Leibler information* that represents the distance between two hypotheses among the erratic values of the random variable, characterized by its covariance matrix (see appendix J).

Denoting the Kullback-Leibler information between probability density functions f_{abc} and f_{ijk} as

$$D(f_{abc}, f_{ijk}) = E_{f_{abc}}\left[\ln \frac{f_{abc}(Z_{S_{\alpha\beta\gamma}})}{f_{ijk}(Z_{S_{\alpha\beta\gamma}})}\right] \tag{7.11}$$

it can be shown that

$$E_{f_{abc}}[Na] \to \frac{-\ln(A)}{\min\limits_{[ijk]\neq[abc]} D(f_{abc}, f_{ijk})} \text{ as } A \to 0 \tag{7.12}$$

Thus, as the separation between the hypotheses decreases, the number of measurements needed to identify clearly a combination increases. The vector $[i\,j\,k]^T$ minimizing $D(f_{abc}, f_{ijk})$ is the integer combination for which the secondary phase residuals are the most similar to those of the true hypothesis $[a\,b\,c]^T$.

This result can be applied to the MAPAS procedure by calculating $\min\limits_{[ijk]\neq[abc]} D(f_{abc}, f_{ijk})$.

The Kullback-Leibler information between the two multivariate normal distributions of the residuals $z_{S_{\alpha\beta\gamma}}$ representing hypotheses $[a\,b\,c]^T$ and $[i\,j\,k]^T$ is

$$D(f_{abc},f_{ijk}) = \frac{1}{2}\left(E_{f_{abc}}[z_{S_{\alpha\beta\gamma}}] - E_{f_{ijk}}[z_{S_{\alpha\beta\gamma}}]\right)^T \Sigma^{-1} \left(E_{f_{abc}}[z_{S_{\alpha\beta\gamma}}] - E_{f_{ijk}}[z_{S_{\alpha\beta\gamma}}]\right) \tag{7.13}$$

We can reformulate (7.3) using the following approximate expression of $\hat{N}_{S_{\alpha\beta\gamma}}(k)$ under low noise conditions:

$$\hat{N}_{S_{\alpha\beta\gamma}}(k) = Round\left[-\Phi_S(k) - C_S(k)\delta\hat{X}_{P_{\alpha\beta\gamma}}(k)\right] \tag{7.14}$$

Developing (5.6) using (7.3), (5.4) and (5.5) leads to

$$\hat{N}_{S_{\alpha\beta\gamma}}(k) = N_S + Round\left[-C_S S_P \left(N_{P_{\alpha\beta\gamma}} - N_P\right) - C_S S_P B_P - B_S\right] \tag{7.15}$$

Thus, (7.3) can be rewritten as follows

$$\begin{aligned} z_{S_{\alpha\beta\gamma}} &= -C_S S_P \left(N_{P_{\alpha\beta\gamma}} - N_P + B_P\right) - B_S \\ &\quad - Round\left[-C_S S_P \left(N_{P_{\alpha\beta\gamma}} - N_P + B_P\right) - B_S\right] \end{aligned} \tag{7.16}$$

and we have

$$E_{f_{abc}}\left[z_{S_{\alpha\beta\gamma}}\right] = -C_S S_P\left(N_{P_{\alpha\beta\gamma}} - N_P\right) - Round\left[-C_S S_P\left(N_{P_{\alpha\beta\gamma}} - N_P\right)\right] \tag{7.17}$$

under the same low noise assumptions as previously.

Developing (7.13) for the multivariate normal distribution of the residuals $z_{S_{\alpha\beta\gamma}}$ leads to

$$D(f_{abc}, f_{ijk}) = \frac{1}{2}\left(C_S S_P \delta N - Round\left[C_S S_P \delta N\right]\right)^T \Sigma^{-1}\left(C_S S_P \delta N - Round\left[C_S S_P \delta N\right]\right) \tag{7.18}$$

where $\delta N = [a\, b\, c]^T - [i\, j\, k]^T$.

The optimum δN value represents the ambiguity combination $[i\, j\, k]^T$ for which the lines of constant phase intersect the most similarly as in $[a\, b\, c]^T$, as explained in figure 5.2.

Simulations have been run to compute the minimum value of $D(f_{abc}, f_{ijk})$ for $\delta N \in \mathbb{Z}^3 / \{0\}$ such that $[i\, j\, k]^T \in \mathcal{N}$. It is useful to note that this minimum value is apparently independent of $[a\, b\, c]^T$, except for the fact that we must have $[i\, j\, k]^T \in \mathcal{N}$. Thus, a rigorous determination of this optimum value requires the search of the combination $[i\, j\, k]^T$ yielding the minimum value of (7.18) for each combination $[a\, b\, c]^T$. This is a very heavy calculation requiring a high computation power that we could not perform in all the cases. To simplify this problem, the optimization was done using an extensive search algorithm making no distinction between the different $[a\, b\, c]^T$ in the set, assuming that the resulting combination $[i\, j\, k]^T$ is in $\mathcal{N}$. This hypothesis has the tendancy to lower the minimum Kullback-Leibler distance, and represents a worst case assumption for the performance of the procedure.

Similarly, an expression of the asymptotic value of the error probability can be derived from [BV94], as they showed that

$$\alpha \to A\gamma \text{ when } A \to 0 \tag{7.19}$$

where γ is a coefficient such as $0 < \gamma < 1$ depending on the minimum Kullback-Leibler information computed previously. This result can be found in [BV94]. It is obtained through the application of nonlinear renewal theory. Practical techniques for computing γ can be found in [WOO82].

This asymptotic value provides a closer approximation to the error probability than equation (7.9).

7.2.4 Comparison between theoretical and observed values

The theoretical expressions (7.12) and (7.19) were used to compute the predicted values of the expected stopping time and error probability for a point located at the beginning of the landing path over Toulouse-Blagnac airport. The values were calculated each second over 24h, representing the predicted performance of the MAPAS procedure that would be initiated at the corresponding time. These values were computed with various configurations of the MAPAS procedure. Then, we compared these figures against the observed values obtained for simulations of the whole landing procedure at the same date and time. All the computations and simulations were performed assuming a phase measurement noise with standard deviation σ=0.05 cycle =1 cm. This value is quite high as compared to the phase measurement accuracy of 1mm, but it is selected 10 times larger to account for the other errors.

The calculation of the asymptotic values of the performance parameters of the MAPAS procedure is based on the determination of the minimum Kullback-Leibler distance between hypotheses, as well as on the computation of γ. This requires the selection of the primary satellites used by MAPAS. The

primary satellites are selected according to their elevation angle and PDOP factor. The values of the Kullback-Leibler distance and of γ were computed for primary satellites with a minimum elevation angle of 10^o and for a minimum ideal PDOP, as well as for an objective PDOP of 7.5, as explained in 5.2.

We first determined the value of this minimum Kullback-Leibler distance over 24 hours for a fixed point in the approach path over Toulouse-Blagnac airport. The calculation was done using the simplification described in the previous section. The evolution of this distance is shown in figure 7.1(a).

Similarly, the evolution of γ over 24h is plotted in figure 7.1(b).

The influence of the number of visible satellites is obvious from the comparison of figure 7.1(c) with figures 7.1(a) and 7.1(b). This comes from the fact that the separation between the hypotheses is easier when more observed data per epoch is used to check their consistency. Thus, the Kullback-Leibler distance increases with the number of satellites.

These computed values correspond to the expected stopping times plotted in figure 7.1(e), for $A = 10^{-10}$. The corresponding asymptotic value of the error probability is plotted in figure 7.1(f).

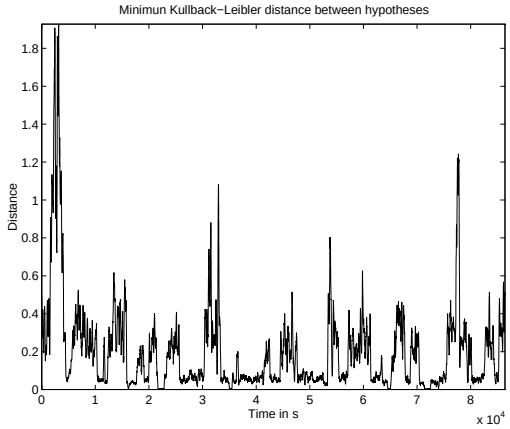

(a) *Average minimum Kullback-Leibler distance between hypotheses (primary satellites with minimum PDOP). Mean = 0.20, std = 0.24, min =* 1.4×10^{-3}*, max = 1.93.*

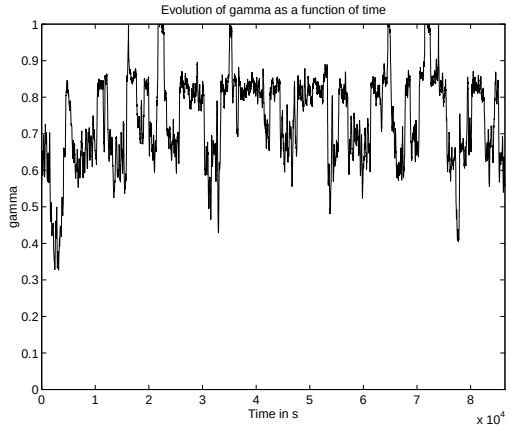

(b) *Evolution of* γ *over 24h (primary satellites with minimum PDOP). Mean = 0.7, std = 0.12, min = 0.33, max = 1.*

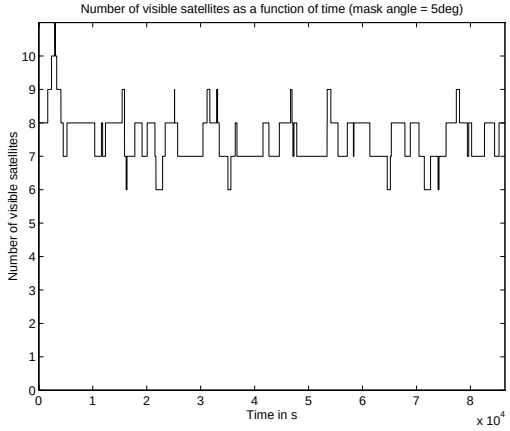

(c) *Total number of visible satellites during the 24h.*

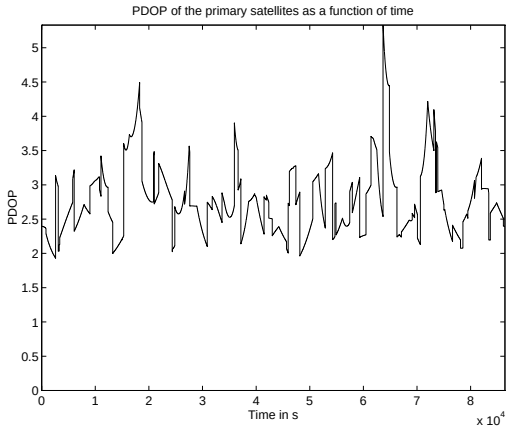

(d) *PDOP of the primary satellites (first case).*

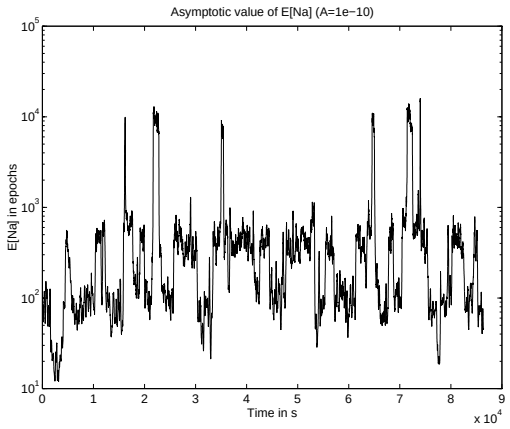

(e) *Asymptotic value of the expected stopping time for primary satellites with minimum PDOP. Mean = 594, std = 1687, min = 11.9, max =* 1.6×10^{4}*.*

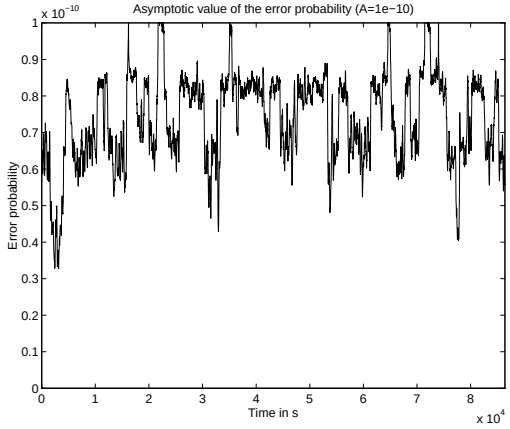

(f) *Asymptotic value of the error probability for primary satellites with minimal PDOP. Mean =* 7.4×10^{-11}*, std =* 1.2×10^{-11}*, min =* 3.3×10^{-11}*, max =* 1.0×10^{-10}*.*

Figure 7.1: *Theoretical performance for primary satellites with minimal PDOP.*

The influence of the PDOP of the primary satellites, plotted in figure 7.1(d) for this first case, can be emphasized by the comparison of the figures 7.1(a), 7.1(e) and 7.1(f) with figures 7.2(b), 7.2(c) and 7.2(d), when the PDOP is now as in figure 7.2(a).

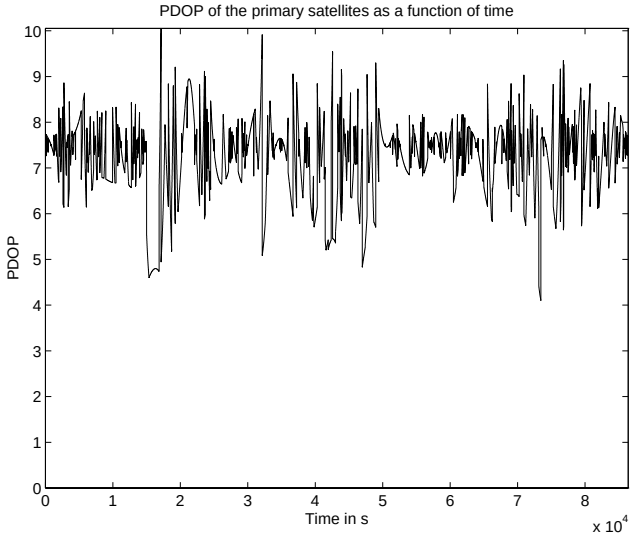

(a) *PDOP of the primary satellites (second case).*

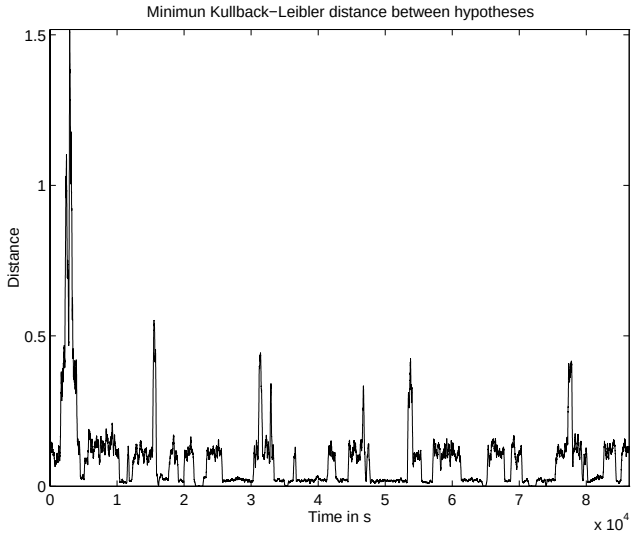

(b) *Average minimum distance between 2 hypotheses over 24h (primary satellites with PDOP close to 7.5). Mean = 0.09, std = 0.13, min =* 5.0×10^{-4}*, max = 1.52.*

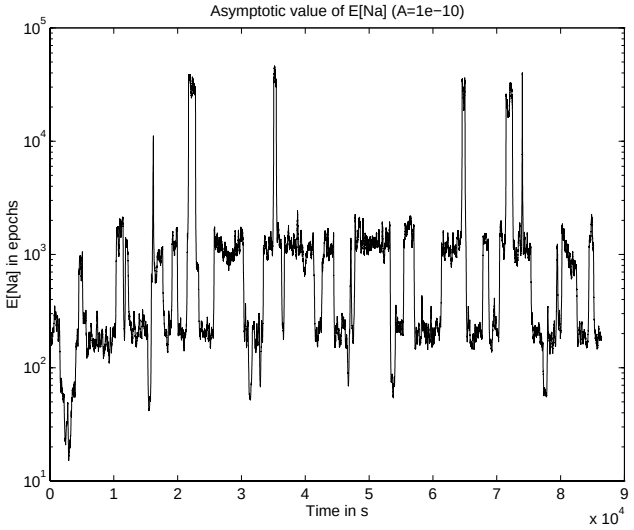

(c) *Asymptotic value of the expected stopping time over 24h (primary satellites with PDOP close to 7.5). Mean = 1674, std =* 5.3×10^{3}*, min = 15.2, max =* 4.6×10^{4}*.*

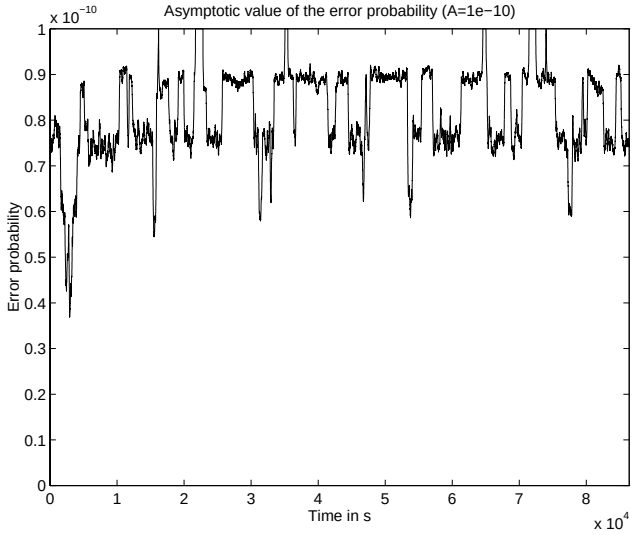

(d) *Asymptotic value of the error probability for* $A = 10^{-10}$ *(primary satellites with PDOP close to 7.5). Mean =* 8.2×10^{-11}*, std =* 9.6×10^{-12}*, min =* 3.7×10^{-11}*, max =* 1.0×10^{-10}*.*

Figure 7.2: *Theoretical performance for primary satellites with PDOP close to 7.5.*

To determine the accuracy of the asymptotic values, we ran the calculation of the minimum Kullback-Leibler distance at four distinct GPS times and compared the obtained results against observed ones. This was done for both primary satellites selection modes, as shown in tables 7.1 and 7.2. In order to obtain observable values of error probabilities, the threshold component A has been set to the relatively high value of 10^{-2}.

GPS time	194800	202800	172800	175750
PDOP of primaries	3.3	2.3	2.4	3.0
# sat.	6	7	8	11
Asymptotic $E[N_a]$	1690	74.4	9.3	2.5
Asymptotic α	9.6×10^{-3}	8.1×10^{-3}	5.6×10^{-3}	3.4×10^{-3}
Observed $E[N_a]$	172.4	104.2	51.9	11.1
Observed α	7.7×10^{-5}	1.2×10^{-4}	2.3×10^{-4}	2.1×10^{-4}
# trials	13000	13000	13000	13000

Table 7.1: *Comparison between computed asymptotic and observed values when the primary satellites are the ones with the lowest PDOP.*

GPS time	194800	202800	172800	175750
PDOP of primaries	8.1	7.5	7.6	7.5
# sat.	6	7	8	11
Asymptotic $E[N_a]$	6514	303	35.6	3.1
Asymptotic α	9.8×10^{-3}	9.0×10^{-3}	7.4×10^{-3}	3.7×10^{-3}
Observed $E[N_a]$	171.2	103.0	51.9	14.0
Observed α	5.5×10^{-4}	4.1×10^{-3}	6.2×10^{-4}	2.9×10^{-4}
# trials	23000	23000	23000	23000

Table 7.2: *Comparison between computed asymptotic and observed values when the primary satellites have the closest PDOP to 7.5.*

As we can see from tables 7.1 and 7.2, the observed error probability appears to be lower than the asymptotic one, and in every case the lower bound (7.9) is satisfied. This major result enables to determine the value of the design threshold P_0, using the desired error probability.

Furthermore, the accuracy of the computed asymptotic values is improved when the number of visible satellites increases, as the computed distance seems to be more stable.

7.2.5 Conclusion

The MAPAS procedure has been modeled as an M-ary Sequential Probability Ratio Test (MSPRT), so that general MSPRT results are applicable. Thus, the time of convergence of the MAPAS procedure, also called the time to first fix the ambiguities, has been shown to be finite, and an upper bound of the error probability has been given as a function of the decision threshold. Furthermore, asymptotic values of these two performance parameters have been given.

Comparison of the theoretical and observed values shows that the upper bound of the error probability seems to be satisfied in every case.

The relative evolution of the asymptotic values of the error probabilities and expected stopping time shows the influence of the number of visible satellites and of the PDOP of the primary satellites. Although these theoretical values are not very accurate when there are few visible satellites, a good prediction of the performance of the procedure can be obtained when the number of satellites is larger than 7.

Chapter 8

EVALUATION OF PERFORMANCE OF AROF PROCEDURES ON SIMULATED DATA

The performance of LSAST and MAPAS were estimated from the average performance observed during 12h to 24h, using simulated data in several configurations. The procedures are first run on data generated according to the assumed measurement model, with several noise levels. Then they are run on data augmented with one or two pseudolite signals. Finally they are run on data corrupted by multipath signals reflected off the Earth's surface.

As a courtesy of SEXTANT AVIONIQUE, the same evaluation for the DIAS and FASF procedures is presented at the end of this section.

The software used for LSAST, DIAS and FASF evaluation were implemented from theoretical principles found in published papers: [HAT91, LCL92], [WS95] and [CHE95, CL94]. Although the software used were not written by their original developers, the names of these methods have nevertheless been unchanged, even if only the theoretical principles have been conserved. Algorithms have been modified and adapted to CAT II/III applications and to simulations which were made.

8.1 Performance of LSAST and MAPAS on simulated data

8.1.1 Description of the simulations

The LSAST and MAPAS procedures were implemented in ADA and run on HP workstations and IBM PC compatible computers. The GPS phase observations are generated using the visible constellation from the receivers point of view. Thermal noise with preset standard deviation can be added to the measurements, as well as distortions induced by multipath generated from reflection off the Earth's surface. Moreover, observations from one or two pseudolites can be added to the measurement vector in order to assess potential benefits from their operation.

The measurements are computed at each epoch from the knowledge of the positions of the satellites and the simulated trajectory of the moving receiver, which corresponds to a certain scenario. In our case, the scenario is the landing phase of an aircraft at the Toulouse-Blagnac airport on a 3^o glideslope, beginning between 10 km and 20 km from the runway. The plane flies at a speed of 62 $m.s^{-1}$. The scenarios are run one after the other for 24h.

The performance parameters are expressed in terms of time of convergence, integrity and availability of the precise position. The High Accuracy Decision Threshold (HADT) introduced in section 6.2.3 is set at the CAT I decision threshold (200 ft). It takes 3 minutes and 25 seconds (205 s) to the aircraft to go from the 20 km starting point to the HADT.

The parameters estimated from these simulations are:

- number of trials N: it is the total number of trials performed for this configuration.
- number of solved trials N_s: it is the total number of trials for which the algorithm found an ambiguity solution.
- percentage of solved trials: it is the ratio $\frac{N_s}{N}$. This is not the integrity of the procedure as a solved trial may not have given the true solution.
- number of solved and successful trials N_{ss}: it the total number of trials for which the algorithm gave the good solution.
- success rate: it is the ratio $\frac{N_{ss}}{N}$. This is not the integrity either, as all the trials are counted, even the ones that did not converge.
- integrity: it is the ratio of the number of correct ambiguity resolutions to the total number of trials where the ambiguity was declared as solved by the procedure.
- computation time: it is the recorded number of seconds for which the CPU of the computer has executed the algorithm during the interval defined by the time of convergence.
- time of convergence: it is the acquisition time required by the procedure before delivering the ambiguities.
- number of trials longer than 205 s: this is the total number of trials that converged after the plane crossed the HADT.
- number of trials longer than 20 s: when using a pseudolite, this is the total number of trials that were not over before the plane exited the bubble.
- number of trials longer than 40 s: when using a pseudolite, this is the total number of trials that did not acquire enough measurement data, from the entrance in the bubble to the HADT, to converge.
- unavailability: it is the percentage of trials that are declared as unsolved by the procedure when the simulated aircraft crosses the High Accuracy Decision Threshold (HADT), with respect to the total number of trials performed. In our case, as explained in chapter 6.2, if the ambiguities have not been delivered by the procedure at the CAT I decision threshold, the accurate position is said to be unavailable to the pilot. The availability of the accurate position is also part of the continuity of service of the total landing system, as explained in sections 6.2.3 and 6.2.4.
- ambiguity error standard deviation: it is the standard deviation of all the ambiguity errors observed on all measurements for all the unsucessful trials.
- vertical position error (successful trials): it is the vertical position error observed at the first epoch after the ambiguities are properly solved.

- vertical position error (unsuccessful trials): it is the vertical position error observed at the first epoch after the ambiguities are solved, but are not the true ones.

The confidence interval of these estimates is very difficult to determine, as the theoretical distribution of each of the random variables estimated is unknown. However, as the number of trials ranges from 2300 to more than 20000 in some cases, it is believed that confidence up to the second digit is gained.

8.1.2 Nominal carrier phase L_1 simulated data

The observations processed are fictive L_1 carrier phase measurements affected by a white Gaussian noise. The standard deviation of this noise is set to $\sigma = 0.02$ cycle, which is approximately 4 mm. This 4mm noise level is chosen in order to evaluate the impact of nominal phase tracking errors on the performance of the AROF procedure.

These results are presented in table 8.1. The value of the a priori standard deviation of the noise is set to 0.02 cycle.

The ambiguity resolution is initiated 20 km away from the runway threshold.

	LSAST	MAPAS
# of trials N	8948	10659
# of solved N_s	8934	10656
Resolution rate $\frac{N_s}{N}$	99.84%	99,97%
# of solved and successful N_{ss}	8924	10647
Success rate $\frac{N_{ss}}{N}$	99.73%	99.89%
Integrity $\frac{N_{ss}}{N_S}$	99.89 %	99.92 %
Computation time (s)	mean: 11.21 std: 4.11 max: 26.8	mean: 13.32 std: 4.74 max: 35.75
Time of convergence (s)	mean: 19.29 std: 17.64 max: 236	mean: 16.17 std: 14.13 max: 162
# of trials N_L with duration > 205 s = 3 min and 25 s	2 (0.0224%)	0 (0%)
Unavailability of precise position $\frac{N_L+(N-N_s)}{N}$	0.179%	0.028%
Ambiguity errors std	?	5.80
Vertical position error std in m (successful trials)	0.0164	?
Vertical axis position error std in m (unsuccessful trials)	0.9603	?

Table 8.1: *LSAST/MAPAS simulation results: nominal L_1 measurements. Note that the unavailability of the precise position may be related to continuity risk (see discussion in section 6.2.3).*

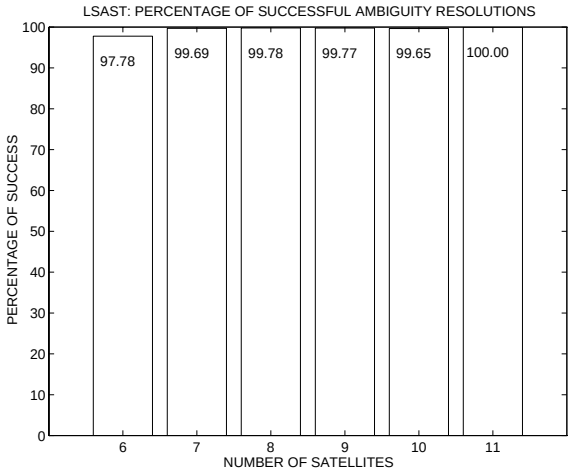

(a) *Percentage of solved trials (LSAST)*

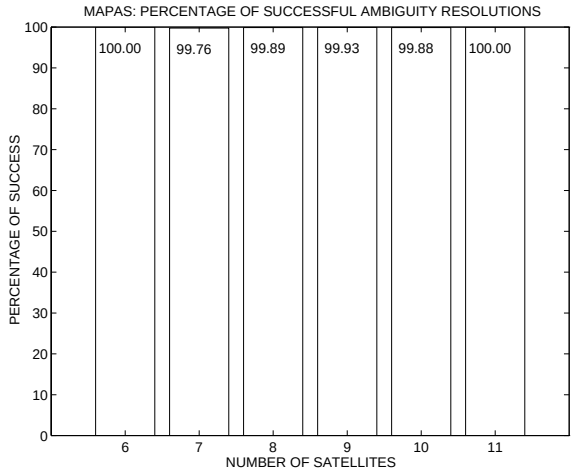

(b) *Percentage of solved trials (MAPAS)*

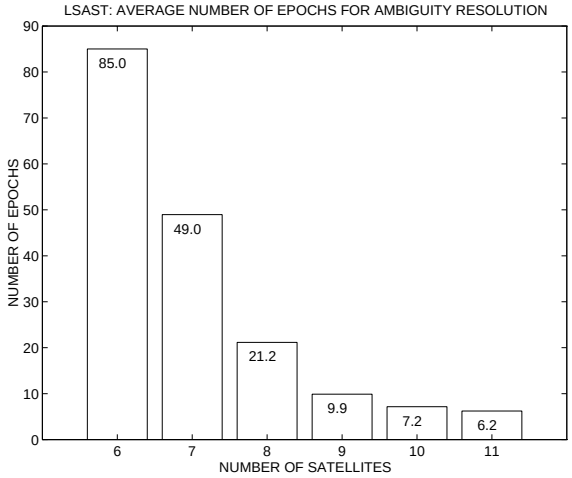

(c) *Average duration of successful trials (LSAST)*

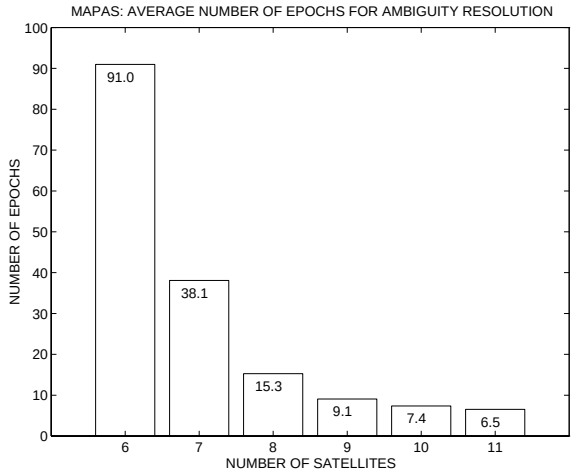

(d) *Average duration of successful trials(MAPAS)*

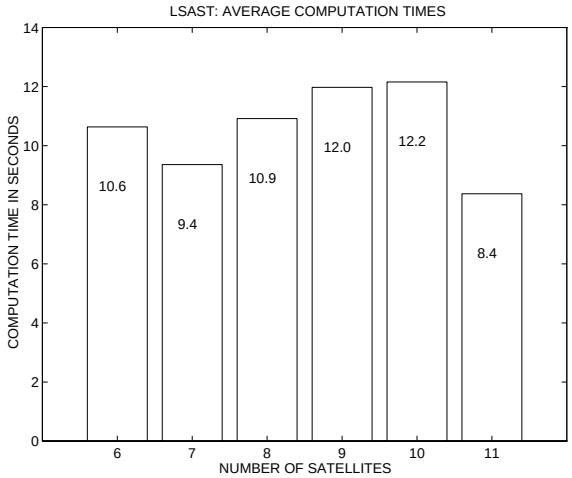

(e) *Average computation time of successful trials (LSAST)*

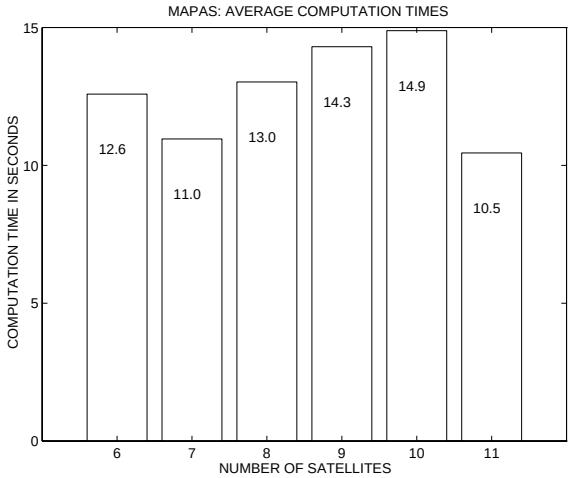

(f) *Average computation time of successful trials(MAPAS)*

Figure 8.1: *Performance of MAPAS on simulated L1 measurements*

As we can see in row 2-6 and 8 of table 8.1, and in figures 8.1(a), 8.1(b), 8.1(c) and 8.1(d), the average performance of LSAST and MAPAS are quite identical when only white noise is affecting the measurements. However, we can note that MAPAS seems to make less decision errors and to isolate the correct ambiguity more quickly. Moreover, we can see in figures 8.1(c) and 8.1(d) that there is a large improvement in the time of convergence when the number of satellite measurements increases from 6 to 11.

The average computation times required to perform the search are shown in row 7 and in figures 8.1(e) and 8.1(f). These durations represent the whole execution time of the entire resolution. The times presented here are to be used as rough indications only, as no particular effort was made to speed up the execution of the procedures. However, the trend of the evolution of these figures with the number of satellites can be analysed. As we can see in figures 8.1(e) and 8.1(f), the benefit of a larger number of observations per epoch offered by additional satellites is important only when 10 satellites are used. Before that, the gain in the ASN is not big enough to compensate the heavy volume of data processed by the computer. from our evaluation, we can also note than our MAPAS algorithm requires more computer power than LSAST.

As we can see in table 8.1, the unavailability of the precise position is quite low, although the MAPAS solution seems to have a better availability than LSAST.

We can also see in table 8.1 that the standard deviation of the position error is around 1 cm when the true solution is isolated, while it is around 1 m when wrong ambiguities are raised. This problem is due to the fact that MAPAS searches for the ambiguities of the 4 primary satellites, and then deduces the ambiguities of the secondary satellites. Therefore, a failure to raise the true primary ambiguities by one cycle on one satellite induces a large ambiguity error for the secondary satellites. The evolution of the position error induced by a 1 cycle error on one of the primary ambiguities is shown in figure 8.2(a). On the opposite, if the error made on each satellite is limited to 1 cycle, the position error is as shown in figures 8.2(b) and 8.2(c).

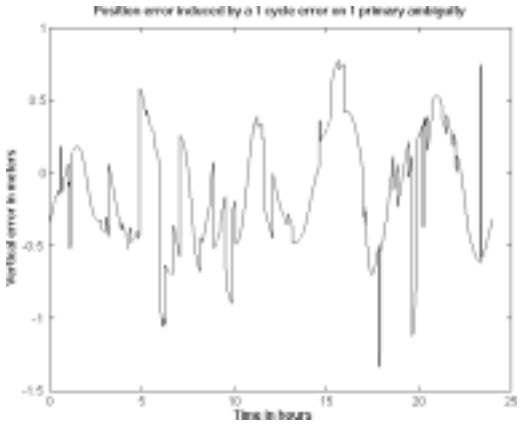

(a) *Position error induced by a 1 cycle error on one of the primary satellites.*

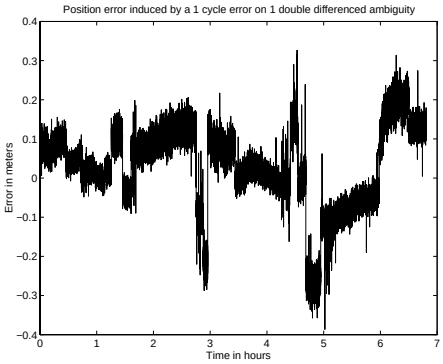

(b) *Position error induced by a 1 cycle error on one ambiguity.*

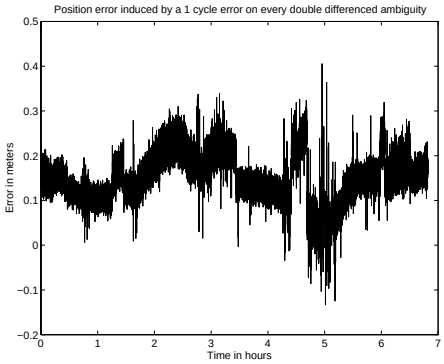

(c) *Position error induced by a 1 cycle error on every ambiguity.*

8.1.3 L1 carrier phase measurements and fixed amplitude Earth multipath

The observations processed are fictive L1 carrier phase measurements affected by a white Gaussian noise and by a fixed amplitude ground multipath. The standard deviation of the noise is set to $\sigma = 0,02$ cycle, which is approximately 4 mm. The multipath error is due to a reflected ray off the Earth's surface with a fixed relative amplitude α=0.1, which represents a nominal ground multipath. The value of the a priori standard deviation is set to 0.02 cycle, as for the previous simulation. This simulation is run in order to evaluate the impact of the multipath errors on the performance of the AROF procedure when the multipath errors are not taken into account in the assumed noise level.

These results are presented in table 8.2.

The distortions generated by the reflected ray are computed using equation 3.26. The total phase shift between both rays is assumed to be equal to the difference in path length between the reflected and the direct ray, computed using equation 3.27. The relative amplitude of the reflected signal is set to α= 0.1.

It is assumed that all the tracking channels can be affected by multipath if the delay caused by the reflection is not larger than $1.5\tau_c$, or 450 m as we assume an Early-Late delay Δ_c of 1 chip (see section 3.2). Therefore, according to (3.27) when the aircraft reaches an altitude lower than 225 m, or a distance lower than 4.3 km (=2.3 Nm) from the runway threshold, all the satellites without restriction on the elevation angle are affected by multipath. Depending on the elevation angle θ, this implies a total reflection area above the aircraft with minimal radius $\frac{h}{\tan\theta}$. Assuming a mask angle of 5^o, the largest value of the radius of this area is 2.5 km.

	LSAST	MAPAS
# trials N	9917	10533
# solved N_s	9862	10520
Percentage of solved $\frac{N_s}{N}$	99.45%	99.88%
# solved and successful N_{ss}	9810	10510
Success rate $\frac{N_{ss}}{N}$	98.92%	99.78%
Integrity $\frac{N_{ss}}{N_s}$	99.47 %	99.90 %
Computation time (s)	mean: 10.48 std: 4.18 max: 37.08	mean: 13.28 std: 4.76 max: 31.56
Time of convergence (s)	mean: 17.36 std: 14.62 max: 190	mean: 16.32 std: 14.12 max: 172
# trials N_L with duration > 205 s = 3 min and 25 s	0 (0%)	0 (0%)
Unavailability of precise position $\frac{N_L+(N-N_s)}{N}$	0.555%	0.123%
Ambiguity errors std	?	5.80
Vertical position error std in m (successful trials)	0.0198 m	?
Vertical position error std in m (unsuccessful trials)	0.7351 m	?

Table 8.2: *LSAST/MAPAS simulation results: L1 measurements and fixed amplitude Earth multipath.* Note that the unavailability of the precise position may be related to continuity risk (see discussion in section 6.2.3).

We can see in table 8.2 that there are more unsolved trials for LSAST and MAPAS than reported in table 8.1. As unsolved trials occur when the procedure ends with zero candidate left in the search set, both procedures found more inconsistent cases than in the previous configuration. However, we see that LSAST encountered more unsolved cases that MAPAS, although the integrity of MAPAS decreased less that the integrity of LSAST. As a consequence, the availability of the precise position using LSAST decreased much more than the availability of MAPAS.

We can also see in table 8.2 and in figures 8.2(f) that the time of convergence of LSAST decreased too, which means that LSAST has the tendency to decide earlier, but with more mistakes. This is a pervert effect of multipath on LSAST and MAPAS when the value of the a priori standard deviation is not adjusted: the procedures have the tendency to decide quickly, but with more mistakes.

Finally, we can see the influence of multipath on the observed position error: when the true ambiguities are solved, the vertical position error is slightly larger than in the previous case.

As we can see in table 8.2 and in figures 8.2(h) and 8.2(i), there is a very small influence of such multipath on the computation times.

Figures 8.3(c) to 8.3(f) show an example of evolution of the double differenced carrier phase prediction residuals during the simulations presented in this section. The elevation angles of satellites 6 and 28 are presented in figure 8.3(a). The characteristics of these residuals are presented in table 8.3(b).

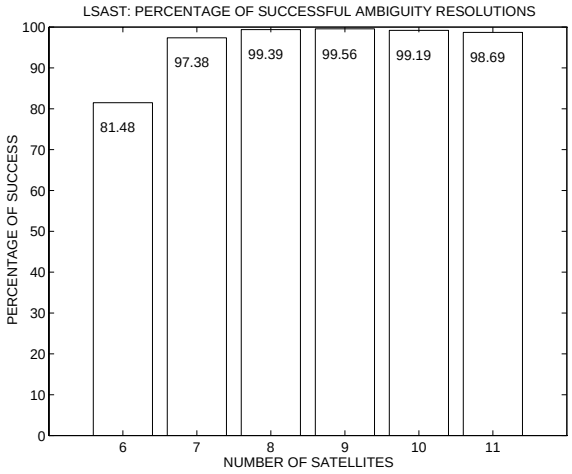

(d) *Percentage of successful trials (LSAST)*

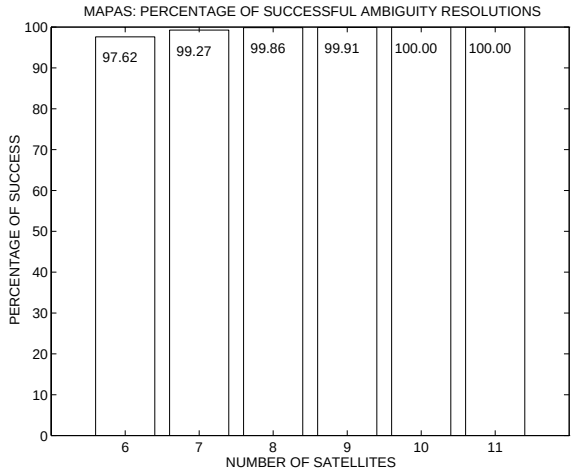

(e) *Percentage of successful trials (MAPAS)*

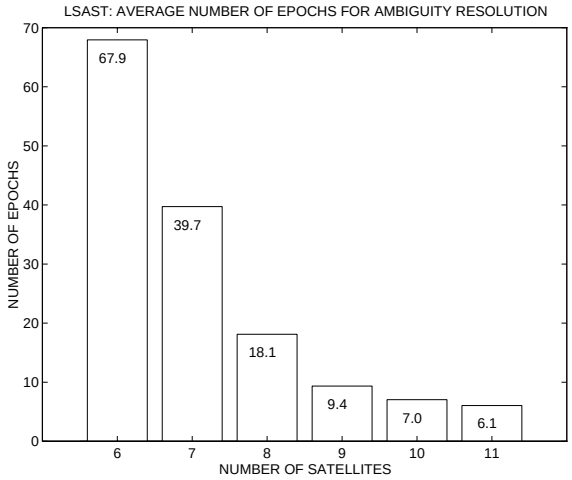

(f) *Average duration of successful trials (LSAST)*

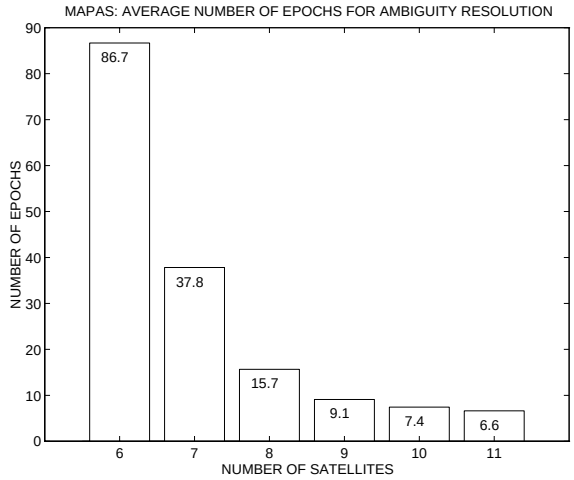

(g) *Average duration of successful trial (MAPAS)*

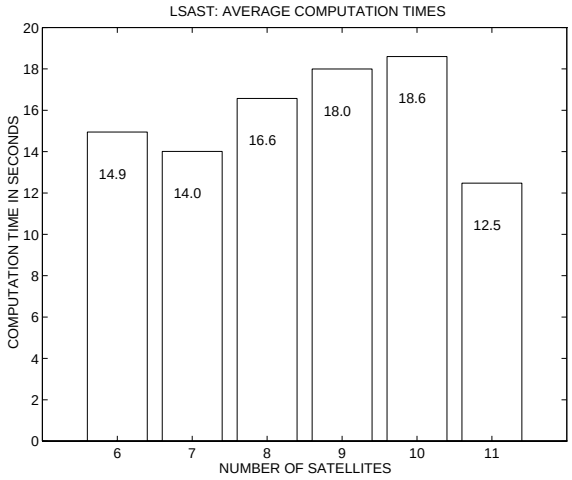

(h) *Average computation time of successful trials (LSAST)*

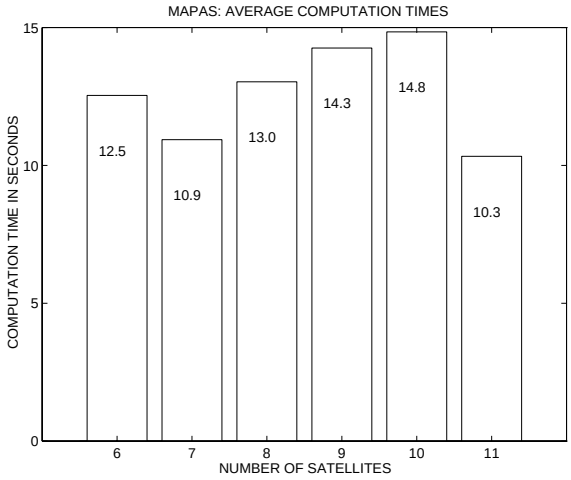

(i) *Average computation time of successful trials (MAPAS)*

Figure 8.2: *Performance of LSAST and MAPAS on simulated L1 measurements corrupted by fixed amplitude Earth multipath*

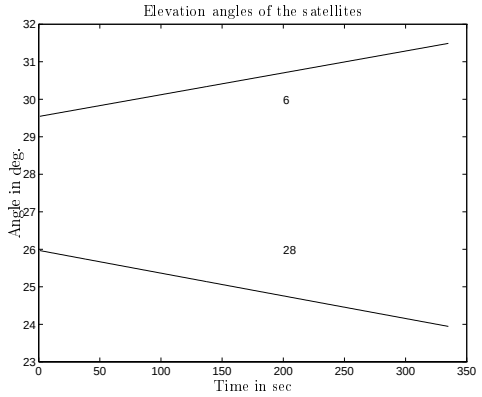

(a) *Elevation angles*

Characteristic (in cycles)	ID=6	ID=28
Mean	0.0039	0.0015
Std	0.1464	0.1334
Max	0.5469	0.3565

(b) *Characteristics of the residuals*

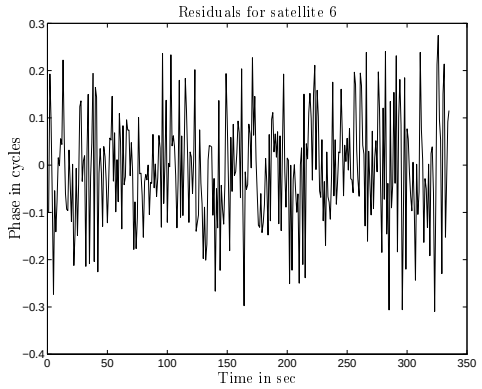

(c) *Prediction residuals for satellite 6.*

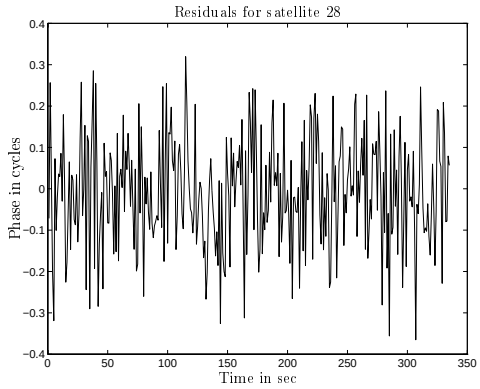

(d) *Prediction residuals for satellite 28.*

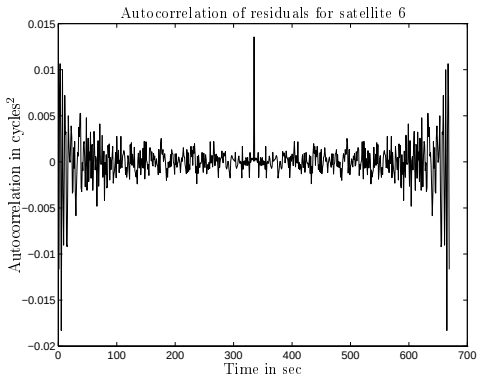

(e) *Autocorrelation of prediction residuals for satellite 6.*

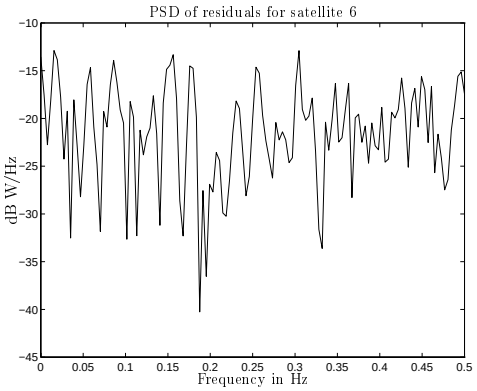

(f) *Power spectral density of prediction residuals for satellite 6.*

Figure 8.3: *Characteristics of double differenced prediction residuals with fixed amplitude Earth multipath.*

As we can see in table 8.3(b), the double differenced prediction residuals have a quite large amplitude as compared to the inserted undifferenced phase measurement error of 0.02 cycle. Nevertheless, as we can see from figures 8.3(e) and 8.3(f), we can still assume that these residuals have a white noise distribution, which is very important to the procedure.

8.1.4 L1 phase measurements and variable amplitude Earth multipath

The observations processed are fictive L1 carrier phase measurements affected by a white Gaussian noise with standard deviation $\sigma = 0.02$ cycle, which is approximately 4 mm, and distorted by an error due to a reflected ray off the Earth's surface with a relative amplitude determined by the soil reflection coefficient, antenna gain and the rejection by the code correlator. These results are presented in table 8.3. The value of the a priori standard deviation is set to 0.02 cycle.

The distortions introduced by the reflected ray are computed using equation E.6:

- The total path delay δs between the reflected ray and the direct ray is computed using (3.27). The total phase rotation $\delta\varphi_1 = \varphi_1 - \varphi_0$ between both rays is computed by adding δs to the phase rotation introduced by the Earth's surface. This phase rotation is obtained through the computation of α using classical reflection coefficient expressions.
- The relative amplitude of the carrier of the reflected ray α_1 is the product of
  - $\mid R \mid$, the module of the soil reflection factor. We have $\mid R \mid = \sqrt{R_r^2 + R_i^2}$, with $R_r = \frac{R_{\perp r} - R_{\parallel r} \times sin\theta}{2}$ and $R_i = \frac{R_{\perp i} - R_{\parallel i} \times sin\theta}{2}$. The reflecting soil is characterized by its dielectric properties. We chose here to model a wet soil, with ε_r=12 and σ_r=0.4.
  - the inverse value of the gain of the mobile antenna in the direction of the direct ray, as indicated in figure 8.4. When the algorithm detects that the reflected ray has a Left-Hand Circular polarization, the module of α is lowered by an additional 10 dB, as real GPS antennas usually present an attenuated LHCP radiation pattern.
  - the ratio of the direct and composite signals correlation factors, as indicated in formula (E.2). This ratio is estimated assuming that the error of estimation of the propagation time τ_0 is the weighted relative delay of the refelcted ray by its relative amplitude: it is assumed that $\hat{\tau} - \tau_0 = a\delta\tau$ with $\delta\tau = \tau_1 - \tau_0$. Therefore, the ratio of both correlation coefficients can be approximated as $\frac{R(\hat{\tau}-\tau_1)}{R(\hat{\tau}-\tau_0)} = \frac{R((\frac{\alpha}{2}-1)*\delta\tau)}{R(\frac{\alpha}{2}\delta\tau)}$.

As for section 8.1.3, all the satellites are assumed to be affected by multipath if the relative delay of the reflected ray is lower than $1.5 \times \Delta_c$, or 450m considering an Early-Late delay Δ_c of 1 chip.

Such a simulation is not a realistic simulation of real multipath, as the reflection coefficient are pessimistic and the visibility of the antenna is reduced. Indeed, in reality the surface of the soil is not smooth, which generates an equivalent diminution of the reflection coefficient. Moreover, the real antenna is mounted on the top of the aircraft, and can it can only be reached by creeping rays. Therefore, the simulations that were run are globally pessimistic, but more realistic simulations are very difficult to implement.

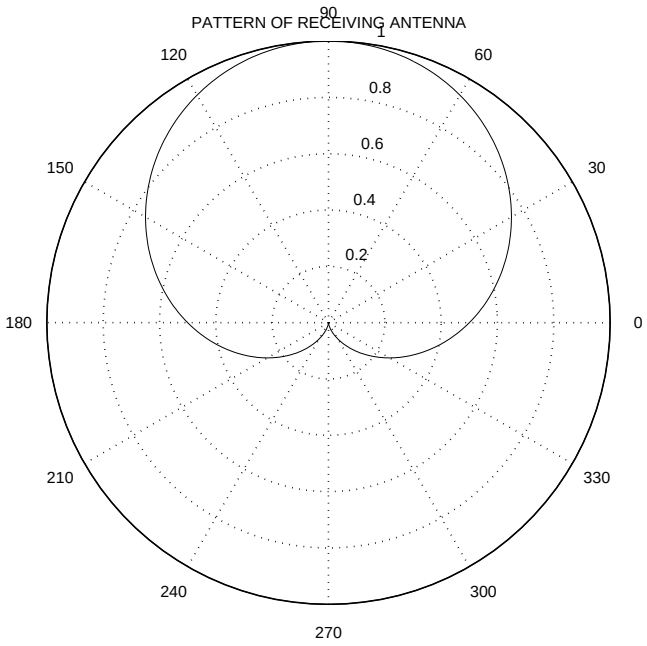

Figure 8.4: *Pattern of simulated mobile antenna.*

	LSAST	MAPAS
# trials N	19730	10533
# solved trials N_r	7202	8997
Percentage of solved trials $\frac{N_s}{N}$	36.50%	85.32%
# solved and successful trials N_{ss}	4138	7322
Success rate $\frac{N_{ss}}{N}$	20.97%	69.51%
Integrity $\frac{N_{ss}}{N_s}$	57.46 %	81.47 %
Computation time (s)	mean: 3.56 std: 5.2 max: 28.84	mean: 11.32 std: 6.46 max: 35.81
Time of convergence (s)	mean: 9.18 std: 5.56 max: 135	mean: 14.45 std: 10.70 max: 188
# trials N_L with duration > 205 s = 3 min and 25 s	0 (0%)	0 (0%)
Unavailability of precise position $\frac{N_L+(N-N_s)}{N}$	63.50%	14.68%
Ambiguity errors std	?	5.80
Vertical position error std in m (successful trials)	0.0437 m	?
Vertical position error std in m (unsuccessful trials)	0.5306 m	?

Table 8.3: *LSAST/MAPAS simulation results: L1 measurements and variable ground multipath.* Note that the unavailability of the precise position may be related to continuity risk (see discussion in section 6.2.3).

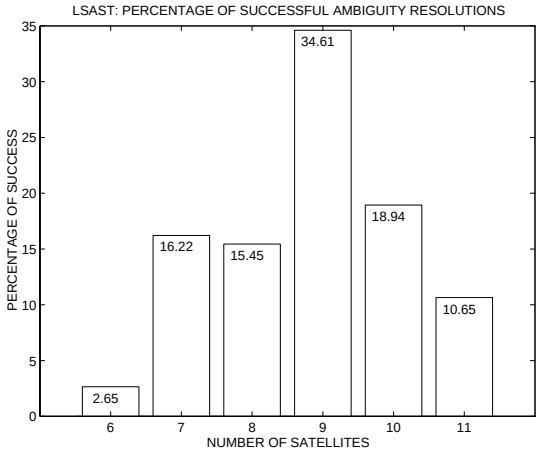

(a) *Percentage of successful trials (LSAST)*

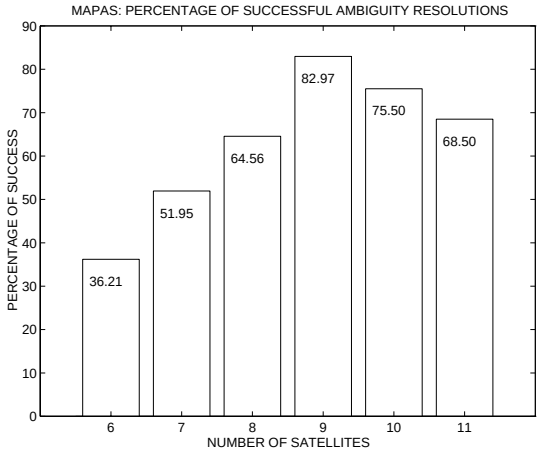

(b) *Percentage of successful trials (MAPAS)*

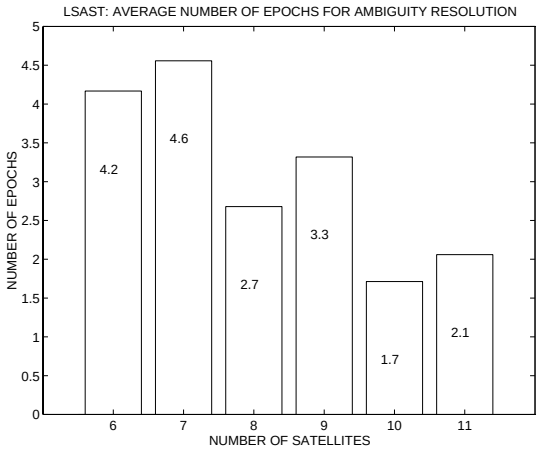

(c) *Average duration of successful trials (LSAST)*

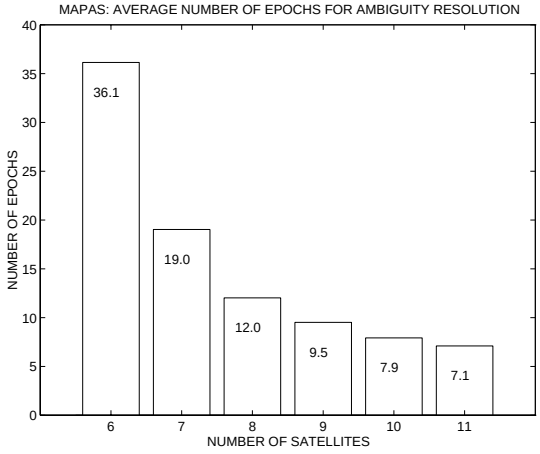

(d) *Average duration of successful trials (MAPAS)*

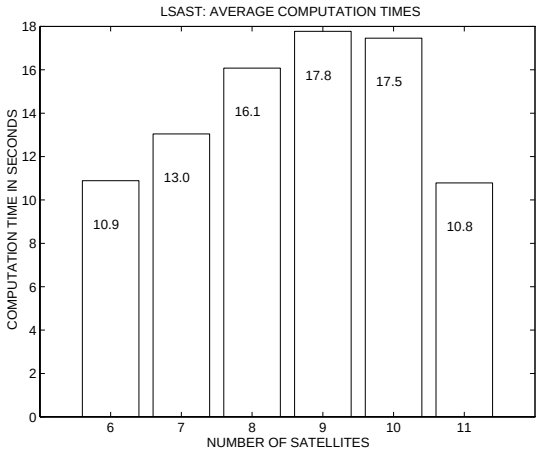

(e) *Average computation time of successful trials (LSAST)*

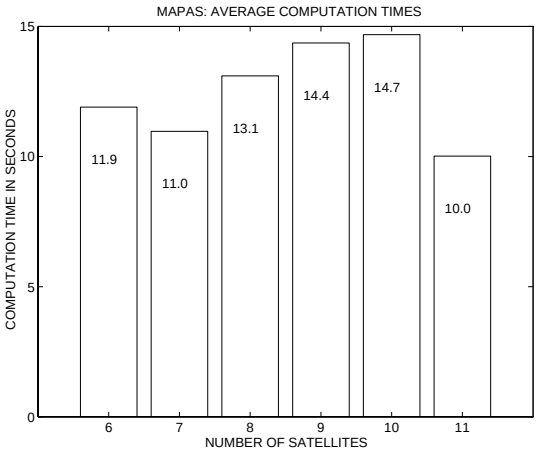

(f) *Average computation time of successful trials (MAPAS)*

Figure 8.5: *Performance of LSAST and MAPAS on simulated L1 measurements corrupted by variable amplitude Earth multipath.*

Comparing table 8.2 with table 8.3, we see that the number of unsolved trials increased. About half of the LSAST trials are unsolved, while 85 % of MAPAS trials remain solved. Similarly, the integrity of LSAST is around 57 %, while the integrity of MAPAS is around 82 %. This leads to a very high unavailability for LSAST, and a lower, but still unacceptable availability for MAPAS. Furthermore, we see that both procedures have a tendency to decide very quickly, though making many mistakes. If we look at figure 8.5(a) and 8.5(b), the procedures are highly affected when the number of satellites is lower than 9 because of the low redundancy in the measurements, and when it is higher than 9 because in that case many satellite signals are affected by multipath.

We also note that the vertical position error hase increased, and is now around 4 cm when the true ambiguities are raised. We must also note that LSAST does not make big mistakes when raising wrong ambiguities, as the vertical position error is around 50 cm in that case.

Figures 8.6(b) to 8.6(e) show an example of the evolution of these residuals during the simulations presented in this section. The elevation angles of satellites 6 and 28 are presented in figure 8.3(a). The characteristics of these residuals are presented in table 8.6(a).

Characteristic (in cycles)	ID=6	ID=28
Mean	-0.0098	-0.0076
Std	0.1162	0.1319
Max	0.2743	0.3195

(a) *Characteristics of residuals*

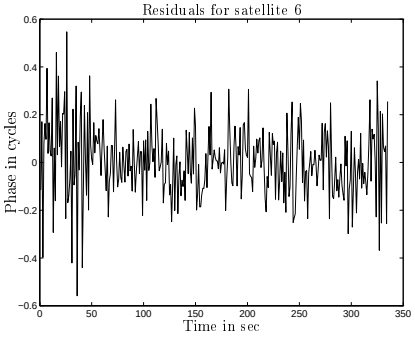

(b) *Prediction residuals for satellite 6.*

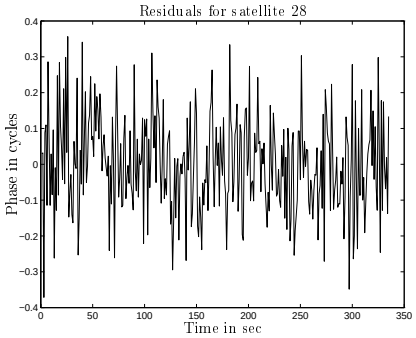

(c) *Prediction residuals for satellite 28.*

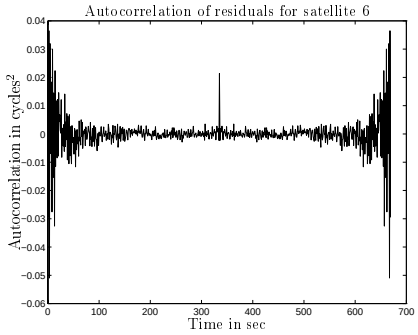

(d) *Autocorrelation of prediction residuals for satellite 6.*

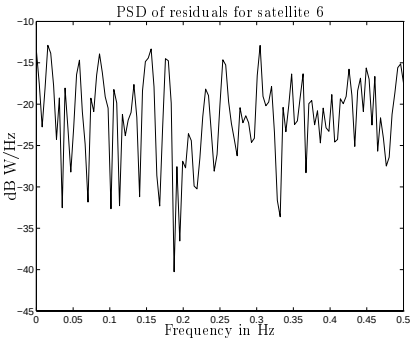

(e) *Power spectral density of prediction residuals for satellite 6.*

Figure 8.6: *Characteristics of prediction residuals of measurements corrupted by Earth multipath.*

When comparing the standard deviation obtained in table 8.6(a) with the standard deviation obtained in table 8.3(b), we see that the residuals are of the same order, although they seem to be statistically lower in the second, more realistic case than in the first one. We also note that the residuals can still be considered as having a white noise distribution.

8.1.5 L1 measurements and variable amplitude Earth multipath (with adaptation of prior variance)

The observations processed are fictive L1 carrier phase measurements affected by a white Gaussian noise with standard deviation $\sigma = 0.02$ cycle, which is approximately 4 mm, and distorted by an error due to a reflected ray off the Earth's surface with a relative amplitude determined by the soil reflection coefficient, antenna gain and the rejection by the code correlator. These results are presented in table 8.4). The value of the a priori standard deviation is set to 0.04 cycle, or approximately 8 mm.

These simulations were run in order to assess the improvement in the performance of the AROF procedure when taking multipath into account in the noise level. This adaptation of the noise level to include all the distortions is a common practice, although it is known that the assumed gaussian distribution is not correct. In our case, the adaptation was done by assuming a noise level of 0.04 cycle when the tracking noise level is 0.02 cycle. Nevertheless, the assumed noise level is still too weak, as the total noise level is around 0.12 cycle as shown in table 8.6(a).

	LSAST	MAPAS
# trials N	2363	5173
# solved trials N_s	2229	5041
Percentage of solved trials $\frac{N_s}{N}$	94.33%	99.46%
# solved and successful trials N_{ss}	2090	5041
Success rate $\frac{N_{ss}}{N}$	88.45%	97.45%
Integrity $\frac{N_{ss}}{N_s}$	93.76 %	97.98 %
Computation time (s)	mean: 14.26 std: 7.17 max: 52.56	mean: 15.94 std: 5.38 max: 40.50
Time of convergence (s)	mean: 37.27 std: 32.80 max: 361	mean: 33.24 std: 29.00 max: 292
# trials N_L with duration > 205 s = 3 min and 25 s	5 (0.212%)	6 (0.116%)
Unavailability of precise position $\frac{N_L+(N-N_s)}{N}$	5.883%	0.657%
Ambiguity error std	?	5.80
Vertical position error std in m (successful trials)	0.0437 m	?
Vertical position error std in m (unsuccessful trials)	0.5306 m	?

Table 8.4: *LSAST/MAPAS simulation results: L1 measurements and variable amplitude Earth multipath (with adapted prior variance). Note that the unavailability of the precise position may be related to continuity risk (see discussion in section 6.2.3).*

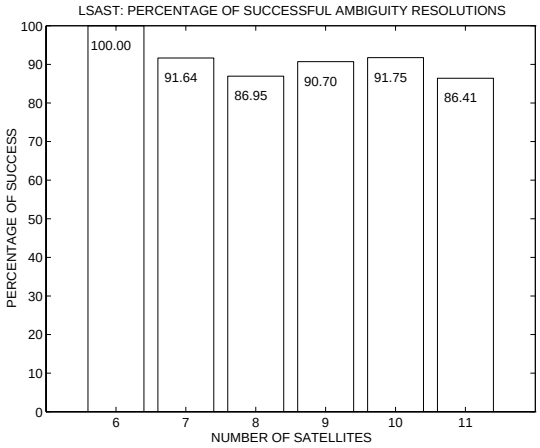

(a) *Percentage of successful trials (LSAST)*

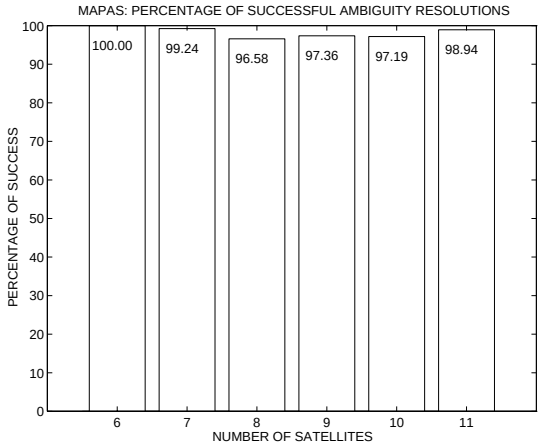

(b) *Percentage of successful trials (MAPAS)*

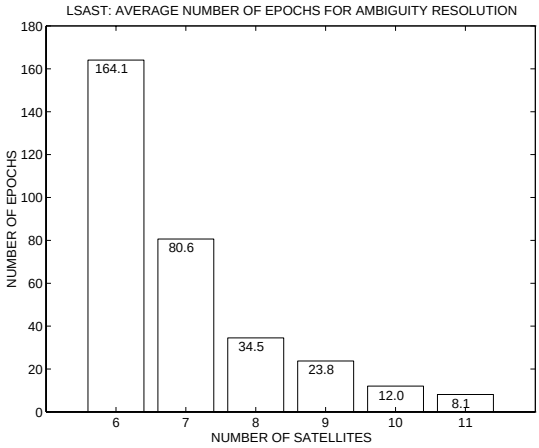

(c) *Average duration of successful trials (LSAST)*

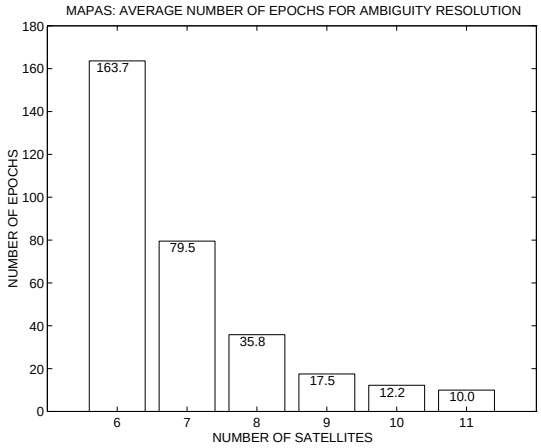

(d) *Average duration of successful trials (MAPAS)*

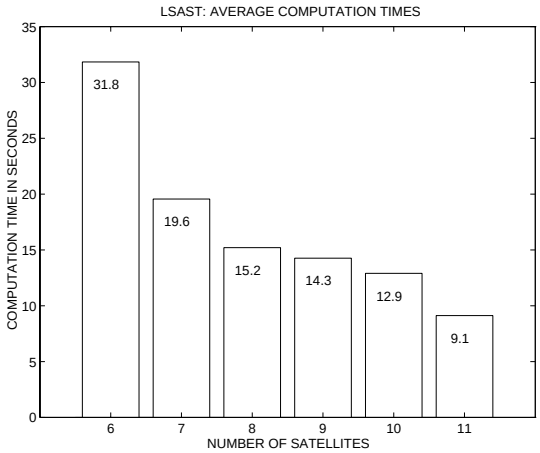

(e) *Average computation time of successful trials (LSAST)*

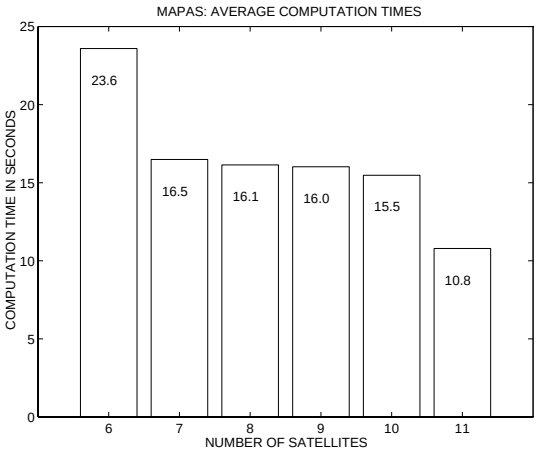

(f) *Average computation time of successful trials (MAPAS)*

Figure 8.7: *Performance of LSAST and MAPAS on simulated L1 measurements corrupted with variable amplitude Earth multipath, with adapted prior variance.*

When comparing the results presented in table 8.3 with the results presented in table 8.4, we see the number of unsolved trials decreased significantly, and that the observed integrity has improved, although the integrity of LSAST is still only around 88 %. The availability of both procedures improved, but LSAST still has an unavailability of around 6 %.

The consequence of the adaptation of the prior variance to account for multipath is the increase of the time of convergence, as MAPAS and LSAST now converge in about 30 s, as compared to the average 15 s reported in table 8.1.

The vertical position errors are identical to the position errors observed in table 8.3.

As we can see in figures 8.7(c) and 8.7(d), the resolution takes a very long time when the number of satellites is 6 or 7, because of the adaptation of the prior variance of the noise. But we can note that the trend observed on the figures 8.7(e) and 8.7(f) is different from the trends observed previously, as the computation time decreases with the number of tracked satellites. This is mainly due to the increase in the time of convergence for a low number of satellites, which cancels the benefit of having few observations per epoch.

8.1.6 L1 measurements and 1 pseudolite

The observations processed are fictive L1 carrier phase measurements affected by a white Gaussian noise with standard deviation $\sigma = 0.02$ cycle, which is approximately 4 mm. The GPS satellite constellation is augmented by a pseudolite located 3 km away from the runway threshold, offset by 100 m from the centerline. This pseudolite has a coverage radius of 700 m. A plane flying 120 kts (62 m.s^{-1}) crosses the bubble in 20 s. It takes the aircraft 40 s before reaching the CAT I decision threshold (200 ft) since the time he entered the bubble, as presented in figure 8.8. The ambiguity resolution trials start when the plane enters the bubble. These results are presented in table 8.5. The value of the a priori standard deviation is set to 0.02 cycle, or approximately 4 mm.

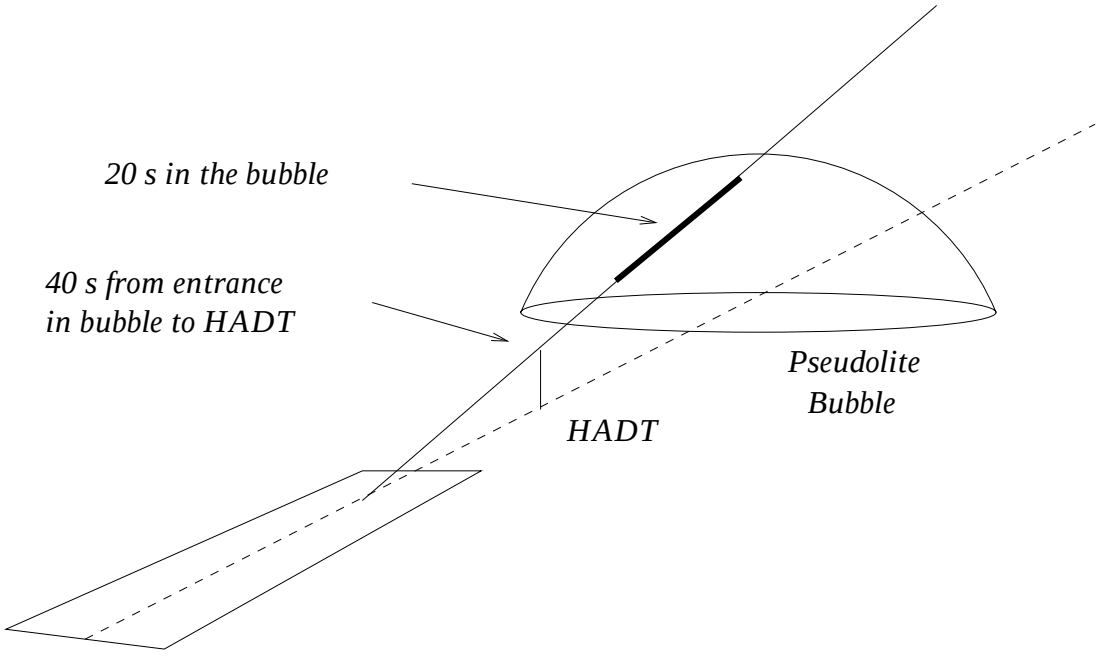

Figure 8.8: *Coverage of bubble pseudolite.*

	LSAST	MAPAS
# trials N	16034	16930
# solved trials N_s	16014	16929
Percentage of solved trials $\frac{N_s}{N}$	99.88%	99.99%
# solved and successful trials N_{ss}	15984	16915
Success rate $\frac{N_{ss}}{N}$	99.69%	99.91%
Integrity $\frac{N_{ss}}{N_s}$	99.81 %	99.92 %
Computation time (s)	mean: 12.92 std: 5.90 max: 48.89	mean: 14.81 std: 6.20 max: 43.11
Time of convergence (s)	mean: 10.77 std: 8.65 max: 215	mean: 10.19 std: 6.54 max: 152
# trials with duration $>$ 20 s	1209 (7.54%)	678 (4.00%)
# trials with duration $>$ 40 s N_L	343 (2.14%)	160 (0.945%)
Unavailability of precise position $\frac{N_L+(N-N_s)}{N}$	2.26%	0.951%
Ambiguity error std	3.87	?
Vertical position error std in m (successful trials)	0.0067 m	?
Vertical position error std in m (unsuccessful trials)	0.9069 m	?

Table 8.5: *LSAST/MAPAS simulation results: L1 measurements and 1 pseudolite.* Note that the unavailability of the precise position may be related to continuity risk (see discussion in section 6.2.3).

If we compare table 8.1 with table 8.5, we see that the percentage of solved trials has slightly increased, although the resulting integrity is about the same. The main improvement is seen on the time of convergence, which is almost divided by 2, going down to around 7 s. However, we see that in the configuration simulated here, where the ambiguity resolution is initiated at the entrance in the bubble, the availability of the precise position is lower than in the first case, where no pseudolite is transmitting, and the resolution starts 20 km away from the runway. This is due to the severe restriction of the allowed time of convergence, going from 205 s to 40 s. We also note that the standard deviation of the ambiguity errors is smaller, and that the vertical position error in the successful case is lower than 1 cm, but it is around 90 cm if the wrong ambiguities are raised The other change to be noted is the increase of the computation time required to handle the extra measurement provided by the pseudolite.

Comparing figures 8.1(a)-8.1(f) with figures 8.9(a)-8.9(f), we see that the distribution of the parameters over the number of satellites has the same trend.

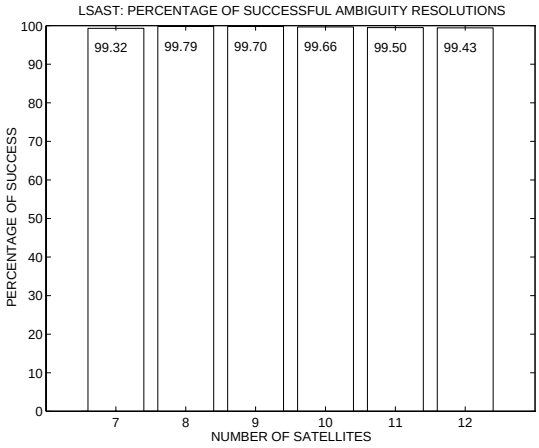

(a) *Percentage of successful trials (LSAST)*

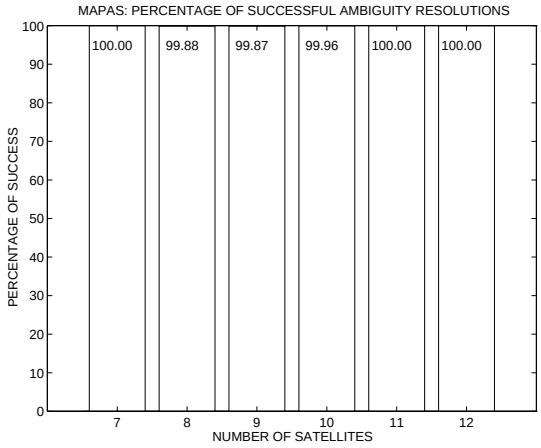

(b) *Percentage of successful trials (MAPAS)*

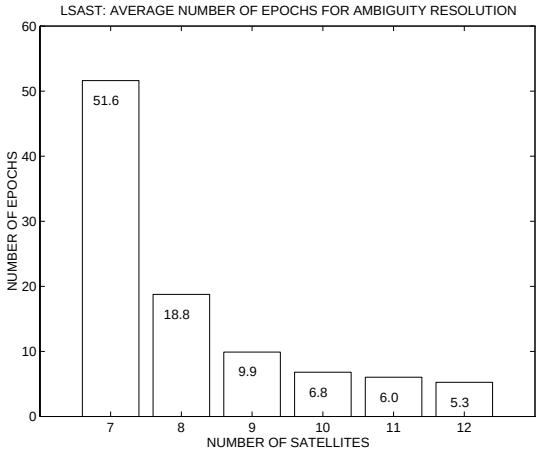

(c) *Average duration of successful trials (LSAST)*

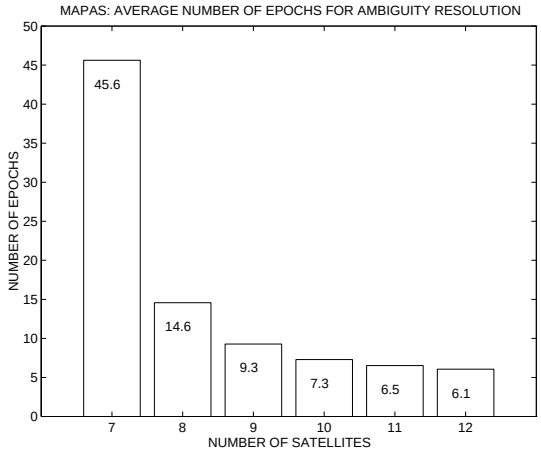

(d) *Average duration of successful trials (MAPAS)*

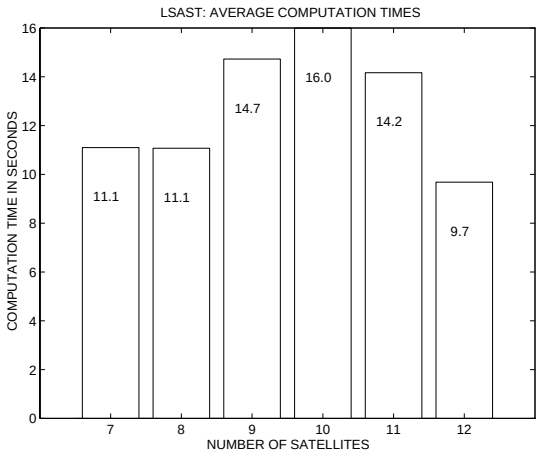

(e) *Average computation time of successful trials (LSAST)*

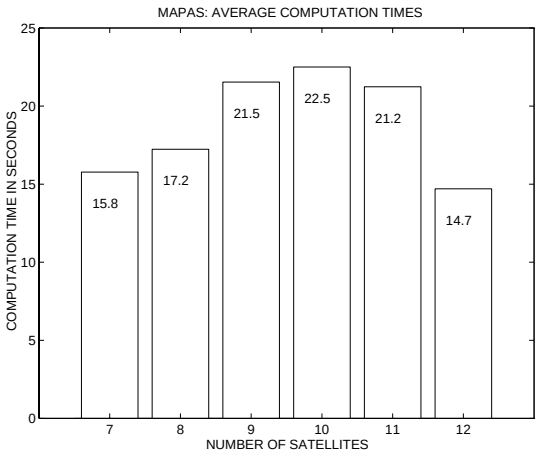

(f) *Average computation time of successful trials (MAPAS)*

Figure 8.9: *Performance of LSAST and MAPAS on simulated L1 measurements augmented with 1 pseudolite.*

8.1.7 L1 measurements and 2 pseudolites

The observations processed are fictive L1 carrier phase measurements affected by a white Gaussian noise with standard deviation $\sigma = 0.02$ cycle, which is approximately 4 mm. The GPS satellite constellation is augmented by 2 pseudolites located 3 km away from the runway threshold, offset by 100 m on each side of the centerline. These pseudolites have a coverage radius of 700 m. A plane flying 120 kts (62 m.s^{-1}) crosses their bubble in 20 s. It takes the aircraft 40 s before reaching the CAT I decision threshold (200 ft) since the time he entered the bubble. The ambiguity resolution trials start when the plane enters the bubble. These results are presented in table 8.6. The value of the a priori standard deviation is set to 0.02 cycle, or approximately 4 mm.

	LSAST	MAPAS
# trials N	20603	19751
# solved trials N_s	20545	19751
Percentage of successful trials $\frac{N_s}{N}$	99.72%	100%
# solved and successful trials N_{ss}	20508	19734
Success rate $\frac{N_{ss}}{N}$	99.54%	99.91%
Integrity $\frac{N_{ss}}{N_s}$	99.82 %	99.91 %
Computation time (s)	mean: 14.67 std: 6.68 max: 72.68	mean: 17.15 std: 6.16 max: 53.79
Time of convergence (s)	mean: 8.39 std: 5.77 max: 98	mean: 8.61 std: 4.42 max: 103
# trials with duration > 20 s	650 (3.15%)	327 (1.66%)
# trials with duration > 40 s N_L	159 (0.77%)	70 (0.3544%)
Unavailability of precise position $\frac{N_L+(N-N_s)}{N}$	1.0532%	0.3544%
Ambiguity error std	3.3805	6.06
Vertical position error std in m (successful trials)	? m	?
Vertical position error std in m (unsuccessful trials)	0.8648 m	

Table 8.6: *LSAST/MAPAS simulation results: L1 measurements and 2 pseudolites.* Note that the unavailability of the precise position may be related to continuity risk (see discussion in section 6.2.3).

Comparing table 8.5 with table 8.6, we see that there is no significant improvement in the percentage of solved trials and in the integrity of the procedures. However, we note that the time of convergence is improved, and is now around 5 s. This also improves the availability of the precise position, with a similar computation time. We also note that the vertical position error is slightly improved when the wrong ambiguities are raised. The general trends observed in figures 8.10(a)-8.10(f) is similar to the trend of the previous figures.

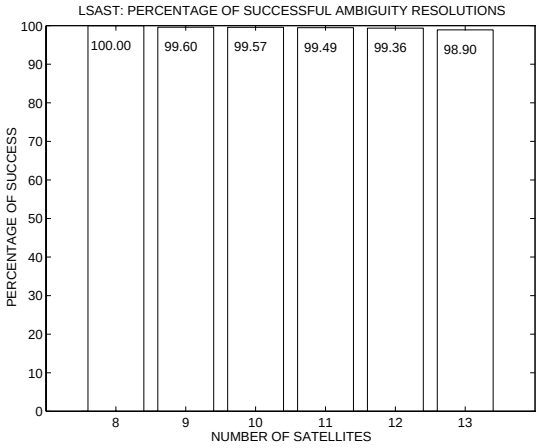

(a) *Percentage of successful trials (LSAST)*

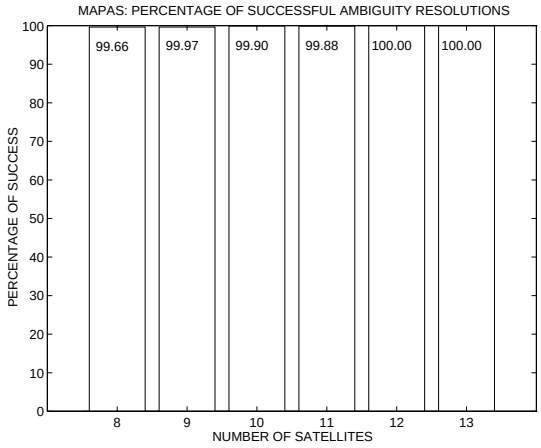

(b) *Percentage of successful trials (MAPAS)*

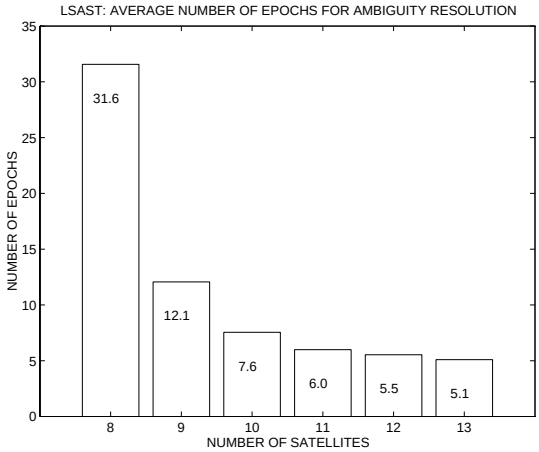

(c) *Average duration of successful trials (LSAST)*

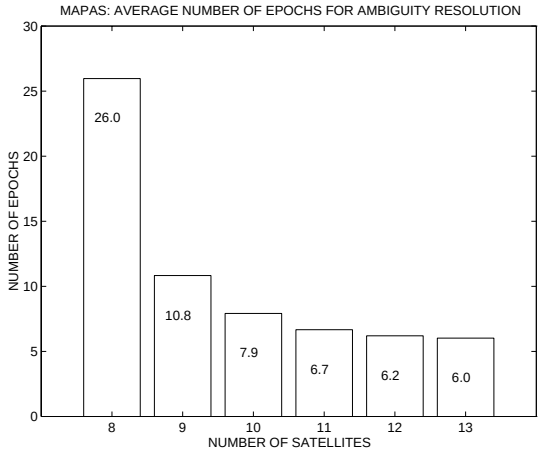

(d) *Average duration of successful trials (MAPAS)*

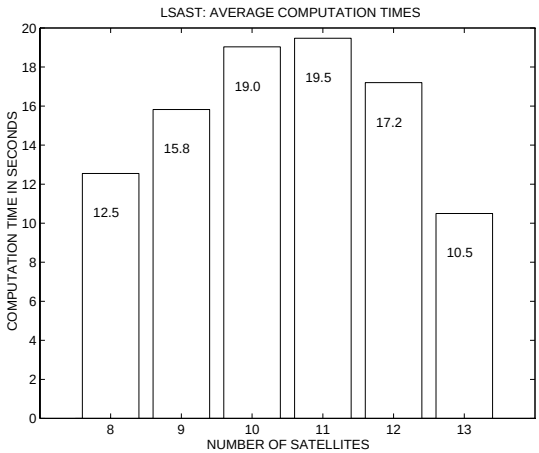

(e) *Average duration of successful trials (LSAST)*

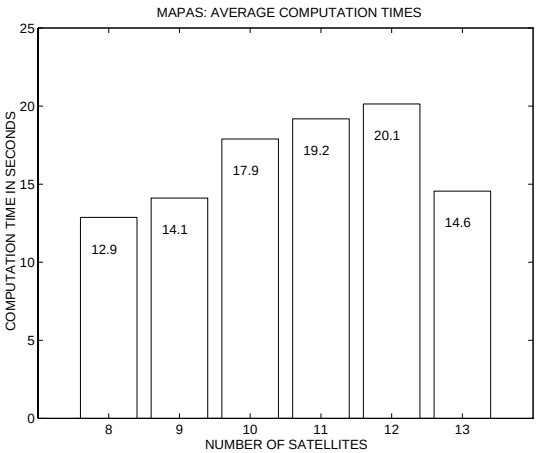

(f) *Average duration of successful trials (MAPAS)*

Figure 8.10: *Performance of LSAST and MAPAS on simulated L1 measurements augmented with 2 pseudolites.*

#	Applied noise level	Distance of aircraft	Pseudolites	Multipath
1	1 mm	10 km	N/A	N/A
2	1 mm	10 km	1	N/A
3	2 mm	10 km	N/A	yes
4	2 mm	10 km	1	yes
5	2 mm	10 km	N/A	yes
6	2 mm	20 km	1	yes
7	4 mm	20 km	N/A	N/A
9	2 mm	10 km	N/A	N/A

Table 8.7: . *Configuration of scenarios run by SEXTANT AVIONIQUE for DIAS and FASF.*

#	DIAS Integrity	DIAS Availability of precise position	FASF Integrity	FASF Availability of precise position
1	96.48	90.01	99.53	93.93
2	98.7	96.4	N/A	N/A
3	91.2	31.8	97.9	46.8
4	97.14	44.3	97.8	60.8
5	93.33	80.3	96.5	89.9
6	94.2	86.7	98.5	93.7
7	97.1	88.2	100	85.5
8	90.06	83.4	99.3	78.3
9	99.22	90.1	N/A	N/A

Table 8.8: *Simulation results obtained by SEXTANT AVIONIQUE on DIAS and FASF.*

8.2 Performance of DIAS and FASF on simulated data

The performance of the DIAS and FASF algorithms was evaluated by SEXTANT AVIONIQUE using a methodology similar to the approach chosen by the LTST. The scenarios run are defined in table 8.7.

The results obtained are gathered in table 8.8.

8.3 Summary and discussion on simulation results

The results presented in sections 8.1 and 8.2 can only be interpreted as comparisons between methods in the same category, following the classification presented in section 5.1. As LSAST and MAPAS were implemented and compared by the LTST, and DIAS and FASF were implemented and compared by SEXTANT AVIONIQUE, differences in software design and simulation parameters prevent a systematic comparison of performance of decision and estimation methods. The differences in software design concern thresholds settings, that were adjusted by two different teams, both performing trade-offs between the error probability and the time of convergence. The differences between the simulation parameters are presented in table 8.9. It must also be noted that the computation times were given as indications only, as no particular effort was made to optimize the computations.

Methods	LSAST, MAPAS	DIAS, FASF
Noise level	4 mm	1 mm, 2 mm or 4 mm as indicated
Starting point of flight path	20 km	10 km or 20 km as indicated
Multipath	All visible satellites	Highest visible satellite
Pseudolites	700 m radius bubbles @ 3 km from runway threshold	Coverage extended to all the approach path

Table 8.9: *Differences between the LTST and SEXTANT AVIONIQUE simulation parameters.*

The estimated performance of LSAST and MAPAS is summarized in figure 8.11 and 8.12.

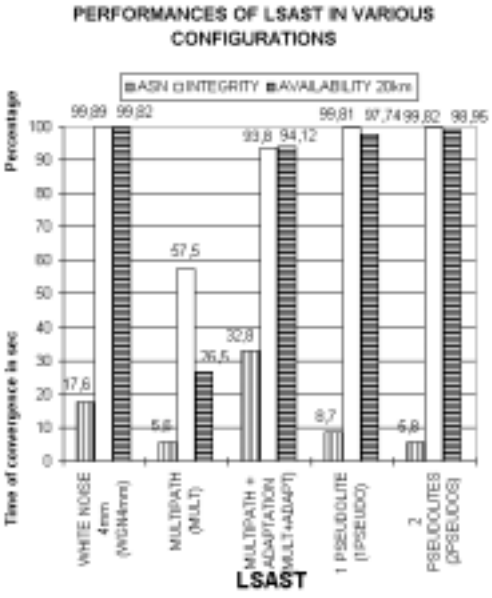

Figure 8.11: *Summary of LSAST simulation results*

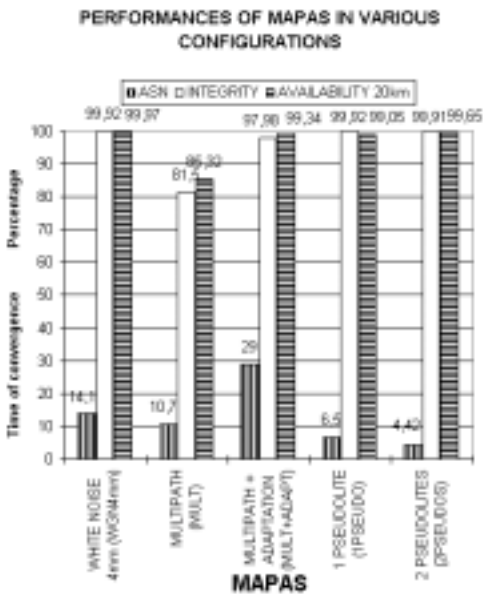

Figure 8.12: *Summary of MAPAS simulation results*

We can deduce from the observation of these graphs that the estimated performance of these two methods is quite identical when no additional perturbation is added to the measurements (see bar plot WGN4mm on figures 8.11 and 8.12). But the influence of multipath is dramatic (MULT), as the reliability of both methods drops significantly, although it can be improved by setting a higher a priori noise level than the inserted one (MULT+ADAPT). However, we can see that MAPAS seems to show a better resistance to multipath than LSAST, probably because of its rejection mechanism which is direclty performed on probability criteria and not on χ^2 thresholds. This difference is presented in detail in [MAC96]. The benefit of the addition of bubble pseudolite signals is visible as well, mainly on the estimated time of convergence (1PSEUDO, 2 PSEUDOS). However, we can see that the impact of this addition on the integrity and availability of the procedures is not significant in this case where the pseudolite signal noise level is similar to the satellite signal noise level, not even when adding one extra pseudolite. Note that we can expect a higher benefit when using pseudolites radiating signals having a larger coverage than a 700 m radius bubble, as it was done for DIAS and FASF testing by SEXTANT AVIONIQUE.

The estimated performance of DIAS and FASF is presented in figures 8.13 and 8.14.

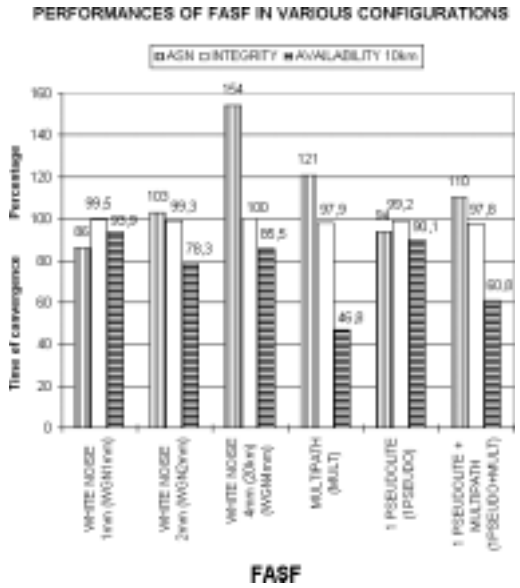

Figure 8.13: *Summary of FASF simulation results*

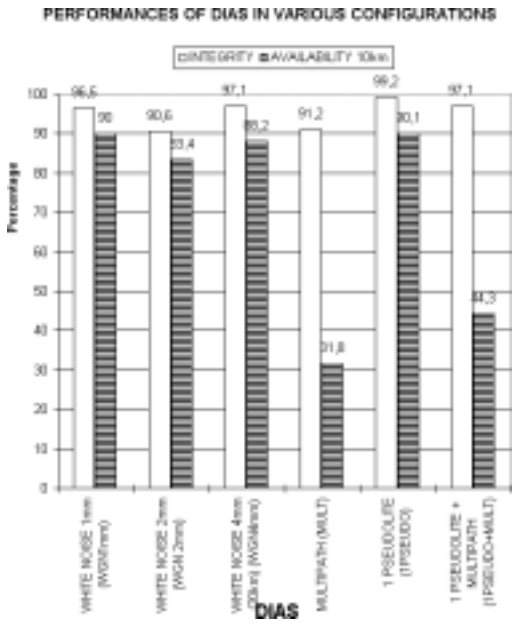

Figure 8.14: *Summary of DIAS simulation results*

Stricly speaking, the error probability reported here cannot be directly interpreted as the integrity risk because DIAS and FASF offer the possibility to deliver floating point ambiguities that can be used to compute a precise position. However, as noted in section 8.2, a failure to raise the true ambiguities is almost always associated with an approximate position error of 1 m. Therefore, the error probability reported in figures 8.13 and 8.14 can be interpreted as the integrity risk.

As we can see from the first results presented in these figures, FASF seems to have a better error probability and availability than DIAS when only white noise is affecting the measurements (WGN1mm, WGN2mm, WGN4mm). As reported earlier about LSAST and MAPAS, multipath induced errors seriously affect the performance of the procedures, with an advantage to FASF, that seems to have a better resistance to that type of unmodeled errors (MULT). Similarly, the influence of the addition of a pseudolite measurement is not very high, improving only the availability of the methods (1PSEUDO), even when multipath is added (1PSEUDO+MULT).

This first set of results enables to draw several conclusions about the performance of these methods. First of all, we see that the influence of multipath induced errors is dramatic. This is a direct consequence of the measurement model used by all these procedures, that does not include multipath. Then, we can deduce from these first simulations that compliance to integrity requirements is far from being satisfied. Furthermore, the benefit of adding one or two pseudolite measurements is not significant when the noise level on the pseudolite signal is identical to the noise level on the GPS signals. When the satellite signal is affected by multipath, as in simulation number 6 for example, there is a slight improvement in integrity and availability of the precise position. Finally, according to the simulations performed, MAPAS and FASF seem to have better performance than the other tested procedures, which certainly has to do with the smoothness of their selection process.

Further comparison of MAPAS and FASF was done by SEXTANT AVIONIQUE by incorporating typical multipath errors and tropospheric residuals in carrier phase measurements. It results from these additional evaluations that the availability of the precise position using FASF is highly affected by multipath and biased residuals, while MAPAS sees its integrity decreased in the same conditions. However, it is anticipated that improvement of the robustness of MAPAS can be achieved. From all the analysis performed at this point, presented in [MBJ+97] and gathered in table 8.3, MAPAS is

selected as the best candidate for further exploitation.

Method	LSAST*	MAPAS	DIAS*	FASF*
Accuracy	Centimeter level			
Time of Convergence		+		
Error Probability		+	+	
Nature and Model of Processed Measurements	Identical			
Functional Principle	Decision Primary Satellites required		Estimation No discrimination between satellites	
Nature and Quantity of Information extracted from observations	Optimal			
Computational Burden		-		
Relationship between performance and decision thresholds	N/A	Theoretical Link Exists	N/A	N/A
Quantification of error	Residuals			
Error Indicators	History of search set		History of tree exploration	

Table 8.10: *Summary of analysis of AROF procedures. The symbol * denotes the methods that were simply implemented by the LTST and SEXTANT AVIONIQUE from available publications. The symbol + means that the mentioned characteristic is an advantage of the method.*

Chapter 9

PERFORMANCE OF MAPAS ON DATA COLLECTED BY REAL RECEIVERS

The performance of AROF procedures was evaluated on real data in several configurations. A first set of measurements was collected using a Nortel GPS signal generator connected to the receivers, and a second set contains measurements in the field. All the data collected was not processed in real time, but post-processed.

On each set of data, the differences with the simulated measurements are analyzed, then the time of convergence and the error rate are assessed on the samples collected.

All the results are compared, and a conclusion is drawn from this analysis. These results are also available in [MB97].

9.1 Presentation of receivers used

The receivers used to perform the measurements are of two types:

- NOVATEL GPSCard. This is a 10-channel L1 GPS receiver that is connected to the computer via the ISA bus. The receiver is controlled from a software running under Microsoft Windows. Measurements can be delivered at a rate of 0.1 Hz to 20 Hz.
- SEXTANT AVIONIQUE TOPSTAR 200: 10-channel L1 GPS-receiver that is connected to the computer via an ARINC card. Measurements are delivered at a rate of 1 Hz.

In each case, the receivers were set up in a differential mode, either connected in real time via a serial line, or run in parallel with no physical data link at the time of recording the data.

9.2 Adaptation of software for application on real data

Several adaptations were made to the implementation of MAPAS for it to be able to raise properly the ambiguities. These adaptations were made progressively, as they were mostly driven by the difficulties encountered to process the data. The most important modifications concerned the synchronization of the reference and user data, the computation of the positions of the satellites for the user and for the reference separately and the introduction of a troposphere model.

9.2.1 Synchronization of user and reference data

The measurements made by the user and the reference receiver are triggered by a specific event within the receiver controlled by the CPU. This event occurs repeatedly with a period equal to the measurement frequency (< 20 Hz). The occurence of this event may be driven by any specific task, or may coincide with a particular clock event identical on all receivers of the same type. In the first case, measurements are taken by two receivers of the same type at two completely different times, in such a way that the difference between the times of measurements maybe as large as 0.5 s. In the other case, measurements of two receivers of the same type are taken almost simultaneously, the difference in time being identical to the offset between the two receiver clocks, which can amount to several μs.

In any case, the measurements are not made at the same time, and they need to be re-synchronized with each other for the single differences to be computed, as indicated in section 4.1.

We chose to extrapolate the measurements of the reference receiver at the times of the user receiver measurements. This is done for two reasons. First, it is best that there is the smallest time lag possible between the time the user receiver makes the measurements and the time a position is delivered. Thus, the measurements used for positioning should be the measurements computed at the time given by the user receiver. Second, the range observations made by the reference station have a slower and more stable evolution as this receiver is fixed on the ground.

9.2.2 Computation of the satellites position

In order to introduce as little distortion as possible, the positions of the satellites were specifically computed for the reference station and the user receiver. This computation is done using an iterative procedure that recursively estimates the duration of the propagation and the receiver clock offset, as the input of the satellite position computation algorithm is the ephemeris data and the time of transmission in the GPS time scale.

9.2.3 Compensation of tropospheric refraction

Before being fed to the MAPAS algorithm, the real measurements are compensated for tropospheric refraction. If this compensation is not done, the procedure fails to raise the ambiguities when the receivers are separated by more than 100 m. Several models were tested, and the most efficient one was found to be the NATO model, presented in appendix H.

9.3 Performance on data collected using Nortel simulator

The Nortel GPS signal simulator is an electronic device that generates GPS-like RF signals from computer models of the satellite constellation, of the signal models and of the receiver's dynamics. The Nortel simulator STR 2760 is owned by the STNA and was made available for the study reported here. This simulator is a differential test bench: it can simultaneously generate signals for a reference receiver and for a user receiver, as shown in figure 9.1.

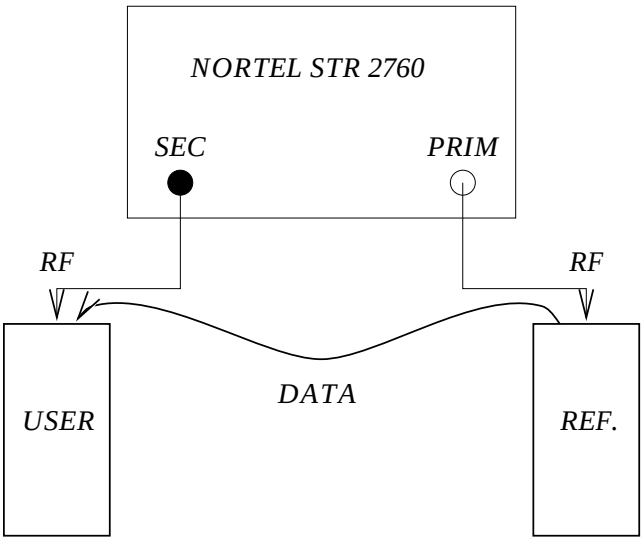

Figure 9.1: *Set-up of the Nortel connexions. The primary channel sends signals for the reference station. The secondary channels sends signals to the user receiver.*

9.3.1 Presentation of scenarios run

Several scenarios were run to evaluate the performance of MAPAS in several configurations. A first batch of scenarios simulates a static user at various points of the 3^o elevation approach path over Toulouse-Blagnac airport. These scenarios were designed to quantify the effect of the distance D and height h of the user receiver with respect to the reference station.

A summary of these scenarios is presented in table 9.1.

Type	#	Position	Multipath
Static	1	D = 1 m h = 0.5 m	No
Static	1 b	D = 500 m h = 25 m	No
Static	2	D = 5 km h = 260 m	No

Table 9.1: *Configuration of scenarios run on Nortel simulator.*

9.3.2 Quality of data

The data processed in this phase of the study is collected using the Nortel GPS signal generator. Therefore, all the distortions affecting the measurements are intentional. As a consequence, the noise superimposed to the signal can be controlled and the tracking accuracy is generally better than in real conditions. For example, no cycle slips were found in the data collected.

The carrier phase measurement noise was analyzed using the data collected in scenario 1 because there is negligible influence of spatial decorrelation of SA and atmospheric errors. The double differenced carrier phase measurement noise is computed as the difference between the observed double differenced measurements and the predicted double differenced carrier phase measurements. The double differenced carrier phase measurements can be predicted as the position of both receivers is accurately known, and the ambiguities can be easily determined using MAPAS for example.

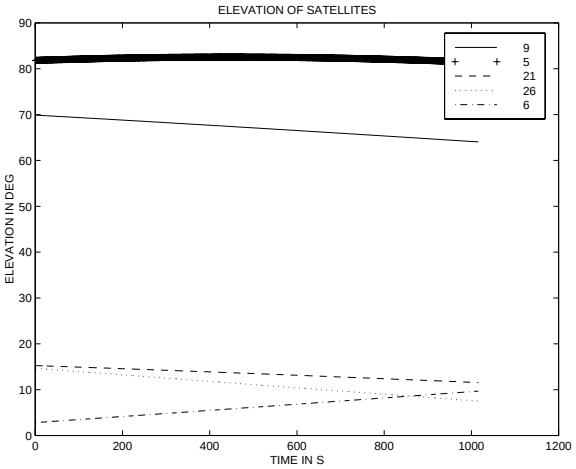

(a) *Elevation angles of four satellites*

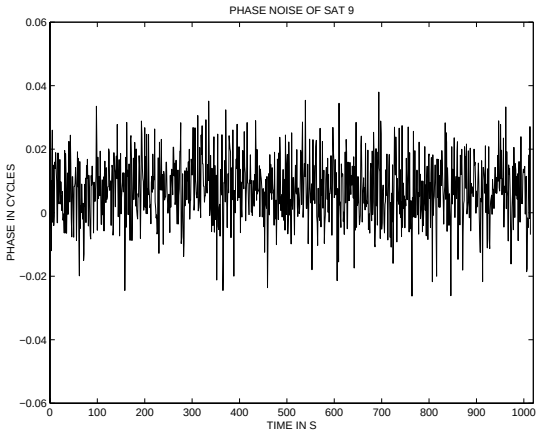

(b) *Phase noise of satellite 9*

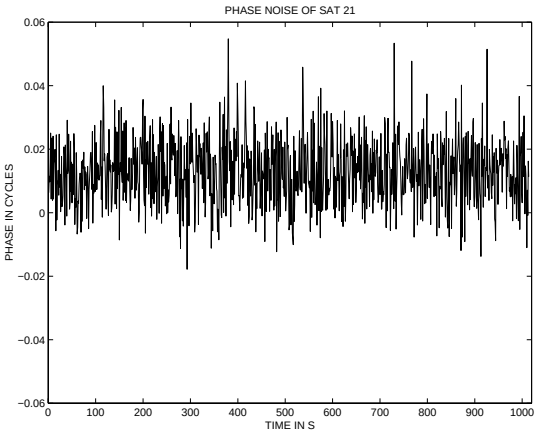

(c) *Phase noise of satellite 21*

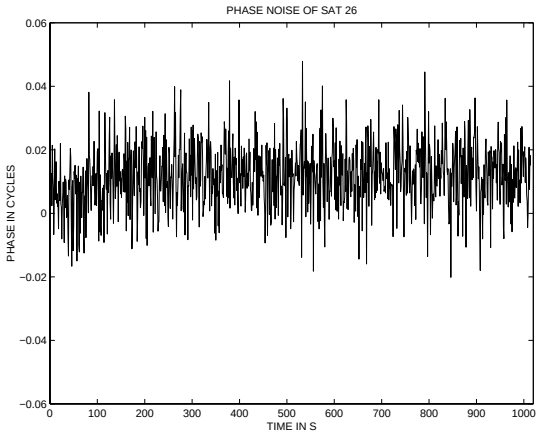

(d) *Phase noise of satellite 26*

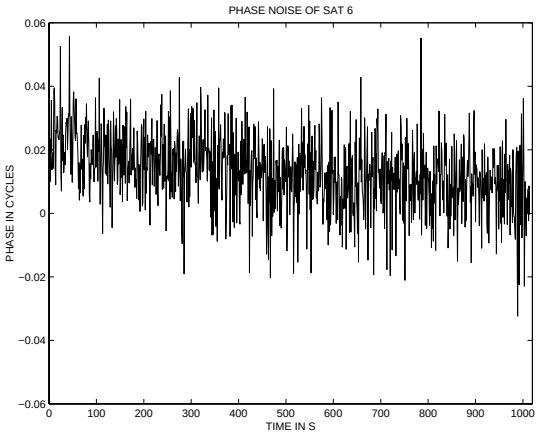

(e) *Phase noise of satellite 6*

Figure 9.2: *Double differenced phase noise observed on scenario 1 data.*

We can see in figures 9.2(b)-9.2(e) that all the phase noises exhibit a small bias. For satellite 6, which is a very low satellite, the offset value observed decreases as the elevation angle increases. This bias is due to the difference in atmospheric delays between the two receivers and to the low signal-to-noise ratio of the received signal.

Figures 9.3(a)-9.3(d) and 9.4(a)-9.4(d) show that the phase noise can be considered as white noise, with a Gaussian distribution.

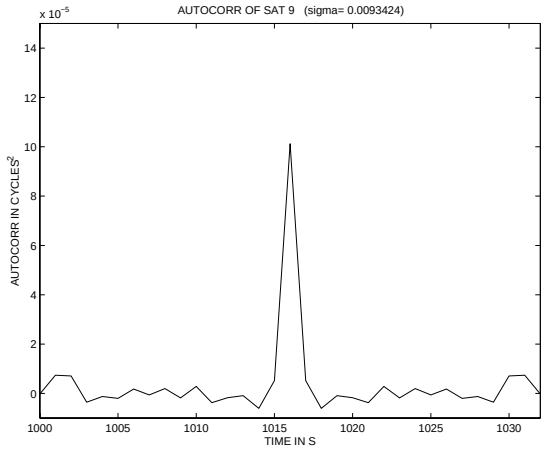

(a) *Zoom of autocovariance of double differenced phase noise of satellite 9*

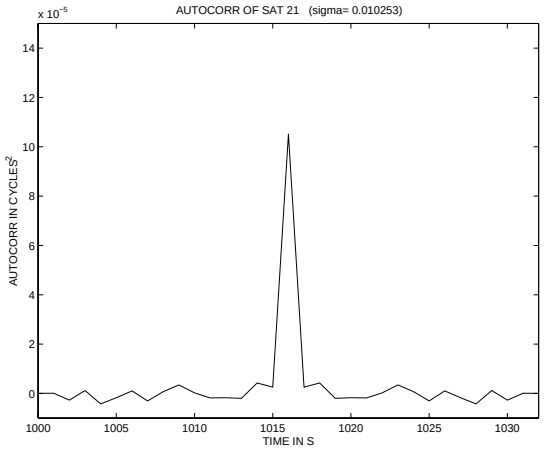

(b) *Zoom of autocovariance of double differenced phase noise of satellite 21*

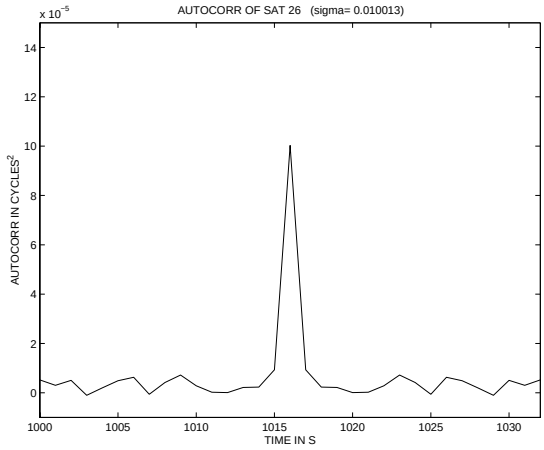

(c) *Zoom of autocovariance of double differenced phase noise of satellite 26*

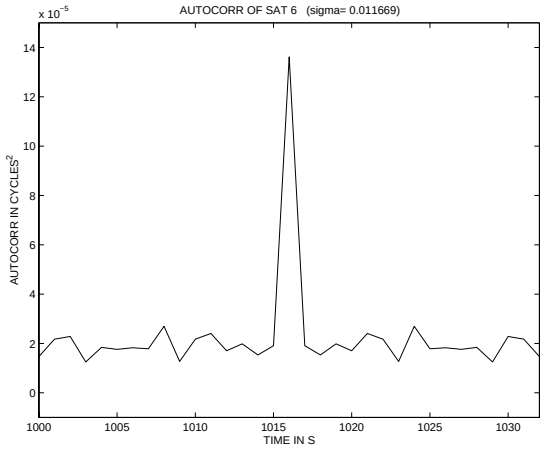

(d) *Zoom of autocovariance of double differenced phase noise of satellite 6*

Figure 9.3: *Autocovariance of double differenced code pseudorange noise observed on scenario 1 data.*

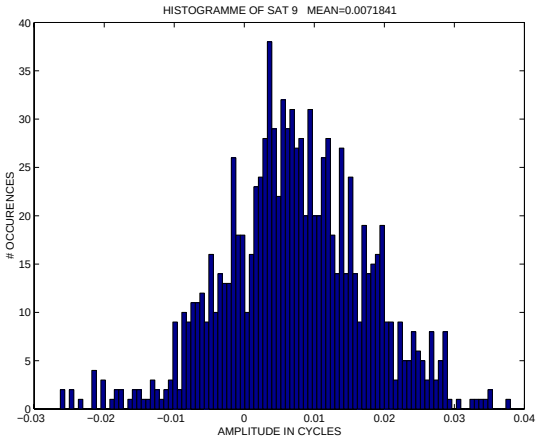

(a) *Histogram of double differneced phase noise of satellite 9*

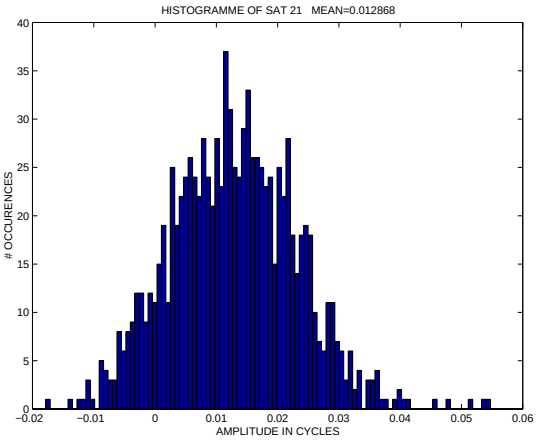

(b) *Histogram of double differenced phase noise of satellite 21*

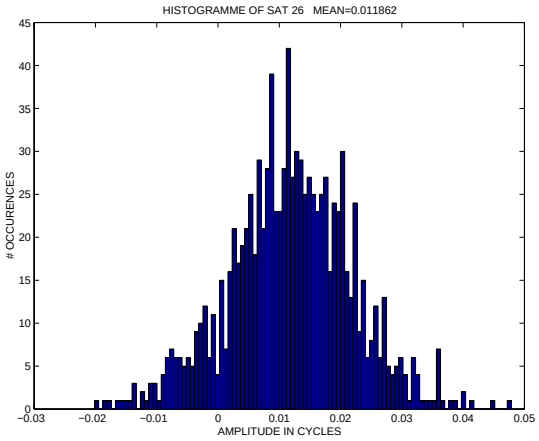

(c) *Histogram of double differenced phase noise of satellite 26*

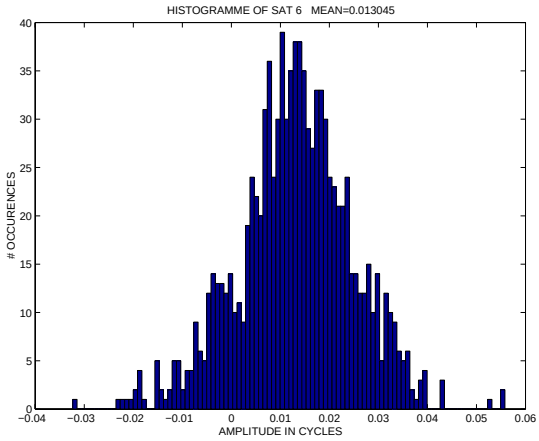

(d) *Histogram of double differenced phase noise of satellite 6*

Figure 9.4: *Histograms of double differenced code pseudorange noise observed on scenario 1 data.*

As a comparison, figures 9.5(a)-9.5(d) show the carrier phase smoothed double differenced code pseudorange noise for the same scenario. We see that the variance and the bias of this noise is larger than for the carrier phase. However, dividing the observed standard deviation of the double differenced code pseudorange noise by 2 to take into account the fact that these quantities are double differenced, we see that the noise on the undifferenced code pseudorange measurements is of the order of 7 cm, which is a very low value due as actual typical value of code pseudorange measurement noise is of the order of 1 m. This may be due to the extremely noiseless environment created by the Nortel simulator, and to the acrrier smoothing applied by the NOVATEL receiver.

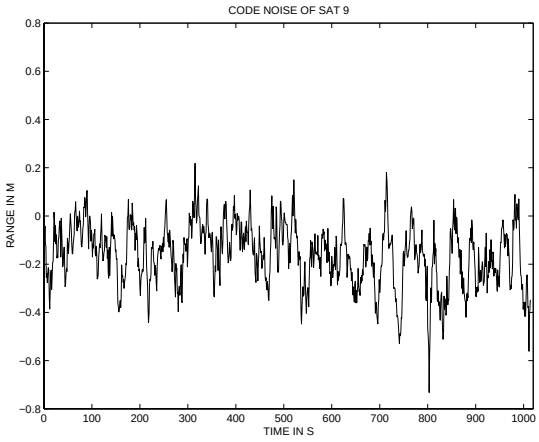

(a) *Code pseudorange noise of satellite 9 (mean = -0.16 m, std=0.13 m)*

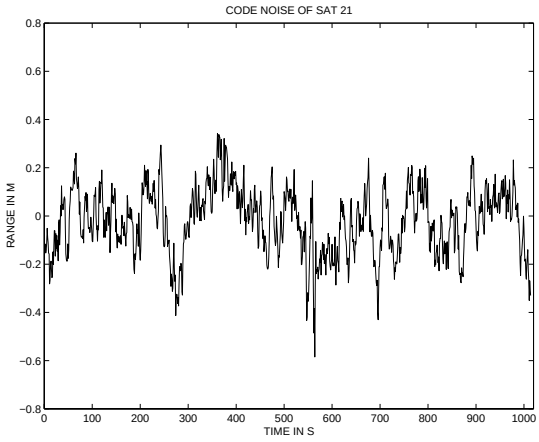

(b) *Code pseudorange noise of satellite 21 (mean = -0.02 m, std=0.14 m)*

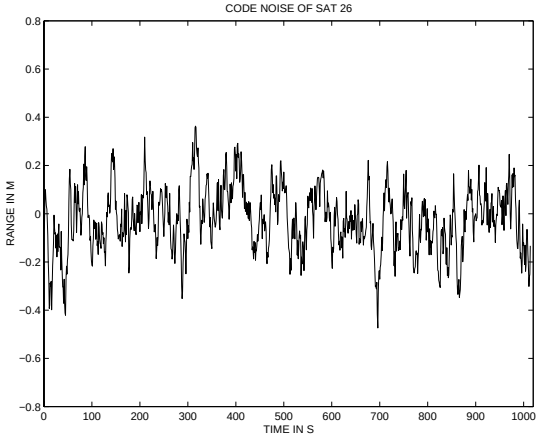

(c) *Code pseudorange noise of satellite 26 (mean = -0.02 m, std=0.13 m)*

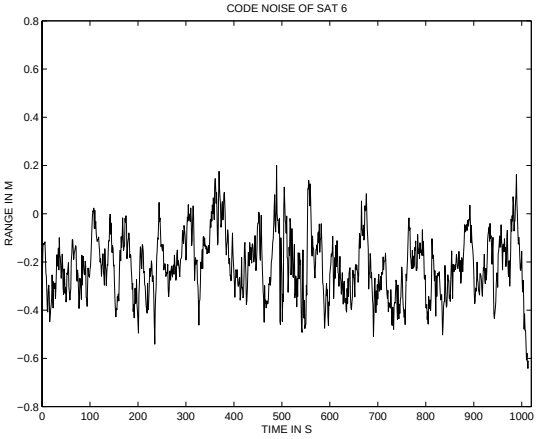

(d) *Code pseudorange noise of satellite 6 (mean = -0.21 m, std=0.13 m)*

Figure 9.5: *Double differenced code pseudorange noise observed on scenario 1 data.*

9.3.3 Results

This section presents the results of the execution of MAPAS on the different scenarios presented in section 9.3.1.

Results on static scenarios

The ambiguity resolution trials are launched one after the other every 15 s on each file. This is done in order to get significant statistics from the recorded file with the constraint that two consecutive trials should use as different data as possible.

	MAPAS 5 Hz (σ=0.02)	MAPAS 1 Hz (σ=0.02)	MAPAS 5 Hz (σ=0.01)
# trials N	44	14	109
# solved trials N_s	44	13	109
Percentage of successful trials $\frac{N_s}{N}$	100%	92.86%	100%
# solved and successful trials N_{ss}	44	13	109
Success rate $\frac{N_{ss}}{N}$	100%	92.86%	100%
Integrity $\frac{N_{ss}}{N_s}$	100%	100%	100%
Computation time (s)	mean: 4.17 std: 0.59 max: 7.81	mean: 3.78 std: 1.09 max: 4.30	mean: 3.76 std: 0.46 max: 8.05
Time of convergence (s)	mean: 26.26 std: 47.58 max: 323.40	mean: 59.55 std: 33.16 max: 125	mean: 10.53 std: 29.74 max: 308.2
# trials with duration > 205 s N_L	1(2.27%)	0(0%)	1(0.92%)
Unavailability of precise position $\frac{N_L+(N-N_s)}{N}$	2.27%	7.14%	0.92%
Vertical position error std in m (successful trials)	0.002 m	0.002 m	0.002 m
Vertical position error std in m (unsuccessful trials)	N/A	N/A	N/A

Table 9.2: *Results of the application of MAPAS to data of scenario 1 (GPS time 176500s to 177670s, week 767). Note that the unavailability of the precise position may be related to continuity risk (see discussion in section 6.2.3).*

Results on scenario 1 We can see in table 9.2 the influence of the data rate and of the prior variance.

The time of convergence is divided by 2 when going from 1 Hz samples to 5 Hz samples. The gain is not a 5:1 ratio, mainly because of failures of the communication link between the receiver and the computer that induces data lags, and also because the phase noise samples are slightly correlated due to atmospheric residuals.

The average time of convergence presented in this table does not reflect the observed values of this time: all the trials converge in a few tens of seconds, but one single trials in the middle of the file takes a very long time. Its time of convergence corresponds to the maximum time displayed in the table. This occurs because the number of visible satellites is 6 in the beginning of the trial. Otherwise, for all the other trials, the number of visible satellites is 7.

All the trials performed converged towards the good solution: the integrity is 100% in every case. The computation time is well under the time of convergence.

The position error is lower than 1 cm, which is as good as expected using carrier phase measurements.

	MAPAS 5 Hz (σ=0.02)	MAPAS 1 Hz (σ=0.02)	MAPAS 5 Hz (σ=0.01)
# trials N	78	78	78
# solved trials N_s	76	72	77
Percentage of successful trials $\frac{N_s}{N}$	97.44%	92.31%	98.72%
# solved and successful trials N_{ss}	76	72	77
Success rate $\frac{N_{ss}}{N}$	97.44%	92.31%	98.72 %
Integrity $\frac{N_{ss}}{N_s}$	100%	100%	100%
Computation time (s)	mean: 16.70 std: 9.19 max: 29.1	mean: 16.02 std: 9.88 max: 29.02	mean: 16.06 std: 9.45 max: 29.14
Time of convergence (s)	mean: 10.57 std: 14.74 max: 50.6	mean: 26.76 std: 28.24 max: 107	mean: 6.14 std: 9.25 max: 40.80
# trials with duration > 205 s N_L	0(0%)	0(0%)	0(0%)
Unavailability of precise position $\frac{N_L+(N-N_s)}{N}$	2.56%	7.69%	1.28%
Vertical position error std in m (successful trials)	0.002 m	0.002 m	0.002 m
Vertical position error std in m (unsuccessful trials)	N/A	N/A	N/A

Table 9.3: *Results of the application of MAPAS to data of scenario 1 b (GPS time 174870s to 176040s, week 767). Note that the unavailability of the precise position may be related to continuity risk (see discussion in section 6.2.3).*

Results on scenario 1 b Once again, we can see in table 9.3 the high influence of the data rate and of the prior variance.

The time of convergence is divided by 2.5 when going from 1 Hz samples to 5 Hz samples, which still is not a 5:1 ratio.

The unsolved trials are due to unexplained incorrect code measurements made by the receiver during 1.2 second at a particular point in the middle of the scenario, between 175106.4s and 175107.6 s included. These outliers cause the program to be unable to determine its differential position using code measurements. As these measurements are not deleted from the file, the longer the trials last, the more trials are affected. Therefore, we see that when the prior variance is set to a low value (σ=0.01 cycle) at a high data rate (5 Hz), the number of unsolved trials in the set is reduced to 1 as opposed to 6 in the worst case presented.

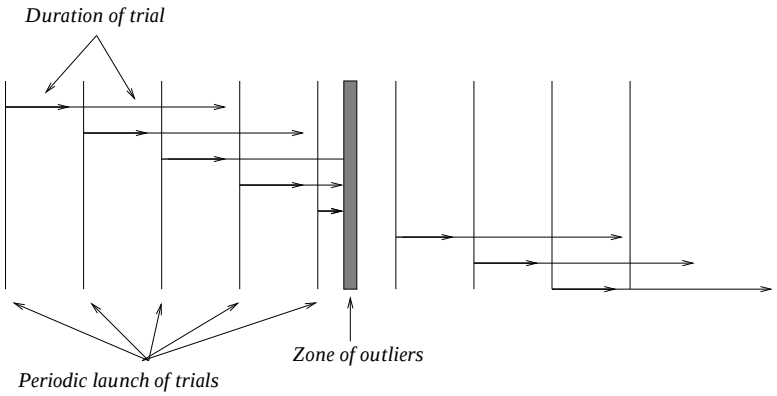

Figure 9.6: *Impact of the presence of outliers on the estimation of the performance of the procedure. The longer the trials last, the more trials get resetted.*

As a consequence, the unavailability of the precise position is highly influenced by the presence of this corrupted sequence in the file, going from 7.7 % in the worst case to 1.28 % in the best case.

The vertical positioning error obtained is lower than 1 cm in successful cases.

The number of satellites for this set ranges from 6 in the beginning to 9 at the end.

	MAPAS 5 Hz (σ=0.04)	MAPAS 5 Hz (σ=0.02)	MAPAS 5 Hz (σ=0.01)
# trials N	66	66	66
# solved trials N_s	57	57	57
Percentage of successful trials $\frac{N_s}{N}$	86.36%	86.36%	86.36%
# solved and successful trials N_{ss}	52	39	36
Success rate $\frac{N_{ss}}{N}$	78.79%	59.09%	54.55%
Integrity $\frac{N_{ss}}{N_s}$	91.23%	68.42%	63.16%
Computation time (s)	mean: 20.01 std: 12.11 max: 34.79	mean: 16.50 std: 10.36 max: 30.00	mean: 8.43 std: 5.39 max: 16.54
Time of convergence (s)	mean: 27.31 std: 18.24 max: 61.6	mean: 12.65 std: 10.73 max: 42.00	mean: 4.89 std: 4.35 max: 20.40
# trials with duration > 205 s N_L	0(0%)	0(0%)	0(0%)
Unavailability of precise position $\frac{N_L+(N-N_s)}{N}$	13.64%	13.64%	13.64%
Vertical position error std in m (successful trials)	0.002 m	0.002 m	0.002 m
Vertical position error std in m (unsuccessful trials)	0.653 m	1.0678 m	1.051 m

Table 9.4: *Results of the application of MAPAS to data of scenario 2 (GPS time 174746 s to 175748 s, week 767). Note that the unavailability of the precise position may be related to continuity risk (see discussion in section 6.2.3).*

Results on scenario 2 The time of convergence is divided by 2.5 when going from a prior variance σ=0.04 to σ=0.01 with 5 Hz samples. However, in the same time, the integrity drops from 90 % to 60 %. We see here that a trade-off must be done using the best value of σ.

The unsolved trials are due to unexplained incorrect code measurements made by the receiver during a total 1.2 second at a particular point in the beginning of the scenario, between 174876.6 s and 174877.8 s included. These outliers cause the program to be unable to determine its differential position using code measurements. As the trials are very slow in the beginning of the file because there are only 5 satellites visible, all of them get resetted whenever they reach that point, as illustrated in figure 9.7.

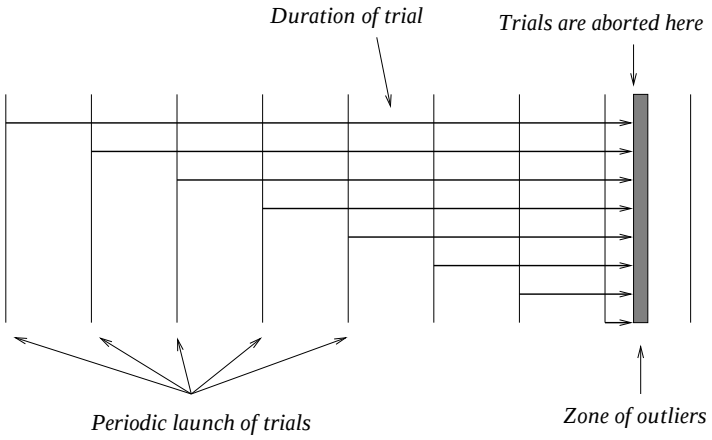

Figure 9.7: *Impact of the presence of outliers on the estiation of the performance of the procedure. If the trials are very long in any case, a large number of unsolved cases are observed.*

All the 9 first trials are aborted due to this problem. As a consequence, the unavailability of the precise position is highly influenced by the presence of this corrupted sequence in the file, leading to an unavailability of 13.6 %.

If this corrupted segment had been removed, the availability would have been significantly increased. This problem is attributed to a problem in the processing software that should be corrected in the next future.

The vertical positioning error obtained is lower than 1 cm in successful cases. However, when the procedures makes errors, the vertical position error reaches 1 m in the worst case observed.

The number of satellites for this set ranges from 5 to 8.

9.4 Performance on field measurements

Field measurements used for this analysis were conducted in August and September 1996 at the Toulouse-Blagnac airport, and in February 1997, at the Paris Charles De Gaulle airport using Novatel GPSCard receivers. The processed data are 4 static sets and 1 dynamic set. 2 of the 4 static sets were done using 3 receivers, providing 3 baselines each. Therefore, the total number of different possible static sets is 8. The dynamic measurements were collected using a car driven around the Toulouse-Blagnac airport. The reference position for the dynamic set is the position determined using the GeoTracer software, developed by GEOTRONICS.

A description of the data sets is presented in table 9.5.

Type	Name	Trajectory
Static	CDG1	Static, 29 m
Static	CDG2	Static, 29 m
Static	TLS3-1	Static, 898 m
Static	TLS3-2	Static, 132 m
Static	TLS4-1	Static, 898 m
Dynamic	TLS5-3	Dynamic with car

Table 9.5: *Description of real data sets.*

9.4.1 Quality of data

The data used in this phase of the study was collected in the field in real situations. Therefore, many distortions were observed on the recorded measurements. For example, a very large number of cycle slips is found in many of the files, and it was sometimes difficult to isolate an interval with no cycle slip. However, as we do not have an automatic program for cycle slip correction, these defaults were not removed from the recorded files.

9.4.2 Results on static measurements

Data set CDG1

	MAPAS 1 Hz (σ=0.1)	MAPAS 1 Hz (σ=0.07)	MAPAS 1 Hz (σ=0.05)
# trials N	330	332	334
# solved trials N_s	243	263	286
Percentage of successful trials $\frac{N_s}{N}$	73.64%	79.22%	85.63%
# solved and successful trials N_{ss}	195	201	223
Success rate $\frac{N_{ss}}{N}$	59.01%	60.54%	66.77%
Integrity $\frac{N_{ss}}{N_s}$	80.25%	76.43%	77.97%
Computation time (s)	mean: 29.48 std: 17.99 max: 48.72	mean: 21.85 std: 11.54 max: 35.47	mean: 18.15 std: 7.80 max: 28.46
Time of convergence (s)	mean: 160.70 std: 93.12 max: 497	mean: 121.04 std: 69.59 max: 327	mean: 91.02 std: 53.73 max: 227
# trials with duration > 205 s N_L	43(13.03%)	26(7.83%)	7(2.10%)
Unavailability of precise position $\frac{N_L+(N-N_s)}{N}$	33.39%	28.61%	16.47%
Vertical position error std in m (successful trials)	0.005 m	0.007 m	0.005 m
Vertical position error std in m (unsuccessful trials)	2.216 m	1.951 m	2.258 m

Table 9.6: *Results of the application of MAPAS to data set CDG1 (GPS time 391010 s to 396070 s, week 893). Note that the unavailability of the precise position may be related to continuity risk (see discussion in section 6.2.3).*

As we can see in table 9.6, the integrity has dropped with respect to the results presented in section 9.3.3. The integrity remains around 80 %, and a large increase of the availability of the precise position is observed when decreasing the prior variance of the noise.

The position error in the successful cases is larger than with the Nortel data, but still remains under 1 cm. Similarly, the position error induced by wrong ambiguities is around 2 m, which is twice as much as observed on Nortel data.

The number of visible satellites in this set ranges from 7 to 9, with a large majority to 8.

Data set CDG2

	MAPAS 1 Hz (σ=0.1)	MAPAS 1 Hz (σ=0.07)	MAPAS 1 Hz (σ=0.05)
# trials N	220	220	220
# solved trials N_s	110	131	154
Percentage of successful trials $\frac{N_s}{N}$	50%	59.55%	70%
# solved and successful trials N_{ss}	55	69	92
Success rate $\frac{N_{ss}}{N}$	25.00%	31.36%	41.82%
Integrity $\frac{N_{ss}}{N_s}$	50.00%	52.67%	59.74%
Computation time (s)	mean: 16.47 std: 17.36 max: 52.92	mean: 13.94 std: 12.33 max: 37.79	mean: 12.37 std: 8.92 max: 27.36
Time of convergence (s)	mean: 141.39 std: 81.89 max: 278	mean: 109.73 std: 65.86 max: 240	mean: 84.71 std: 52.52 max: 212
# trials with duration > 205 s N_L	18(8.18%)	6(2.73%)	2(0.91%)
Unavailability of precise position $\frac{N_L+(N-N_s)}{N}$	58.18%	43.18%	30.91%
Vertical position error std in m (successful trials)	0.011 m	0.013 m	0.012 m
Vertical position error std in m (unsuccessful trials)	0.822 m	1.160 m	1.598 m

Table 9.7: *Results of the application of MAPAS to data set CDG2 (GPS time 460060 s to 463452 s, week 893). Note that the unavailability of the precise position may be related to continuity risk (see discussion in section 6.2.3).*

The integrity observed after the execution of these trials is lower than the integrity estimated on data set CDG1. Similarly, the availability of the precise position is lower, which is certainly due to the lower number of visible satellites, ranging from 6 to 8, with a majority of 7.

Data set TLS3-1

	MAPAS 1 Hz (σ=0.1)	MAPAS 1 Hz (σ=0.07)	MAPAS 5 Hz (σ=0.01)
# trials N	240	249	251
# solved trials N_s	240	249	251
Percentage of successful trials $\frac{N_s}{N}$	100%	100%	100%
# solved and successful trials N_{ss}	23	23	22
Success rate $\frac{N_{ss}}{N}$	9.58%	9.24%	8.76%
Integrity $\frac{N_{ss}}{N_s}$	9.58%	9.24%	8.76%
Computation time (s)	mean: 19.85 std: 2.61 max: 25.08	mean: 25.21 std: 2.81 max: 32.01	mean: 18.17 std: 2.03 max: 23.19
Time of convergence (s)	mean: 291.75 std: 63.48 max: 499	mean: 244.41 std: 60.50 max: 496	mean: 193.50 std: 66.33 max: 415
# trials with duration > 205 s N_L	227(94.58%)	185(74.30%)	100(39.84%)
Unavailability of precise position $\frac{N_L+(N-N_s)}{N}$	94.58%	74.30%	39.84%
Vertical position error std in m (successful trials)	0.011 m	0.013 m	0.012 m
Vertical position error std in m (unsuccessful trials)	1.781 m	1.666 m	1.515 m

Table 9.8: *Results of the application of MAPAS to data set TLS3-1 (GPS time 305330 s to 309290 s, week 868).*

The integrity observed on the trials run on this data set is extremely low (lower than 10 %), and the availability of the precise position is rigorously unacceptable. This may be due to the low number of satellites visible during this experiment, ranging from 5 to 7.

Data set TLS3-2

	MAPAS 1 Hz (σ=0.1)	MAPAS 1 Hz (σ=0.07)	MAPAS 1 Hz (σ=0.01)
# trials N	297	297	303
# solved trials N_s	283	287	295
Percentage of successful trials $\frac{N_s}{N}$	95.29%	96.63%	97.36%
# solved and successful trials N_{ss}	108	89	67
Success rate $\frac{N_{ss}}{N}$	36.36%	29.97%	22.11%
Integrity $\frac{N_{ss}}{N_s}$	38.16%	31.01%	22.71%
Computation time (s)	mean: 21.70 std: 5.75 max: 30.07	mean: 27.90 std: 6.49 max: 38.63	mean: 20.43 std: 4.49 max: 28.74
Time of convergence (s)	mean: 281.01 std: 77.73 max: 537	mean: 232.74 std: 63.34 max: 392	mean: 188.76 std: 61.15 max: 343
# trials with duration > 205 s N_L	277(93.27%)	199(67%)	119(39.27%)
Unavailability of precise position $\frac{N_L+(N-N_s)}{N}$	97.98%	70.37%	41.91%
Vertical position error std in m (successful trials)	0.008 m	0.007 m	0.007 m
Vertical position error std in m (unsuccessful trials)	1.724 m	1.654 m	1.634 m

Table 9.9: *Results of the application of MAPAS to data set TLS3-2 (GPS time 305066 s to 309880 s, week 893). Note that the unavailability of the precise position may be related to continuity risk (see discussion in section 6.2.3).*

The integrity of the solution is larger than on data set TLS3-1, but it remains very low. The availability of the precise position is still unacceptable. The number of satellites in this set ranges from 6 to 7.

Data set TLS4-1

	MAPAS 1 Hz (σ=0.1)	MAPAS 1 Hz (σ=0.07)	MAPAS 1 Hz (σ=0.01)	MAPAS 1 Hz (σ=0.1) w/o tropo correction
# trials N	239	239	240	239
# solved trials N_s	232	231	237	229
Percentage of successful trials $\frac{N_s}{N}$	97.07%	96.65%	98.75%	95.82%
# solved and successful trials N_{ss}	29	30	27	0
Success rate $\frac{N_{ss}}{N}$	12.13%	12.55%	11.25%	0%
Integrity $\frac{N_{ss}}{N_s}$	12.50%	12.99%	11.39%	0%
Computation time (s)	mean: 50.22 std: 9.72 max: 62.85	mean: 34.06 std: 7.07 max: 43.98	mean: 25.06 std: 3.88 max: 31.70	mean: 27.70 std: 6.21 max: 33.83
Time of convergence (s)	mean: 280.39 std: 72.61 max: 449	mean: 229.29 std: 68.81 max: 425	mean: 181.88 std: 59.18 max: 307	mean: 280.03 std: 83 max: 551
# trials with duration > 205 s N_L	209(87.45%)	155(64.85%)	82(34.17%)	210(87.87%)
Unavailability of precise position $\frac{N_L+(N-N_s)}{N}$	90.38%	68.20%	35.42%	92.05 %
Vertical position error std in m (successful trials)	0.008 m	0.007 m	0.007 m	N/A
Vertical position error std in m (unsuccessful trials)	0.577 m	0.670 m	0.701 m	0.561

Table 9.10: *Results of the application of MAPAS to data set TLS4-1 (GPS time 298620 s to 302339 s, week 869). Note that the unavailability of the precise position may be related to continuity risk (see discussion in section 6.2.3).*

As we can see in this table, the integrity is very low (around 10 %). This may due to the same problem encountered with data set TLS3-1, as the distance between is the two receivers is identical. The number of satellites for this set is 6 in the beginning and 7 during the remaining two thirds of the file.

9.4.3 Results in dynamic application

Data set TLS5-3

A car carrying a GPS receiver is driven around the runway of the Toulouse-Blagnac airport, as shown in figure 9.8(a). MAPAS is run on the data set, and a position is issued by the procedure after resolution of the ambiguities. The prior standard devition is set to 0.5 cycle, as this value seemed to provide

good results on the static data sets presented in section 9.4.2. The reference position is computed from the GPSCard measurements using the GEOTRACER 2.24 software, developed by GEOTRONICS. A number of verification of known baselines have been carried out before using this software as a reference.

The ambiguities are properly raised at the very beginning in 158 s, and the procedure is able to keep track of the movement of the vehicle during the whole file. The standard deviation of the 3D position error is 4mm. The figures 9.8(b), 9.8(c) and 9.8(d) show the error of the position error over time. As we can see, all of them exhibit a peak rising up to a few centimeters during a small interval. During this interval, the car is stopped on a service road, and the position estimate is affected by small unexplained variations, that may be attributed to multipath.

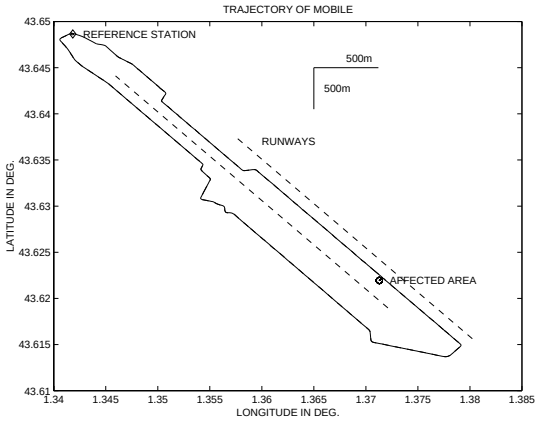

(a) *Trajectory of mobile: the car is driven around the runway.*

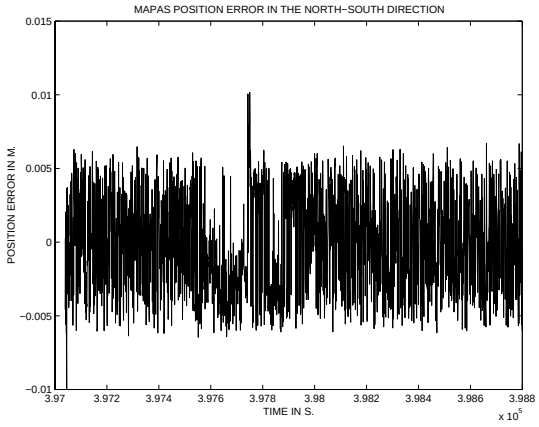

(b) *Position error of MAPAS in the North-South direction (with respect to GEOTRACER solution).*

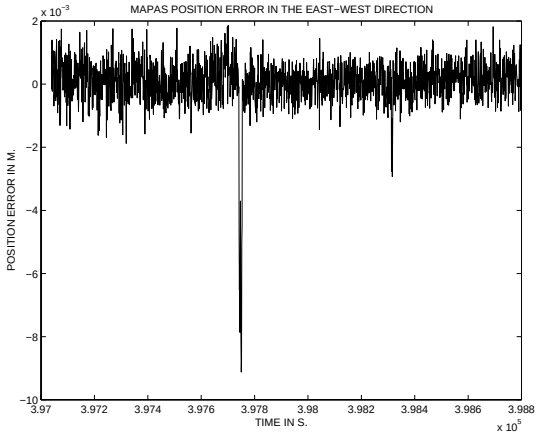

(c) *Position error of MAPAS in the East-West direction (with respect to GEOTRACER solution).*

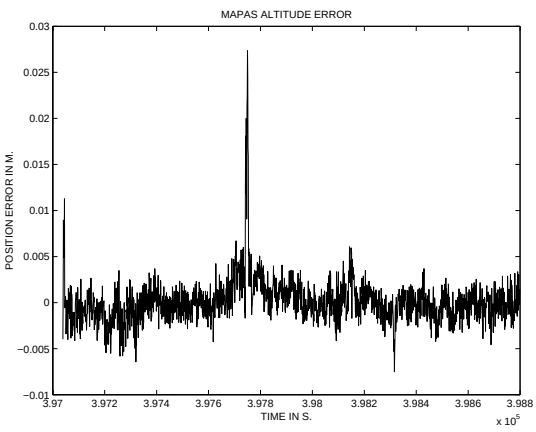

(d) *Altitude error of MAPAS (with respect to GEOTRACER solution).*

Figure 9.8: *Results of the application of MAPAS to real measurements collected in a dynamic situation.*

9.5 Conclusion

A preliminary conclusion can be drawn about the initial results of the exploitation of MAPAS presented in this chapter.

First, we see that several modifications to the pre-processing module, such as data synchronization, distinction between user and receiver satellite computation, and tropospheric compensation, had to be made in order to be able to raise properly the ambiguities on these first data.

Then, we can see that the data collected on the NORTEL simulator are very clean, and may not fully represent reality. However, several problems were identified in this phase of the study, and some of them are still to be solved to process successfully measurements for a distant receiver (> 5 km). The prior variance appears as a factor driving the time of convergence and the estimated integrity and unavailability of the precise position. A very significant improvement of the performance of the procedure is observed when measurements are delivered at 5 Hz in comparison with the 1 Hz case. So far, the integrity values obtained are between 60 % and 100%, the time of convergence ranges between 6 s and 30 s, and the unavailability of the precise position is between 3% and 13 %. However, due to our lack of experience in processing real measurements, these figures can only be interpreted as initial estimates. Moreover, because the number of measurements exploited is very low, and the size of the confidence interval is unknown, a small confidence is attributed to the estimates. As a rule of thumb, we can assume that estimates of performance parameters is only valid at the first digit at the most, because the number of trials never reaches 1000.

Finally, the data collected in the field show the extreme difficulty to process properly carrier phase measurements. Numerous cycle slips and outliers are encountered in the files, calling for a very efficient quality control module, which is not ready yet. The prior variance of the phase noise had to be raised by a factor of 5 from 0.01 cycle on NORTEL scenarios to 0.05 cycle in order to obtain as many successful resolutions as possible. The estimated integrity is low (< 81 %) when the two receivers are close (29 m), and is extremely low (< 39 %) when the receivers are seperated by 900 m. The time of convergence is larger than 3 min in average, which is very close to the limit chosen in this study. Finally, the unavailability of the precise position is very high as it reaches 98 %, due to the large number of unsolved trials. However, a further investigation of this problem should lead to an improvement of this number.

Chapter 10

CONCLUSION

During this work, a number of research activities have been carried out to draw a preliminary conclusion on the operational adequacy of AROF procedures for precision landings.

The impact of the raw data processing techniques, such as single differencing and data synchronization on the data fed to the procedure has been systematically assessed.

A classification of AROF procedures has been established, based on the approach chosen for resolution of the ambiguities, leading to a distinction between decision and estimation techniques. LSAST and MAPAS were studied as examples of the first category, whereas DIAS and FASF were analyzed to illustrate the second one.

A new AROF procedure based on a maximum a posteriori sequential test has been developed and implemented. It is characterized by a smooth rejection mechanism and delivers at each step of the resolution a criterion quantifying the confidence to be placed in each solution.

The theoretical performance parameters of MAPAS have been established using the MSPRT formulation. This analysis enabled us to determine theoretical expressions of bounds and asymptotic values of error probability and time of convergence. These expressions allow a control over the performance of MAPAS, and have been checked against the observed performance parameters.

An optimal set of evaluation criteria has been identified for the comparison of the AROF procedures and the assessment of their adequacy to fulfill the operational requirements. The first two sets are the performance parameters and the working assumptions, indicating the error probability, the time of convergence and the mathematical model of the measurements processed. The other two sets are the processing method and the means of control, that indicate the method used, its computational burden, and the means provided to control and monitor the procedure. Constraints on each of the identified characteristics have been derived from the civil aviation required navigation performance.

At the end of this work, the characteristics of four AROF procedures, namely LSAST, MAPAS, DIAS and FASF were compared with each other. The evaluation was done on simulated data in various configurations, on data collected from a GPS signal generator and on field measurements in various environment conditions.

According to the simulations run, it appears that the performance of the AROF procedures is severely reduced in presence of multipath and that pseudolites do not contribute sufficiently to the improvement of their capacity when their ranging noise is equivalent to the satellite ranging noise. However, MAPAS appears as the most robust procedure in presence of distortions. We must note that the computation burden of our development software is fairly high, but more work is currently being carried out by SEXTANT AVIONIQUE to improve its real-time capabilities.

MAPAS emerged as the most promising method. Nonetheless, it must be stressed that the algorithms of LSAST, DIAS and FASF were not implemented by their initial developers. Therefore, the obtained performance may not be the optimal performance. Moreover, the floating point ambiguity es-

timation procedures have not been fully analyzed, and a final conclusion is pending for further results.

From an operational point of view, the characteristics of MAPAS are far from satisfactory. Although the accuracy performance is outstanding when the ambiguities are correctly raised, the positioning error is well out of performance when the algorithm elects a wrong set of ambiguities. Unfortunately, this situation occurs too often with regards to the requirements and the procedure does not provide a means to detect it. The integrity is thus insufficient for CAT II/III precision landings. Similarly, the continuity risk is much too high. Indeed, the time of convergence can be longer than the alloted slot in some particular satellite configurations, and the sensitivity to cycle slips is detrimental to this key performance. As the availability requirement of AROF procedures has not been clearly defined yet, this parameter has not been further analyzed.

Nevertheless, several limitations restrict the range of these conclusions. Although the models used for simulations have been selected as close to reality as possible, complex phenomena appearing in real situations cannot be properly reproduced. The amount of real measurements is limited due to the difficulty of organization and the time-consuming nature of data collection campaigns on airport grounds. This also led to a limited number of receiver and environmental configurations that restricts the range of this evaluation. Finally, the algorithms were not tested in real-time in a real landing situation.

To refine the assessment, broader scale experiments should be carried out encompassing a large number of satellite configurations, signal distortions like multipath, interference, atmospheric perturbations, user/reference station geometry and aircraft dynamics. Such a test campaign has been scheduled by SEXTANT AVIONIQUE in the next phase of the study.

To remedy the current limitations of MAPAS, a number of improvements have been foreseen. The noise model could be refined to account for time-correlated errors. An integrity module could be developed using either internal measurement redundancy or external aids to monitor the accuracy of the proposed solution. In addition, a module monitoring the quality of the measurements must be developed, checking for cycle slips and outliers. Finally, the algorithm of MAPAS must be optimized to improve its real-time performance.

These improvements should lead to a better understanding of the capabilities and limitations of these procedures. These methods are currently assessed at international level in ICAO working groups. Once completed, this analysis will provide theoretical and practical results usable by these groups for the choice of a CAT II/III landing system. Should AROF procedures be selected, the results of this study could further be used to develop the appropriate standards.

Looking still further ahead, the evaluation methodology developed during this study could easily be extended to encompass the assessment of new systems. It is also expected that MAPAS could be adapted to accomodate new types of measurements provided by a GNSS2 system. In this context, we can hope that the level of performance will be highly improved since carrier phase processing would have been a design driver to fulfill CAT II/III operational requirements.

Appendix A

ICAO's definition of categories of approaches

Categories of aircraft approaches are defined by ICAO in [ICA96] according in particular to the level of confidence that can be placed by the pilot into the system he is using to help him land the plane safely. The precision approach is divided in two main segments : the aircraft first follows the indication provided by the landing system, then the pilot takes over in the final part and controls the aircraft using visual outside information if the aircraft is in a position to land. As the reliability of the aircraft, of the crew and of the landing system increases, the height of the aircraft over the ground at the end of the interval of use of the information provided by the system can be decreased.

Therefore, a critical point in the approach path, called the *Decision Height (DH)* is specified, which is the minimum height above the runway threshold at which a missed approach procedure must be executed if the minimal visual reference is not established. Otherwise, the aircraft is flown manually by the pilot using visual external reference or automatically by the autopilot under pilot monitoring. The visual requirements are expressed in terms of *distance of visibility* and *Runway Visual Range (RVR)*. The visibility is the greatest distance, determined by atmospheric conditions and expressed in units of length, at which it is possible with the unaided eye to see and identify, in daylight, a prominent dark object, and at night a remarkable light source [ICA85]. The RVR is the maximum distance in the landing direction at which the pilot on the centerline can see the runway surface markings or the runway lights, as measured at different points along the runway and in particular in the touchdown area [ICA92]).

Values of DH, visibility and RVR for CAT I, II and III approaches are presented in table A.1 and illustrated in figure A.1.

Category		Decision Height (DH)	Visual Requirements
CAT I		DH $\geq$ 60 m (200 ft)	Visibility $\geq$ 800 m or RVR $\geq$ 550 m
CAT II		(100 ft) 30 m $\leq$ DH $<$ 60 m	RVR $\geq$ 350 m
CAT III	A	0 m $\leq$ DH $<$ 30 m	RVR $\geq$ 200 m
	B	0 m $\leq$ DH $<$ 15 m (50 ft)	50 m $\leq$ RVR $<$ 200 m
	C	DH=0 m	RVR = 0 m

Table A.1: *ICAO's Definition of categories of approaches as stated in (ICAO,1996) Attachment C, page 98.*

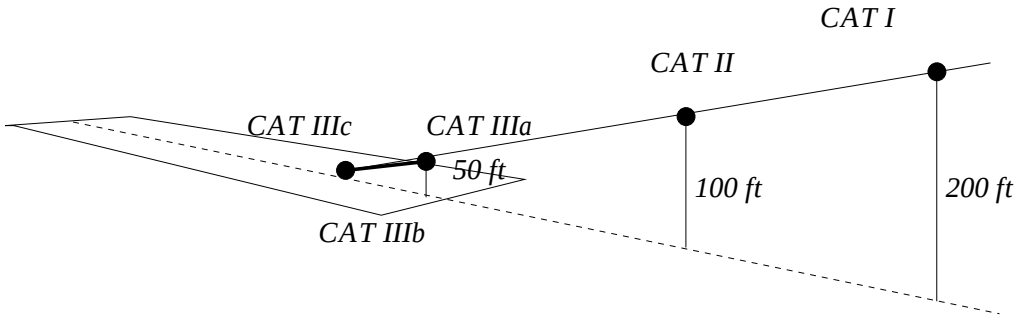

Figure A.1: *Definition of categories of approaches.*

Appendix B

ILS and MLS requirements

The *Instrument Landing System (ILS)* is the most widely used electronic guidance system for precision approaches. It is based on old principles, as early design of the ILS was conducted in 1919 [ESM+95]. Beginning in 1967 until 1994, the *Microwave Landing System (MLS)* was the leading contender for replacement of ILS. However, in 1994, the Federal Aviation Administration (FAA) stopped the MLS development in favor of satellite based landing schemes, and the ICAO decided in 1995 that ILS should be kept as the basic landing system, and that MLS could be installed when proved necessary.

An ILS ground system is composed of three radiating subsystems:

- The *localizer (LOC)* provides lateral guidance information with respect to the centerline. The information is provided by Amplitude Modulation (AM) of the RF carrier at 90 Hz and 150 Hz. The modulation depth of the two tones is equal on the extended centerline. To the left of centerline, from the viewpoint of an approaching aircraft, the 90 Hz predominates. The *difference in the depth of modulation (DDM)* vary linearly with the deviation angle in a $\pm 3^o$ to $\pm 4^o$ region about the centerline. Forty operating channels are provided, spaced 50 kHz apart from 108.10 MHz to 111.95 MHz.

- The *glideslope (GLIDE)* provides vertical guidance information with respect to the nominal glide path. The signal radiated is identical to the LOC signal, except that the 150 Hz predominates below the glide path, and the 90 Hz predominates above. Forty channels are available, spaced 150 kHz apart from 329.15 MHz to 335.0 MHz.

- Two or three *marker beacons* provide spot checks of position at 4.5 Nm (*outer marker*), at the 200 ft CAT I decision height (*middle marker*), and at the 100 ft CAT II decision height (*inner marker*). The markers operate at the VHF frequency of 75 MHz. These markers tend to be replaced by Distance Measuring Equipments (DME), that provide continuous range information.

An ILS system is presented in figure B.1.

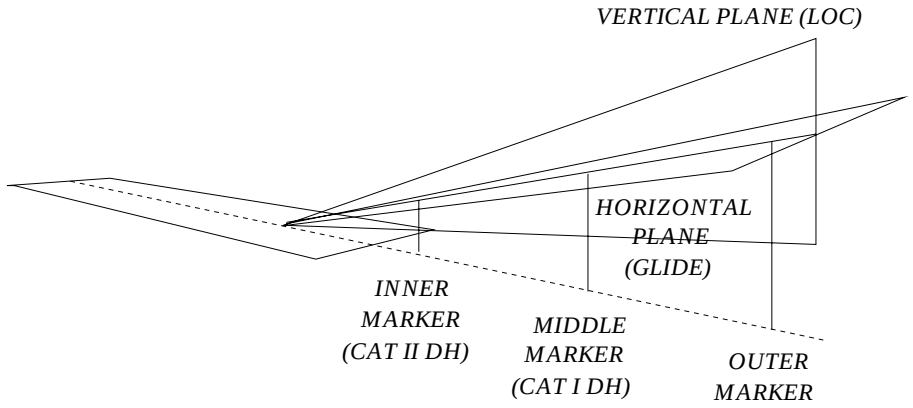

Figure B.1: *Illustration of GLIDE and LOC guiding planes.*

An MLS ground system is also composed of three separate sub-systems:

- The *azimuth (AZ)* ground station provides lateral information with respect to boresight of the antenna. This information is provided by a narrow vertical *scanning beam* radiated by the antenna that sweeps horizontally on each side of boresight with a constant angular rate. The interval between the reception of two pulses is proportional to the angle offset with respect to boresight. Coverage of the AZ station extends to $\pm 40^o$ on each side of boresight.
- The *elevation (EL)* ground station provides vertical information with respect to the nominal glide path. The principle is the same as for the AZ station. Coverage of the EL station is provided from 0.9^o to 15^o.
- The *Distance Measuring Equipment (DME)* provides continuous range information.

The complete MLS equipment enables the determination of the position of the aircraft.

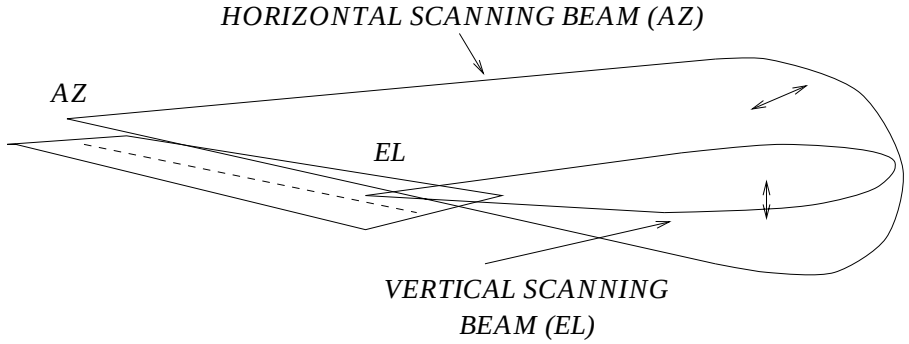

Figure B.2: *Illustration of AZ and EL scanning beams.*

Requirements for an ILS and an MLS ground station depends on the category of operation of the runway. These requirements are presented in [ICA96] and are recalled in table B.1.

Category	Integrity during any landing	Continuity of service	Mean Time Between Outages (MTBO)
CAT I	$1\text{-}10^{-7}$	$1\text{-}4{\cdot}10^{-6}$ in any 15 s period	1000 hr
CAT II	$1\text{-}0.5{\cdot}10^{-9}$	$1\text{-}2{\cdot}10^{-6}$ in any 15 s period	2000 hr
CAT III	$1\text{-}0.5{\cdot}10^{-9}$	$1\text{-}2{\cdot}10^{-6}$ in any 30 s period (LOC) $1\text{-}2{\cdot}10^{-6}$ in any 15 s period (GLIDE)	4000hr LOC 2000hr GLIDE

Table B.1: *ICAO's ILS and MLS reliability requirements found in (ICAO, 1996), attachment C to part 1.*

The accuracy requirements for an ILS ground station are presented in [ICA96] and recalled in table B.2 and table B.3 for the Localizer (LOC), and in table B.4 and table B.5 for the glideslope (GLIDE).

Category	LOC bias error limit at runway threshold [ICA96]
CAT I	10.5 m
CAT II	4.5 m
CAT III	3 m

Table B.2: *Maximum specified LOC alignment error at runway threshold from [ICA96], section 3.1.3.6.1.*

Category and validity area (point B = point located at 1050 m from runway threshold)	LOC beam bend error limit in Difference in Depth of Modulation (DDM) (2σ)
CAT I between point B and 100ft point	0.015
CAT II between point B and reference point	0.005
CAT III between point B and reference point	0.005

Table B.3: *Maximum LOC beam bending from [ICA96], section 3.1.3.4.1.*

Category	GLIDE angle error limit (θ is the nominal glide path angle)
CAT I	0.075θ
CAT II	0.075θ
CAT III	0.04θ

Table B.4: *Maximum GLIDE angle error from [ICA96], section 3.1.5.1.2.2.*

Category	GLIDE beam bend error limit in DDM
CAT I	0.035
CAT II	0.023
CAT III	0.023

Table B.5: *GLIDE beam bend error limit in DDM from [ICA96], section 3.1.5.4. Note that the specified angular displacement sensitivity is 0.0875 DDM for 0.12θ.*

The accuracy of an MLS ground station is presented in [ICA96] and is recalled in table B.6.

Station	Path Following Error (PFE) (2σ)	Path Following Noise (PFN) (2σ)	Control Motion Noise (CMN) (2σ)
AZ	6 m	3.5 m	3.2 m
EL	0.6 m	0.4 m	0.3 m

Table B.6: *MLS accuracy requirements.*

Appendix C

Definition of operational parameters

The requirements used to assess the ability of a navigation system to support precision approach and landing operations are the *Required Navigation Performances (RNP)*. These RNPs are adapted from the enroute RNP concept presented in [ICA94a], and are still under development in the AWOP. RNP type is a designator that specifies the 95 % accuracy value associated with the RNP space in the horizontal plane, thus defining a containment region [ICA94a]. For CAT I, II and III operations, the associated RNP types are those presented in the first line of table 2.1. In that case, RNP types include specification of lateral as well as vertical performance standards. The RNPs are expressed in terms of the accuracy, the integrity, the continuity of service and the availability. The definition of these parameters is recalled in [ICA94b], and collected in table C.1.

Parameter	Definition
Accuracy	Ability of the total system to maintain the aircraft position within a total system error (TSE) limit with a 95% probability at each point along the specified procedure and to keep it within an outer performance boundary with a probability of no less than 1-10^{-7}.
Integrity	Quality which relates to the trust that can be placed in the correctness of the information supplied by the total system. Integrity includes the ability of a system to provide timely and valid warnings to the user when the system must not be used for the intended operation. The integrity risk is the probability of an undetected failure which will result in the loss of the specified accuracy.
Availability	Ability of the total system to perform its function at the initiation of the intended operation. The availability risk is the probability that the required guidance will not be present at the initiation of the intended operation.
Continuity of service	Ability of the total system to perform its function without interruption during the intended operation. The continuity risk is the probability that the system will be interrupted and not provide guidance information for the intended operation.

Table C.1: *ICAO's definition of operational parameters.*

Appendix D

Definition of tunnel concept

The precision approach requirements are expressed in terms of Required Navigation Performance (RNP) parameters such as *accuracy*, *integrity*, *continuity of service* and *availability*. These parameters generate volumes around the nominal approach path within which ones the aircraft must fly with a specified probability. In practice, these volumes are delimited by surfaces defining *tunnels*.

For each category, two tunnels are defined according to the associated probability of presence:

- the *inner tunnel* is the volume in which the aircraft must be contained 95% of the time.
- the *outer tunnel* is the volume in which the aircraft must be contained with a probability of 1-10^{-7}.

Figure D.1 illustrates the tunnel concept.

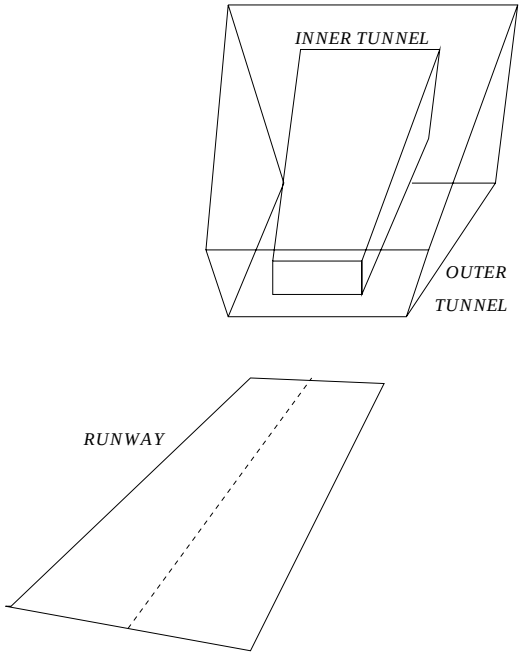

Figure D.1: *Illustration of tunnel concept.*

The position error driving the deviation of the aircraft around the assigned approach path is the *Total System Error (TSE)*. This error is a measure of the true aircraft position relative to the desired position. Part of this position error is due to the *Navigation Sensor Error (NSE)*, and another part is due to the inability of the aircraft's pilot or autopilot to fly precisely the desired trajectory. This second part is referred to as the *Flight Technical Error (FTE)*.

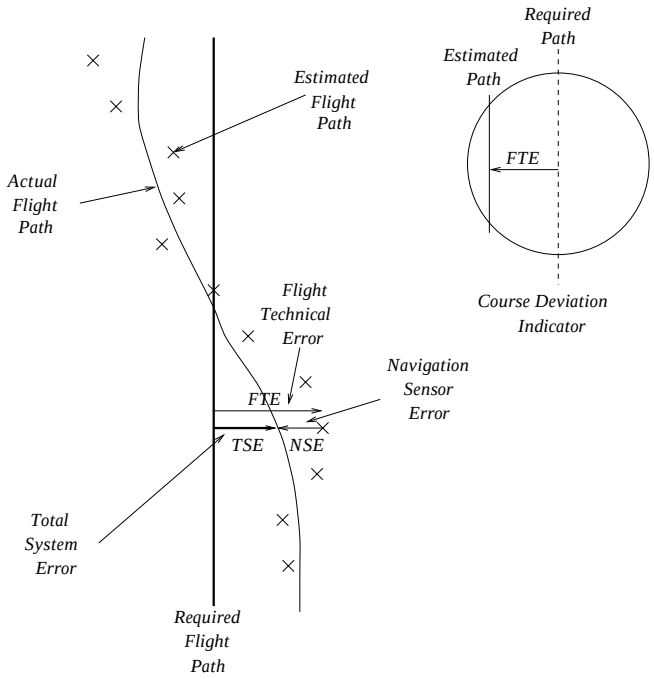

Figure D.2: *Ilustration of TSE=FTE+NSE. The reference used by the Course Deviation Indicator when coupled to the GNSS receiver is the theoretical Required Flight Path. When coupled to an ILS equipment, the CDI is centered on the sensed null DDM position.*

Assuming these error components are random and independent, the standard deviation of the Total System Error can be expressed as:

$$\sigma_{TSE}^2 = \sigma_{FTE}^2 + \sigma_{NSE}^2 \tag{D.1}$$

Appendix E

Carrier phase multipath errors

The carrier phase tracking error ε_{mult_i} induced by multipath can be computed using the structure of the receiver.

For example, when the disturbing signal is one specular reflected ray, the signal fed to the PLL can be modeled as:

$$V_i(t) = R(\hat{\tau} - \tau_0)\sin\left(2\pi f(t-\tau_0) + \theta_0\right) + aR(\hat{\tau} - \tau_1)\sin\left(2\pi f(t-\tau_1) + \theta_1\right) \tag{E.1}$$

where

- R is the autocorrelation function of the tracked C/A code
- $\hat{\tau}$ is the code phase delay estimated by the DLL and used to unspread the signal
- τ_0 is the true phase delay of the direct signal
- θ_0 is the original phase shift of the direct signal
- a is the relative amplitude of the reflected ray ($0 \leq a \leq 1$)
- τ_1 is the total code phase delay of the reflected ray
- θ_1 is the phase shift of the reflected signal

This signal has the same phase as the signal

$$V_\phi(t) = \sin\left(2\pi f(t-\tau_0) + \theta_0\right) + a\frac{R(\hat{\tau} - \tau_1)}{R(\hat{\tau} - \tau_0)}\sin\left(2\pi f(t-\tau_1) + \theta_1\right) \tag{E.2}$$

or

$$V_\phi(t) = \sin\left(2\pi f(t-\tau_0) + \theta_0\right) + \alpha\sin\left(2\pi f(t-\tau_1) + \theta_1\right) \tag{E.3}$$

or equivalently

$$V_\phi(t) = \sin\left(2\pi ft + \phi_0\right) + \alpha\sin\left(2\pi ft + \phi_1\right) \tag{E.4}$$

where

- $\alpha = a\frac{R(\hat{\tau}-\tau_1)}{R(\hat{\tau}-\tau_0)}$
- $\varphi_0 = -2\pi f\tau_0 + \theta_0$
- $\varphi_1 = -2\pi f\tau_1 + \theta_1$

Therefore, we have

$$V_\Phi(t) = A\sin(2\pi ft + \varphi_0 + \delta\varphi) \tag{E.5}$$

where

$$\delta\varphi = \arctan\left(\frac{\alpha\sin\delta\varphi_1}{1+\alpha\cos\delta\varphi_1}\right) \tag{E.6}$$

denoting $\delta\varphi_1 = \varphi_1 - \varphi_0$ the total path length difference between the direct signal and the reflected ray.

The measurement error $\delta\varphi$ is illustrated in figure E.1.

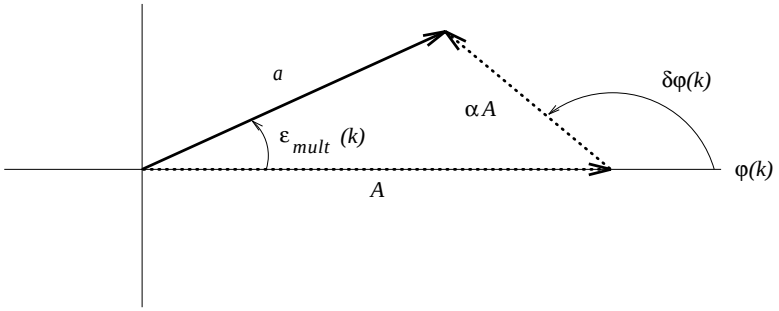

Figure E.1: *Composition of the direct and reflected ray ($\delta\varphi$ and α are the relative phase and amplitude of the reflected signal).*

We can see in this figure that the largest measurement error is obtained when the composite signal is perpendicular to the direct ray, which corresponds to a phase error of $\pm\frac{\pi}{2}$, or $\frac{1}{4}$ of a wavelength. Of course, this value is a bound, as in that case, the amplitude of the resulting signal is 0. This result can also be shown using E.6 when α=1 and $\delta\varphi_1 \to \pi$.

Therefore, we have [LEI95]

$$-\frac{\pi}{2} < \delta\varphi < \frac{\pi}{2} \tag{E.7}$$

Appendix F

Spatial correlation of satellite clock errors

Satellite clock errors affecting measurements performed by two receivers are identical if the signal used for measurements is transmitted at the same time. However, the length of the electrical path from one satellite to two distinct receivers is different because of the distance separating these two receivers. Thus, as illustrated in figure F.1, the time of transmission of the signal reaching two distinct receivers at the exact same time is different.

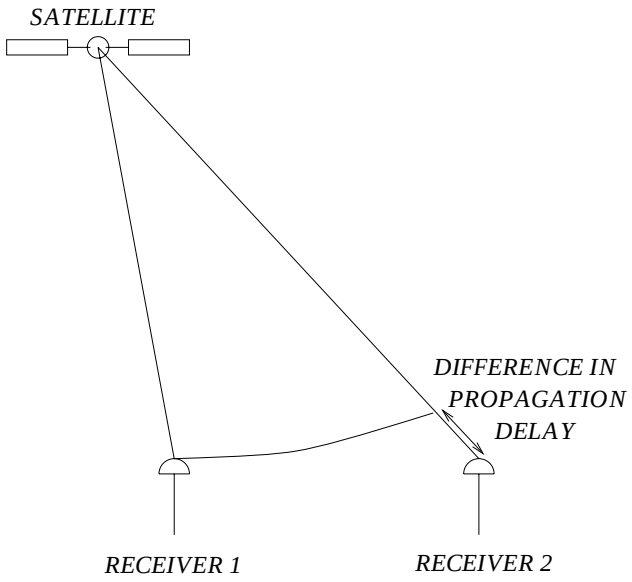

Figure F.1: *Illustration of the difference in time of transmission of a signal reaching two distinct receivers at the same time.*

This implies that the satellite clock offset, including SA dither are different for two measurements performed at the same time by two receivers. The maximum value of this time difference is observed when both receivers and the satellite are aligned. This is obtained when the satellite is at its lowest point on the horizon for two receivers on the ground. Thus, the difference in path length can be considered as identical to the distance separating the two receivers. Therefore, for two receivers located 20 km apart, the maximal difference in time of transmission is around 70 μs.

However, the GPS satellite clocks have a short term stability lower than 10^{-11} s.s^{-1}, and the evolution of SA has been specified to be lower than 2 m.s^{-1} [NN95], the equivalent of 7.10^{-9} s.s^{-1}. Thus,

the evolution of the satellite clock offset, including SA-dither, is highly negligible during this interval.

In practice, measurements from two distinct receivers can not be made at the exact same time because of their difference in clock offset. However, re-synchronization of one set of the measurements with respect to the other set can be made through proper extrapolation, with a timing accuracy equivalent to the uncertainty of determination of both clock offsets. In practice, the receiver clock offset can be estimated with an approximate 95 % accuracy of 300 ns , as specified in [NAT93]. Therefore, the extrapolated measurements are computed with a total 600 ns timing accuracy, which must be added to the 70 μs offset determined previously. However, the resulting evolution of the satellite clock offset and SA-dither during this interval is negligible.

Appendix G

Ionospheric errors

The *ionosphere* is a weakly ionized region extending from 50 km above the ground up to about 1000 km, although effects of higher layers up to the height of the satellites are sometimes not negligible [KLO96]. The ionosphere is a dispersive medium, causing an equal phase advance and code delay of opposite signs. The effect of the ionosphere on the propagation of GPS signals depends on the solar ionization flow, magnetic activity, solar spot cycle, season, time, position and line of sight. This effect is difficult to model, and complex algorithms can only compensate a maximum of 75% of the ionospheric delay, due to presently unmodelable variability of the ionosphere. Thus, simple models are often used, compensating only for 50% of the total ionospheric delay.

A very simple thin shell model of the ionosphere is illustrated in figure G.1.

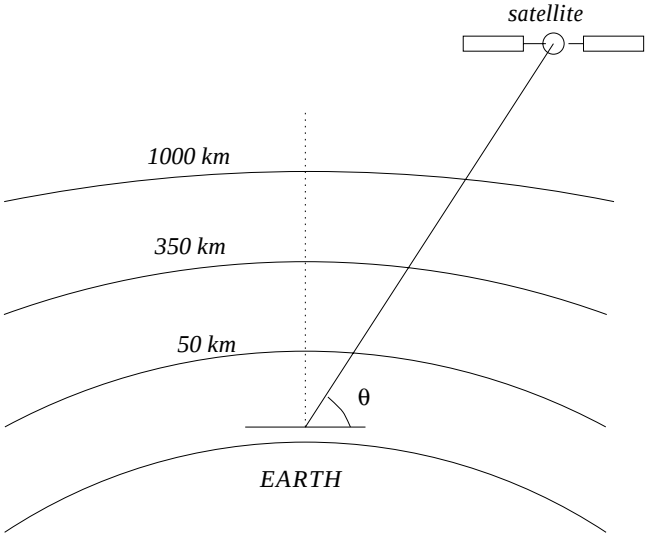

Figure G.1: *Illustration of the thin shell model of the ionosphere : all the free electrons of the ionosphere are supposed to be located at the height of maximum ionization, estimated to be around 350 km.*

Based on this model, a mathematical expression of the ionospheric delay is presented in [XIA92] and is recalled here:

$$I_i = \frac{40.3}{cf^2} \times TEC = \frac{40.3}{cf^2} \times \frac{TEC_0}{\sqrt{1 - \left(\frac{cos\theta}{1+\frac{6378}{350}}\right)^2}} \tag{G.1}$$

where

- TEC is the Total Electron Content, which denotes the total number of electrons encountered

by the oblique electromagnetic ray in a 1m^2 cross-section column of the ionosphere. TEC is expressed in electrons.m^{-2}. Extreme values of TEC are 10^{16} el.m^{-2} and 10^{19} el.m^{-2}.

- TEC_0 is the zenith Total Electron Content, related to the original TEC through the *obliquity function*.
- θ denotes the *elevation angle* of the satellite above the horizon from the receiver's point of view.

Computation of the ionospheric delay is performed for various elevation angles in figure G.2.

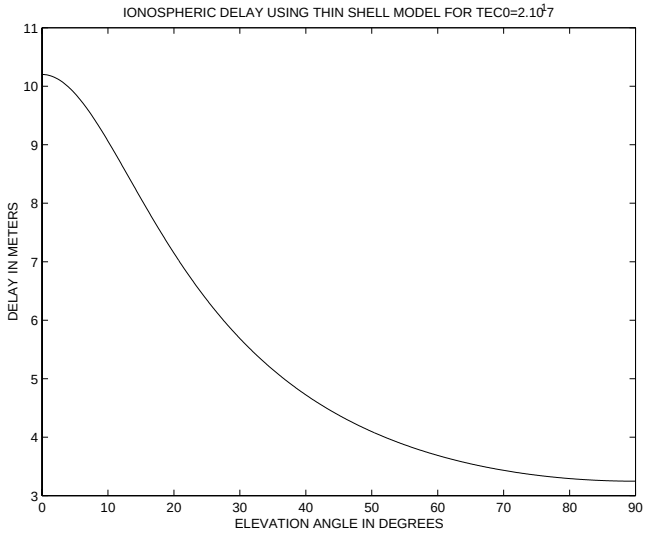

Figure G.2: *Ionospheric propagation delay as a function of elevation angle when* TEC_0*=2.10*^{17}.

As we can see in figure G.2, variation of ionospheric delay increases as the elevation angle decreases. Therefore, in normal conditions, differences in ionospheric propagation delays for two receivers are observed at low elevation angles.

The evolution of these ionospheric residuals for two receivers located as illustrated in figure G.3, tracking a satellite signal with an elevation angle around 5^o, is plotted in figure G.4.

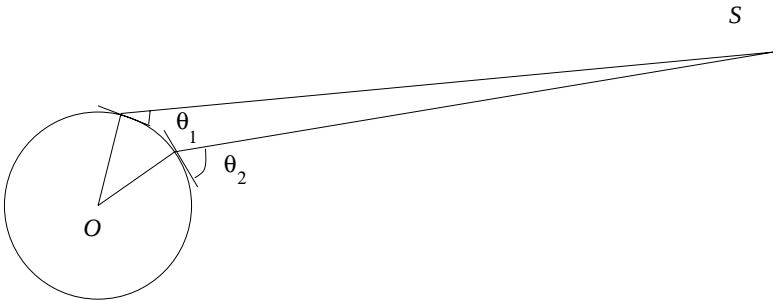

Figure G.3: *Situation of two receivers tracking the same satellite.*

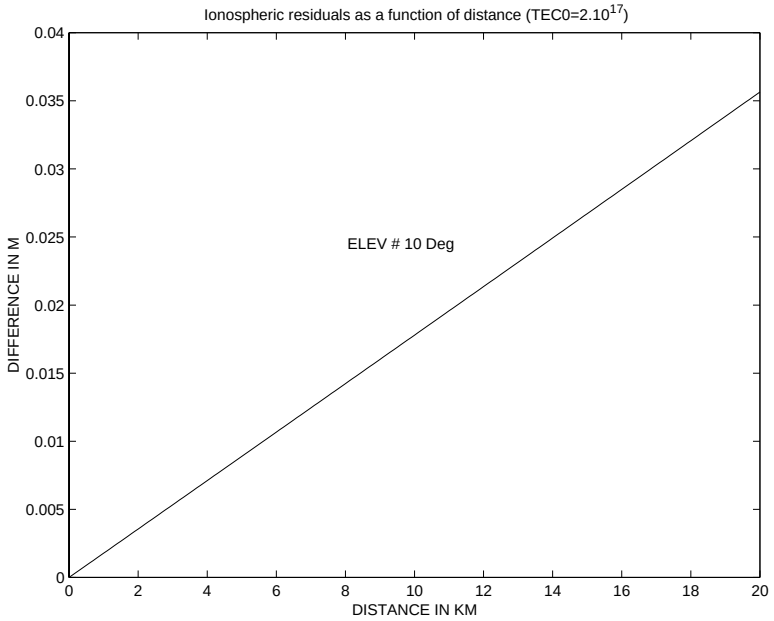

Figure G.4: *Evolution of the difference in ionospheric delays as a function of distance between the two receivers, located at the same height above sea level. The first receiver tracks the satellite with a fixed 10° elevation angle.*

Appendix H

Tropospheric propagation delay

Tropospheric effects are generated by the non-ionized portion of the atmosphere extending from the surface of the Earth up to an approximate altitude of 40 km [SPI96b]. The *troposphere* behaves as a neutral medium at the L-band frequencies. It causes a refraction of the RF signals because of the larger refractive index than that of vacuum. This index is constant with frequency, *non dispersive* for frequencies lower than 30 GHz. Thus the group and phase velocities are identical [ROC88]. In nominal propagation conditions, the actual path of the RF ray through the troposphere is longer than the straight geometrical line, bent in such a way that the curved path is closer to the zenith than the straight line, as shown in figure H.1. However, in reality, the actual path could be even more disturbed.

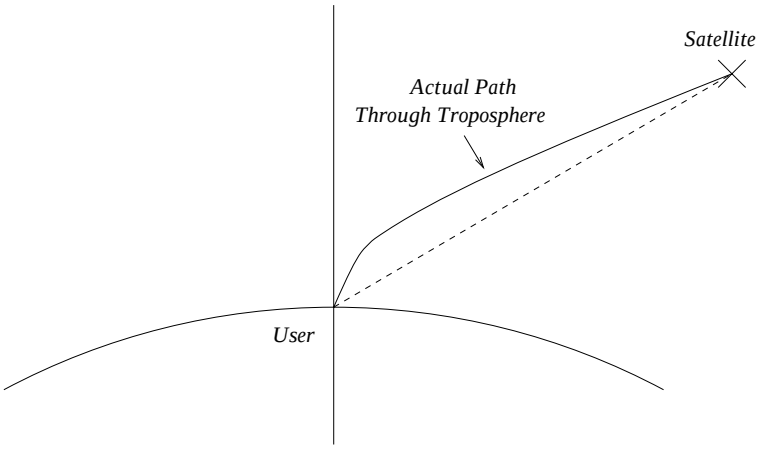

Figure H.1: *Actual path of the RF ray is longer than straight geometrical path.*

The tropospheric delay depends on the temperature, humidity, pressure, and height of receiver. This delay results of the action of two types of constituents : *dry gases* and *water vapor*. The *wet component* of this delay is much more difficult to predict than the *dry component*, although it contributes to only 10 % of the total delay. This uncertainty, combined with the unknown local meteorological conditions, limits the prediction accuracy using global models to the 10-20 cm level [JLN89]. Several models of this delay are proposed. Most of them model the total delay as the product of the zenith delay by a mapping function depending on the elevation angle. These models were extensively compared in [JLN89] and [JLN91]. The impact of different tropospheric models on the reliability and accuracy of the precise airborne positioning solutions is analyzed in [MCL95] and [CL96]. Two models are given here. The first one is an easy to use model, only depending on the height of the receiver and the elevation angle of the satellite. This model is presented in [NAT93]. The second one was presented in [SAA73] and is considered as the best available [JLN89, JLN91]. It is more

complex as it includes atmospheric and partial water vapor pressure, and temperature. Application of this model can be performed through the use of a standard atmosphere profile.

H.1 NATO tropospheric model

The model presented in [NAT93] uses an average reference value for surface refractivity which is input into a three stage equation decomposing the troposphere in three layers.

$$\tau = \Delta R(h) f(\theta) \tag{H.1}$$

where

- $f(\theta)$ is the *obliquity factor (or mapping function)* as a function of the elevation angle θ. We have $f(\theta) = \frac{1}{sin\theta + \frac{0.00143}{tan\theta + 0.0455}}$. This function is actually the Chao dry delay mapping function, as presented in [CHA72].
- $\Delta R(h)$ is the *zenith propagation delay*, depending on altitude above mean sea level. Different expressions of this delay can be given depending on the altitude of the receiver.

The total delay is decomposed as $\Delta R(h) = \Delta R_1(h) + \Delta R_2(h) + \Delta R_3(h)$ where

- $\Delta R_1(h)$ is the error for an altitude $0 < h < 1$ km :

$$\Delta R_1(h) = \left(N_s(1-h) + 0.5\Delta N(1-h^2)\right) \times 10^{-3} \text{ m} \tag{H.2}$$

  N_s is the surface refraction index at the mean sea level, distributed with a mean of 324.8N and a standard deviation of 25.98N. The unit N is such that $N = (n-1)\times 10^6$. ΔN=-7.32$e^{0.005577 * N_s}$. $\Delta R_1(h)$=0 if $h < 1$ km.

- $\Delta R_2(h)$ is the error for an altitude 1 km$< h <$9 km :

$$\Delta R_2(h) = \frac{-8N_1}{ln\left(\frac{N_1}{105}\right)} \left(e^{-ln\left(\frac{N_1}{105}\right)} - e^{0.125(1-h)ln\left(\frac{N_1}{105}\right)}\right) \times 10^{-3} \text{ m} \tag{H.3}$$

  where $N_1 = N_S + \Delta N$. $\Delta R_2(h) = 0$ if $h \leq$9 km, and $\Delta R_2(h) = 0.1430$ m if $h \geq 9$ km .

- $\Delta R_3(h)$ is the error for an altitude 9 km $< h <$ 20186.8 km :

$$\Delta R_3(h) = \frac{-105}{142.4} \left(e^{-2873.3187} - e^{0.1424(h-9)}\right) \times 10^{-3} \text{ m} \tag{H.4}$$

  $\Delta R_3(h)$=0.732 m if $h < 9$ km.

Computation of the tropospheric delay is performed for various elevation angles in figure H.2.

H.2 Saastamoinen's tropospheric model

The model presented in [SAA73] relates the tropospheric delay to the meteorological parameters in the following manner :

$$\tau = \frac{0.00227}{cos\theta} \left[P + \left(\frac{1255}{T} + 0.05\right) e - tan^2\theta\right] \text{ in meters} \tag{H.5}$$

where

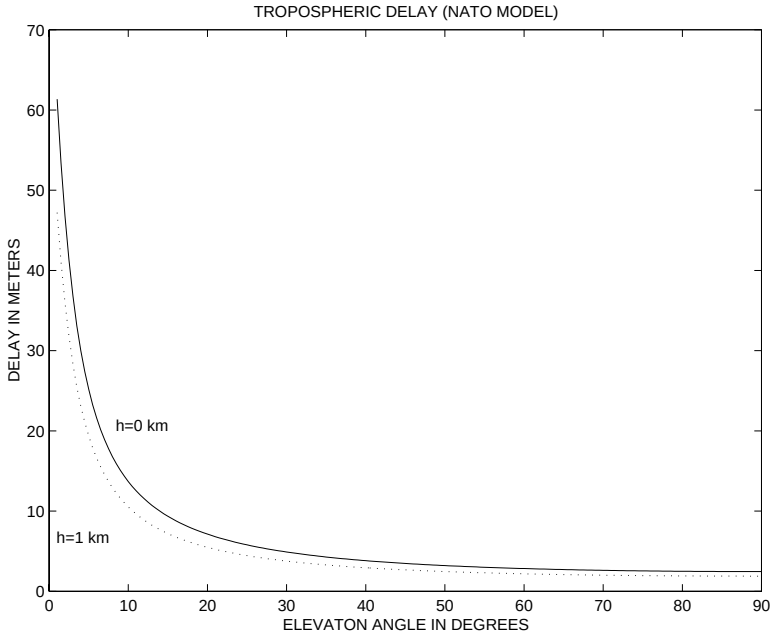

Figure H.2: *Evolution of tropospheric delay as a function of altitude and elevation angle. This model was reported to be suitable for precision airborne navigation in [CL96].*

- θ is the satellite *elevation angle*.
- P is the *atmospheric pressure* in mbar.
- T is the *temperature* in Kelvin.
- e is the *partial water vapor pressure* in mbar.

Computation of this estimated tropospheric delay requires knowledge of meteorological parameters. These parameters can be measured at the site or predicted from a standard atmosphere model. As reported in [BT94], the use of measured meteorological parameters does not yield to more accurate results than the use of standard parameters. An example of standard atmosphere mapping is presented below :

$$P = P_0[1 - 2.26 \cdot 10^{-5}(h - h_0)]^{5.225} \text{ in mbar} \tag{H.6}$$

$$T = T_0 - 6.5 \cdot 10^{-3}(h - h_0) \text{ in K} \tag{H.7}$$

$$e = \frac{RH_0}{100} e^{\left(-6.396 \cdot 10^{-4}(h-h_0) - 37.2465 + 0.2113166T - 2.56908 \cdot 10^{-4}T^2\right)} \text{ in mbar} \tag{H.8}$$

where h is the height of the receiver above the ground in meters, and RH_0 is the relative humidity in percent ($0 \leq RH_0 \leq 100$).

Estimation of differences in tropospheric delays between two receivers

As we can see in figure H.2, the variation of the tropospheric delay is very rapid when the elevation angle is close to 0^o. Therefore, when two receivers track the same satellite as illustrated in figure G.3, the tropospheric delay will be quite different if this satellite is low on the horizon, as the elevation angle will differ from one receiver to the other. This difference is plotted in figures H.3 and H.4.

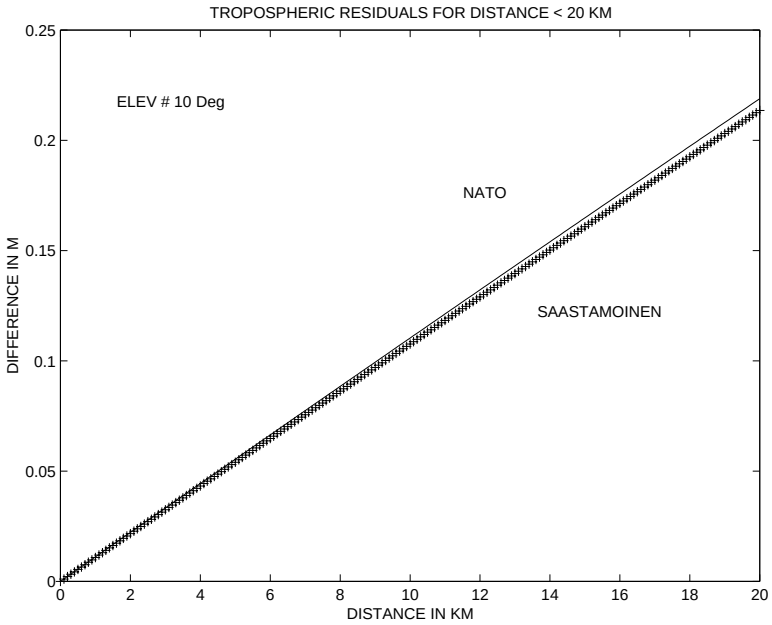

Figure H.3: *Illustration of differences in tropospheric delay for two receivers located at the same height tracking the same satellite. The first receiver tracks the satellite with a fixed 10º elevation angle.*

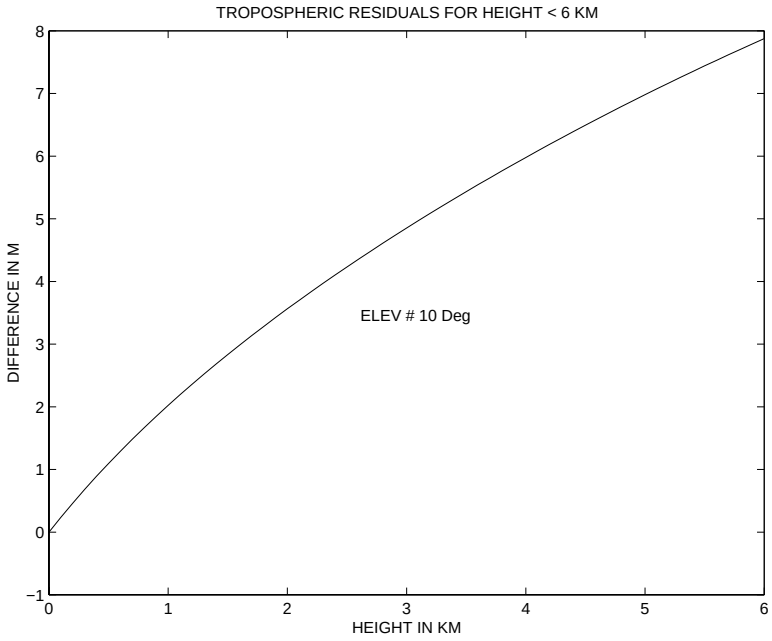

Figure H.4: *Illustration of differences in tropospheric delay for two receivers at the same latitude and longitude tracking the same satellite. The first receiver tracks the satellite with a fixed 10º elevation angle.*

Appendix I

Impact of error of computation of satellite position

The positions of the satellites are necessary in order to process the *slant range* measurements performed by the receiver. The distance measured is the distance between the receiver at the time of reception and the satellite at the time of transmission. Computation of the position of the satellites is performed using the *ephemeris data* broadcast by the satellites and an estimate of the time of transmission. Inaccuracies in the ephemeris data and in the time estimate can induce errors in the estimated positions of satellites. The user position error induced by a satellite position error is projected on the *line of sight* of the satellite, as illustrated in figure I.1.

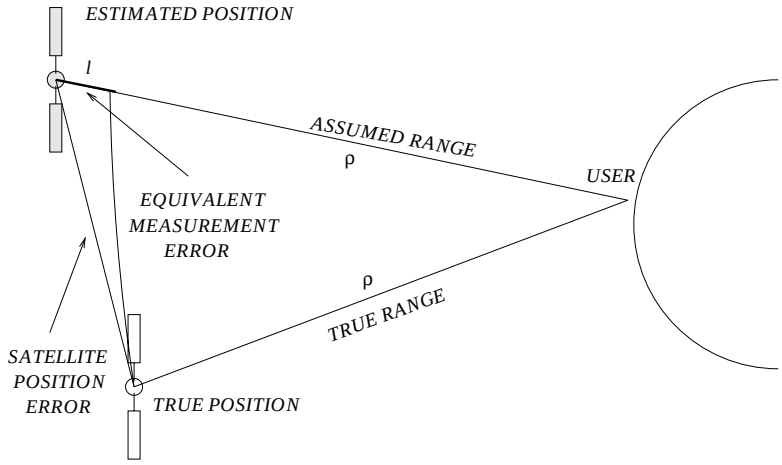

Figure I.1: *Impact of a satellite position error on the user position estimate.*

Thus, in the worst case, this error can be reported entirely on the user position when the assumed position of the satellite is aligned with its true position and the user position. However, when using measurements from another receiver in the same area, these errors can be reduced if they are correlated, as the lines of sights of the satellite from the receivers are almost identical. If both receivers compute the position of the satellite with the same error, the residual error appearing in the single differences is the difference between the two projections, as presented in figure I.2.

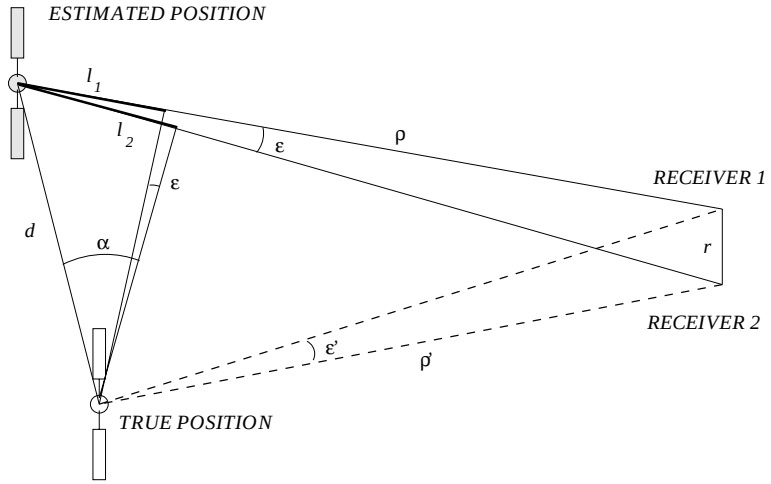

Figure I.2: *Difference in range measurement error for two receivers. As the altitude of the satellites is very large ($\approx$ 20000 km) as compared with the position error d, we can assume that the measurement errors l_1 and l_2 are the result of orthogonal projection on the line of sight of the satellite.*

As shown in [BP82], the equivalent range error on single differences is

$$\Delta l = dsin\alpha - dsin(\alpha - \varepsilon) \tag{I.1}$$

As ε is small, we can approximate I.1 as

$$\Delta l = d\varepsilon cos\alpha \tag{I.2}$$

As $\varepsilon \leq \frac{r}{\rho}$, the largest value of this error is

$$|\Delta l| \leq \frac{dr}{\rho} \tag{I.3}$$

The evolution of this equivalent range measurement error is plotted in figure I.3 for various values of d and r.

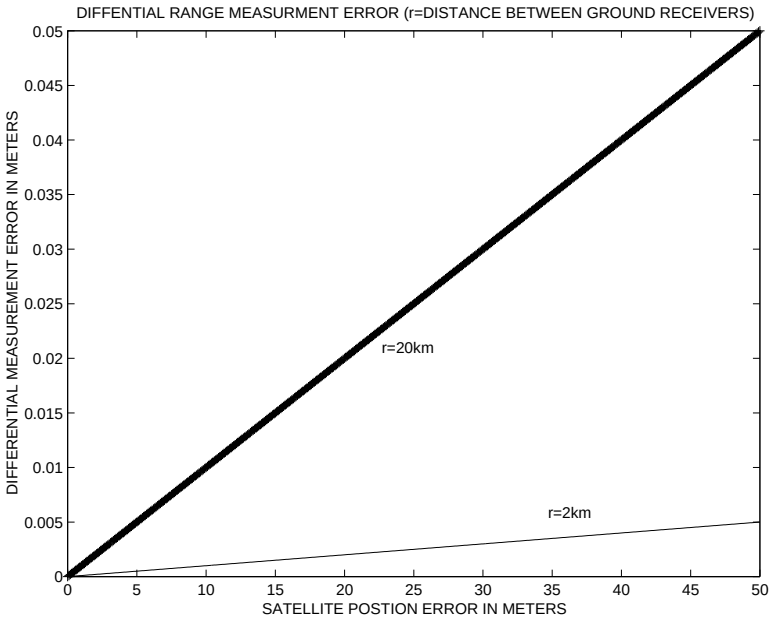

Figure I.3: *Differential range measurement error induced by errors in the computed satellite position.*

Errors in the ephemeris data are due to the limitations of the control segment to estimate the kinematic parameters of the satellites, and to the possible intentional degradation called *SA-epsilon*. These errors induce common satellite position errors for both receivers. The standard deviation of these errors is around 5 m [ZB96], which induces an error lower than 1 cm on the single differenced measurements when both receivers are located less than 20 km apart, as shown in figure I.3.

The time of reception is provided by the local oscillator, biased by its own clock offset, while the time of transmission is computed using an iterative algorithm. As the receiver clock bias can be estimated with an error lower than 300 ns [NAT93], we can assume that the time of transmission can be determined with an error lower than 1 μs. Thus, as the maximum speed of a GPS satellite in the WGS-84 reference frame is lower than 4 km.s^{-1} [AS96], we can deduce that this time error induces an error lower than 1 cm on each range measurement.

Appendix J

Kullback-Leibler information

The Kullback-Leibler information between two probability density functions f_{θ_0} and f_{θ_1} of a random variable Y is [BN93]:

$$D\left(f_{\theta_0}, f_{\theta_1}\right) = E_{\theta_0}\left[ln\frac{f_{\theta_0}(Y)}{f_{\theta_1}(Y)}\right] \tag{J.1}$$

The Kullback-Leibler information is equal to 0 if and only if both distributions f_{θ_0} and f_{θ_1} are identical. This information is not a distance stricly speaking because it is not symmetrical in general. However, it is often called the Kullback-Leibler distance.

In the case where Y has a gaussian distribution with variance σ^2, and f_{θ_0} and f_{θ_1} only differ by the expected value θ_0 and θ_1, we have

$$D\left(f_{\theta_0}, f_{\theta_1}\right) = \frac{1}{2}\frac{(\theta_0 - \theta_1)^2}{\sigma^2} \tag{J.2}$$

As we can see from (J.2), the Kullback-Leibler information can be interpreted as a *signal-to-noise ratio* representing the degree of distinction between the two probability density functions, as illustrated in figure J.1.

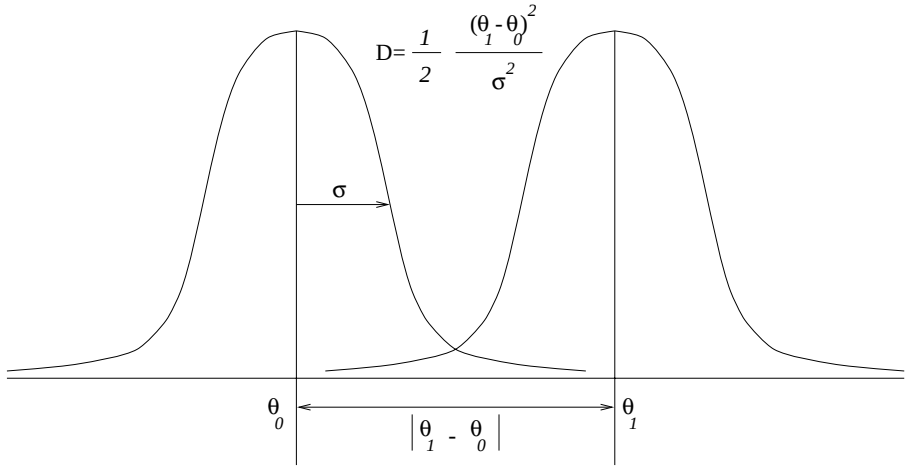

Figure J.1: *Representation of the Kullback-Leibler information between two hypotheses in the scalar case.*

Moreover, it can be shown that the Kullback-Leibler distance between two multivariate normal distributions f_{θ_0} and f_{θ_1} is [BN93]:

$$D(f_{\theta_0}, f_{\theta_1}) = \frac{1}{2}\left(E_{f_{\theta_0}}[z_{S_{\alpha\beta\gamma}}] - E_{f_{\theta_1}}[z_{S_{\alpha\beta\gamma}}]\right)^T \Sigma^{-1} \left(E_{f_{\theta_0}}[z_{S_{\alpha\beta\gamma}}] - E_{f_{\theta_1}}[z_{S_{\alpha\beta\gamma}}]\right) \quad \text{(J.3)}$$

where Σ is the covariance matrix of the distribution.

Appendix K

Linearization of GPS observations

The GPS pseudo-range measurements delivered by a receiver do not depend on the position of the receiver in a *linear* fashion. Therefore, classical linear identification techniques can not be used to process these measurements. However, when a good position estimate of the receiver is available, the model of these measurements can be linearized for further processing.

K.1 Linearization of undifferenced measurements

A simple model of the GPS measurements can be formed from equations 3.23 and 3.25:

$$P_i(k) = \rho_i(k) + n_i(k) \tag{K.1}$$

$$\varphi_i(k) = -\frac{\rho_i(k)}{\lambda} - N_i + b_i(k) \tag{K.2}$$

where

- n_i and b_i denote all the measurement errors affecting the code and carrier phase measurements.
- $\rho_i(k)$ is the geometrical distance between the satellite i and the receiver:

$$\rho = \sqrt{(x - x_i)^2 + (y - y_i)^2 + (z - z_i)^2} \tag{K.3}$$

  where

  - $X = [x, y, z]^T$ is the position of the receiver
  - $X_i = [x_i, y_i, z_i]^T$ is the position of the satellite

As we can see from these equations, the measurements do not linearly depend on the unknown position $X = [x, y, z]^T$.

Assume now that a position estimate $\hat{X}$ is available. We can expand the models K.1 and K.2 around this estimate to create a linear dependency with respect to the position X.

Denoting δX as the estimation error $\delta X = \hat{X} - X$, we can expand the equation K.3 as:

$$\rho(X) = \rho(\hat{X} - \delta X) \approx \rho(\hat{X}) - \frac{\partial \rho}{\partial X}\delta X \tag{K.4}$$

The resulting linearized quantities $\delta\rho = \rho(X) - \rho(\hat{X})$ depend on the unknown position as:

$$\delta\rho = -\frac{\partial \rho}{\partial X}\delta X \tag{K.5}$$

where

$$\frac{\partial \rho}{\partial X} = \left[\begin{array}{ccc} \frac{\partial \rho}{\partial x} & \frac{\partial \rho}{\partial y} & \frac{\partial \rho}{\partial z} \end{array} \right] \tag{K.6}$$

These partial derivatives are in fact the *direction cosines* of the satellites from a receiver located in $\hat{X}$:

$$\frac{\partial \rho}{\partial x} = \frac{\hat{x} - x_i}{\sqrt{(\hat{x} - x_i)^2 + (\hat{y} - y_i)^2 + (\hat{z} - z_i)^2}} \tag{K.7}$$

also denoted $[C_x, C_y, C_z] = \left[\begin{array}{ccc} \frac{\partial \rho}{\partial x} & \frac{\partial \rho}{\partial y} & \frac{\partial \rho}{\partial z} \end{array} \right]$

Therefore, the measurements presented in K.1 and K.2 are linearized as:

$$\delta P_i(k) = P_i(k) - \rho_i(\hat{X}) = -C_{x_i}(k)\delta x(k) - C_{y_i}(k)\delta y(k) - C_{z_i}(k)\delta z(k) + n_i(k) \tag{K.8}$$

$$\delta \phi_i(k) = \phi_i(k) + \frac{\rho_i(\hat{X})}{\lambda} = \frac{C_{x_i}(k)}{\lambda}\delta x(k) + \frac{C_{y_i}(k)}{\lambda}\delta y(k) + \frac{C_{z_i}(k)}{\lambda}\delta z(k) - N_i + b_i(k) \tag{K.9}$$

K.2 Linearization of single differenced measurements

When measurements from a second receiver are available, single differenced measurements can be formed in order to remove many of the measurement errors except errors related to the receiver itself, as presented in section 4.2. Single differences are computed by subtracting measurements from one receiver to the measurements of the other one, after proper resynchronization.

A model of these observations is presented in section 4.2 and is recalled here:

$$\Delta P_i(k) = \Delta \rho_i(k) + \Delta n_i(k) \tag{K.10}$$

$$\Delta \varphi_i(k) = -\frac{\Delta \rho_i(k)}{\lambda} - \Delta N_i + \Delta b_i(k) \tag{K.11}$$

where

- $\Delta n_i(k) = n_{R_i}(k) - n_{U_i}(k)$ and $\Delta b_i(k) = b_{R_i}(k) - b_{U_i}(k)$ denotes all the residual measurement errors (subscripts R and U denote the Reference measurements and the User measurements).
- $\Delta \rho_i(k) = \rho_{R_i}(k) - \rho_{U_i}(k)$ is the difference between the satellite-reference range and the satellite-user range: $\rho_{R_i} = \rho(X_R)$ and $\rho_{U_i} = \rho(X)$, denoting X_R as the reference coordinates and X as the user coordinates.

As the position of the reference receiver X_R is accurately known, linearization of these observations around a user position estimate $\hat{X}$ results in:

$$\begin{aligned} \delta \Delta P_i(k) &= \Delta P_i(k) - (\rho_i(X_R) - \rho_i(\hat{X})) \\ &= C_{x_i}(k)\delta x(k) + C_{y_i}(k)\delta y(k) + C_{z_i}(k)\delta z(k) + \Delta n_i(k) \end{aligned} \tag{K.12}$$

$$\begin{aligned} \delta \phi_i(k) &= \phi_i(k) - \left(\frac{\rho_i(X_R)}{\lambda} - \frac{\rho_i(\hat{X})}{\lambda} \right) \\ &= -\frac{C_{x_i}(k)}{\lambda}\delta x(k) - \frac{C_{y_i}(k)}{\lambda}\delta y(k) - \frac{C_{z_i}(k)}{\lambda}\delta z(k) - N_i + \Delta b_i(k) \end{aligned} \tag{K.13}$$

K.3 Linearization of double differenced measurements

In order to remove the last part of the measurements errors related to the receiver itself from the single differenced measurements, the elaboration of between satellite differences is computed, as presented in section 4.3.

A model of these observations is presented in section 4.3 and is recalled here:

$$\nabla\Delta P_i(k) = \nabla\Delta\rho_i(k) + \nabla\Delta n_i(k) \tag{K.14}$$

$$\nabla\Delta\varphi_i(k) = -\frac{\nabla\Delta\rho_i(k)}{\lambda} - \nabla\Delta N_i + \nabla\Delta b_i(k) \tag{K.15}$$

where

- the reference satellite is assumed to be satellite 1.
- $\nabla\Delta\rho_i$ denotes the double differenced range measurements:

$$\nabla\Delta\rho_i = \Delta\rho_1 - \Delta\rho_i = (\rho_{R_1} - \rho_{U_1}) - (\rho_{R_i} - \rho_{U_i}) \tag{K.16}$$

Linearization of this model produces the following observations:

$$\begin{aligned}
\delta\nabla\Delta P_i(k) &= \nabla\Delta P_i(k) - \left(\Delta\rho_1\left(\hat{X}(k)\right) - \Delta\rho_i\left(\hat{X}(k)\right)\right) \\
&= \left(\Delta P_1(k) - \Delta\rho_1(\hat{X}(k))\right) - \left(\Delta P_i(k) - \Delta\rho_i(\hat{X}(k))\right) \\
&= \left(C_{x_1}(k) - C_{x_i}(k)\right)\delta x + \left(C_{y_1}(k) - C_{y_i}(k)\right)\delta y + \left(C_{z_1}(k) - C_{z_i}(k)\right)\delta z \\
&\quad + \nabla\Delta n_i(k)
\end{aligned} \tag{K.17}$$

$$\begin{aligned}
\delta\nabla\Delta\varphi_i(k) &= \nabla\Delta\varphi_i(k) - \left(-\frac{\nabla\Delta\rho_1(\hat{X}(k))}{\lambda} + \frac{\nabla\Delta\rho_i(\hat{X}(k))}{\lambda}\right) \\
&= -\frac{C_{x_1}(k) - C_{x_i}(k)}{\lambda} - \frac{C_{y_1}(k) - C_{y_i}(k)}{\lambda} - \frac{C_{z_1}(k) - C_{z_i}(k)}{\lambda} \\
&\quad - \nabla\Delta N_i + \nabla\Delta b_i(k)
\end{aligned} \tag{K.18}$$

Collecting all the n_k observations made by the receivers, we can form the vector model:

$$P(k) = \lambda C(k)\delta X(k) + B_P(k) \tag{K.19}$$

$$\Phi(k) = -C(k) - N + B_\Phi(k) \tag{K.20}$$

where

- $P(k) = [\delta\nabla\Delta P_1(k) \ldots \delta\nabla\Delta P_{n_k}(k)]^T$ and $\Phi(k) = [\delta\nabla\Delta\varphi_1(k) \ldots \delta\nabla\Delta\varphi_{n_k}(k)]^T$
- B_P and B_Φ are the code and phase noise vectors
- $N = [\nabla\Delta N_1 \ldots \nabla\Delta N_{n_k}]^T$ is the double differenced ambiguity vector
- $C(k)$ is the linear system matrix

$$C(k) = \frac{1}{\lambda}\begin{bmatrix} C_{x_1}(k) - C_{x_2}(k) & C_{x_1}(k) - C_{x_2}(k) & C_{x_1}(k) - C_{x_2}(k) \\ \vdots & \vdots & \vdots \\ C_{x_1}(k) - C_{x_{n_k}}(k) & C_{x_1}(k) - C_{x_{n_k}}(k) & C_{x_1}(k) - C_{x_{n_k}}(k) \end{bmatrix} \tag{K.21}$$

Appendix L

Kalman filtering of GPS measurements in dynamic applications

A Kalman filter provides the Minimum Mean Square Estimate (MMSE) of the state of a system on the basis of a state transition and an observation model.

The measurements used by a Kalman filter in GPS stand-alone applications are code and/or phase measurements, in an undifferenced, single differenced or double differenced mode. The Kalman filter is used to estimate the kinematic parameters of the mobile (position, velocity, acceleration, ...), the user clock parameters (offset, drift, ...) and the ambiguities of the carrier phase measurements. As the measurement do not linearly depend on the state vector, the actual procedure is usually an extended Kalma filter.

The generic Kalman filter presented here is an extended Kalman filter applied on double differenced code and phase measurements and provides position, velocity and ambiguity estimates. It is based on the integrated random walk state transition model, and on a classical model for the double differenced measurements, as shown in equations L.1 and L.2.

$$X_{k+1} = F_k X_k + W_k \tag{L.1}$$

$$Y_k = h(X_k) + V_k \tag{L.2}$$

where

- X_k is the state vector at epoch k, where $X_k = [x_k, \dot{x}_k, y_k, \dot{y}_k, z_k, \dot{z}_k, N_1, \ldots N_{n_k}]^T$
- F_k is the state transition matrix, usually chosen as

$$F_k = \begin{bmatrix} F & 0 & 0 & 0 \\ 0 & F & 0 & 0 \\ 0 & 0 & F & 0 \\ 0 & 0 & 0 & I_{n_k} \end{bmatrix} \tag{L.3}$$

  where

  - $F = \begin{bmatrix} 1 & T_e \\ 0 & 1 \end{bmatrix}$ is the position transition matrix (integrated random walk).
  - I_{n_k} is the ambiguity transition matrix. It is identical to the identity matrix of rank n_k.

- W_k is the state noise, assumed to be Gaussian, and independent from X_k and from measurement Y_k. Its autocorrelation matrix is:

$$Q_k = \begin{bmatrix} \sigma_{q_x}^2 W & 0 & 0 & 0 \\ 0 & \sigma_{q_y}^2 W & 0 & 0 \\ 0 & 0 & \sigma_{q_z}^2 W & 0 \\ 0 & 0 & 0 & \sigma_N^2 I_{n_k} \end{bmatrix} \tag{L.4}$$

  where

  - $W = \begin{bmatrix} \frac{T_e^3}{3} & \frac{T_e^2}{2} \\ \frac{T_e^2}{2} & T_e \end{bmatrix}$ is the autocorrelation of the position state noise.
  - σ_q^2 is the variance of the acceleration of the mobile, assumed to be a white Gaussian noise.
  - σ_N^2 is the variance of the ambiguity noise model.

- Y_k contains the double differenced code pseudoranges stacked on top of the double differenced carrier phase measurements.

- h is the non linear function mapping the state components on the observations. $h(X_k)$ is actually the function $\nabla\Delta\rho_i(k)$ for the $n_k - 1$ double differenced code measurements, and the function $-\frac{\nabla\Delta\rho_i(k)}{\lambda}$ for the $n_k - 1$ double differenced phase measurements, as preseneted in section K.3.

- V_k is the measurement noise, assumed to be Gaussian, independent from X_k. Its autocorrelation matrix is:

$$R_k = \begin{bmatrix} \sigma_P^2 \Sigma_{\nabla\Delta} & 0 \\ 0 & \sigma_b^2 \Sigma_{\nabla\Delta} \end{bmatrix} \tag{L.5}$$

  where

  - σ_n^2 is the code pseudorange measurement noise
  - σ_b^2 is the carrier phase measurement noise
  - $\Sigma_{\nabla\Delta}$ is the double differenced correlation matrix:

$$\Sigma_{\nabla\Delta} = \begin{bmatrix} 4 & 2 & & & 2 \\ 2 & 4 & & & 2 \\ \vdots & & \ddots & & \vdots \\ 2 & & & 4 & 2 \\ 2 & & & 2 & 4 \end{bmatrix} \tag{L.6}$$

The update of the state estimate is computed using the following equations:

$$\hat{X}_{k+1|k} = F_k \hat{X}_k \tag{L.7}$$
$$\Sigma_{k+1|k} = F_k \Sigma_{k|k} F_k^T + Q_k \tag{L.8}$$
$$K_{k+1} = \Sigma_{k+1|k} H_{k+1}^T \left(H_{k+1} \Sigma_{k+1|k} H_{k+1}^T + R_{k+1} \right)^{-1} \tag{L.9}$$
$$\hat{X}_{k+1|k+1} = \hat{X}_{k+1|k} + K_{k+1} \left(Y_{k+1} - h\left(\hat{X}_{k+1|k} \right) \right) \tag{L.10}$$
$$\Sigma_{k+1|k+1} = \Sigma_{k+1|k} - K_{k+1} H_{k+1} \Sigma_{k+1|k} \tag{L.11}$$

where $H_k = \left. \frac{\partial h(X_{k+1})}{\partial X_{k+1}} \right|_{X_{k+1} = \hat{X}_{k+1|k}}$.

Note that the extended Kalman filter equations L.7-L.11 do not provide an optimal estimate of the state of the system, as they are derived using a first order Taylor expansion of the non linear function h around successive state estimates:

$$h(X_k) \approx h(\hat{X}_{k|k-1}) + H_k(X_k - \hat{X}_{k|k-1}) \tag{L.12}$$

The quantity $I_k = Y_{k+1} - h\left(\hat{X}_{k+1|k}\right)$ appearing in equation L.9 is called the *innovation vector* of the process. In the case where the state transition equation is linear, it can be shown that if L.12 holds, the innovation vector is zero-mean at the first order, and its covariance matrix is equal to

$$\Sigma_{I_k} = H_k \Sigma_{k|k-1} H_k^T + R_k \tag{L.13}$$

Bibliography

[ABI91] H.Z. ABIDIN. New strategy for 'on-the-fly' ambiguity resolution. In *Proceedings of ION-GPS-91, Albuquerque*, 1991.

[AS96] N. ASHBY and J. SPILKER. *Global Positioning System: Theory and Applications*, volume 1, chapter 'Introduction to Relativistic Effects', pages 623–697. AIAA, 1996.

[BH84] R. G. BROWN and P.Y.C. HWANG. A Kalman filter approach to precision GPS geodesy. *Navigation*, pages 155–166, 1984.

[BHW94] H. BLOMENHOFER, G. HEIN, and D. WALSH. On-The-Fly Carrier Phase Ambiguity Resolution for Precise Aircraft Landing. *International Journal of Satellite Communications*, 12:489–497, 1994.

[BLE90] G. BLEWITT. An Automatic Editing Algorithm for GPS Data. *Geophysical Research Letters*, 17(3):199–202, 1990.

[BN93] M. BASSEVILLE and I. NIKIFOROV. *Detection of Abrupt Changes*. Prentice Hall, 1993.

[BP82] J. BESER and B. PARKINSON. The Application of NAVSTAR Differential GPS in the Civilian Community. *Journal of the Institute of Navigation*, 29(2):107–198, 1982.

[BRA96] M. BRAASCH. *Global Positioning System: Theory and Applications*, volume 1, chapter 'Multipath Effects', pages 547–568. AIAA, 1996.

[BT94] F. BRUNNER and P. TREGONING. Tropospheric Propagation Effects in GPS Height Results Using Meteorological Observations. *Australian Journal of Geodesy, Photogrammetry and Surveying*, 60:49–65, 1994.

[BV94] C. BAUM and V. VEERAVALLI. A Sequential Procedure for Multihypothesis Testing. *IEEE Transactions on Information Theory*, 40(6):1994–2007, November 1994.

[BV95] C. BAUM and V. VEERAVALLI. Asymptotic Efficiency of a Sequential Multihypothesis Testing. *IEEE Transactions on Information Theory*, 41(6):1994–1997, November 1995.

[CHA72] C. CHAO. A Model for Tropospheric Calibration from Daily Surface and Radiosonde Balloon Measurements, technical memorandum 391-350. Technical report, Jet Propulsion Laboratory, may 1972.

[CHE95] D. CHEN. Fast Ambiguity Search Filter : A Noval Concept for GPS Ambiguity Resolution. In *proceedings of ION GPS-93, Salt Lake City, Utah*, September 1995.

[CL94] D. CHEN and G. LACHAPELLE. A Comparison of the FASF and Least-Squares Search Algorithms for Ambiguity Resolution On The Fly. In *proceedings of KIS94, BANFF*, pages 148–155, August 30 - September 2 1994.

[CL96] J. COLLINS and R. LANGLEY. Mitigating Tropospheric Propagation Delay Errors in Precise Airborne GPS Navigation. In *proceedings of IEEE Position Location and Navigation Symposium (PLANS), Atlanta, Georgia*, April 22-26 1996.

[CMMS97] H. CARVALHO, P. DEL MORAL, A. MONIN, and G. SALUT. Optimal Non Linear Filtering in GPS/INS Integration. *IEEE transactions on Aerospace and Electronic Systems*, 33(3):16, July 1997.

[DB96] D. DORIS and A. BENHALLAM. On Correlation Processes Reducing Multipath Errors in the L1 GPS Receiver. In *proceedings of ION GPS-96, Kansas City*. The Institute of Navigation, September 17-20 1996.

[DMA87] DMA. Department of Defense World Geodetic System 1984. its definition and relationships with local geodetic systems. Technical report, Defense Mapping Agency, September 1987.

[DoD95] DoD. *Global Positioning System Standard Positioning Service Signal Specification*, 2nd edition, June 1995.

[DOR97] D. DORIS. *GPS Multipath*. PhD thesis, LTST, ENAC, 1997.

[ESM+95] P. ENGE, E. SWANSON, R. MULLIN, K. GANTHER, A. BOMMARITO, and R. KELLY. Terrestrial Radionavigation Technologies. *Journal of the Institute of Navigation*, 42(1):61–108, Spring 1995.

[FAN88] FANS. *Special Comity of Future Air Navigation Systems. Fourth Meeting*. ICAO, 1988.

[FB90] E. FREI and G. BEUTLER. Rapid Static Positioning Based on the Fast Ambiguity Resolution Approach: The Alternative to Kinematic Positioning. In *proceedings of the Second International Symposium on Precise Positioning with GPS, GPS 90*. Canadian Institute of Geomatics, 1990.

[FRE91] E. FREI. Rapid differential positioning with the Global Positioning System (GPS), 1991.

[HAT91] R. HATCH. Instantaneous ambiguity resolution. In *International association of geodesy symposia 107 on kinematic systems in geodesy, surveying and remote sensing, New York*, 1991.

[HE94] R. HATCH and H. EULER. Comparison of several AROF techniques. In *Proceedings of ION GPS-94, Salt Lake City*, 1994.

[HE95] G. HEIN and B. EISSFELLER. Gnss2 Mission Analysis Study (Integrity). Technical report, Institute of Geodesy and Navigation (IfEN), University FAF Munich, September 14 1995.

[HOL81] J. HOLMES. *Coherent Spread Spectrum Systems*. Wiley-Interscience, 1981.

[HW95a] G. HEIN and W. WERNER. Comparison of Different On-The-Fly Ambiguity Resolution Techniques. In *Proceedings of ION GPS-95, Palm Springs*, September 1995.

[HW95b] G. HEIN and W. WERNER. Comparison of Different On-The-Fly Ambiguity Resolution Techniques. In *Proceedings of ION GPS-95, The Institute of Navigation, Palm Springs, September 12-15*, 1995.

[HWLC93] B. HOFMANN-WELLENHOF, H. LICHTENEGGER, and J. COLLINS. *Global Positioning System: Theory and Practice*. Springer-Verlag, 1993.

[ICA85] ICAO. *Rules of the Air and Air Traffic Services*. ICAO, twelfth edition, doc 4444-rac/501 edition, 1985.

[ICA92] ICAO. *Meteorological Service for International Air Navigation: Annex 3 to the Convention on International Civil Aviation*. ICAO, eleventh edition edition, 1992.

[ICA94a] ICAO. *Manual on Required Navigation Performance (RNP)*. ICAO, doc 9613-an/937 edition, 1994.

[ICA94b] ICAO All Weather Operations Panel. *Fifteenth Meeting of the ICAO All Weather Operations Panel, 26 September - 12 October*, 1994.

[ICA96] ICAO. *Aeronautical Telecommunications: Annex 10 to the Convention on International Civil Aviation*. ICAO, volume 1, fifth edition edition, July 1996.

[ICA97] ICAO. *Global Navigation Satellite System Panel Working Groups meeting in Brussels*, October 1997.

[JLN89] H. JANES, R. LANGLEY, and S. NEWBY. A Comparison of Several Models for the Prediction of Tropospheric Propagation Delay. In *proceedings of Fifth Geodetic Symposium on Satellite Positioning, Las Cruces, New Mexico*, March 1989.

[JLN91] H. JANES, R. LANGLEY, and S. NEWBY. Analysis of Tropospheric Delay Prediction Models: Comparisons with ray-tracing and Implications for GPS Relative Positioning. *Bulletin Géodésique*, 65:151–161, 1991.

[KLO96] J. KLOBUCHAR. *Global Positioning System: Theory and Applications*, volume 1, chapter 'Ionospheric Effects on GPS', pages 485–515. AIAA, 1996.

[LCL92] G. LACHAPELLE, M.E. CANNON, and G. LU. High precision GPS navigation with emphasis on carrier-phase ambiguity resolution. *Marine Geodesy*, 15(4):253–269, 1992.

[LE92] H. LANDAU and H.J. EULER. On-the-fly ambiguity resolution for precise differential positioning. In *Proceedings of ION-GPS-92, Albuquerque, The Institute of navigation, Alexandria, VA*, pages 607–613, 1992.

[LEI95] A. LEICK. *GPS Satellite Surveying*. Wiley-Interscience, 2nd edition, 1995.

[LL92] G. LU and G. LACHAPELLE. Statistical Quality Control for Kinematic GPS Positioning. *Manuscripta Geodaetica*, 17:270–281, 1992.

[MAC95] C. MACABIAU. Maximum A Posteriori GPS Phase Ambiguity Search Method. In *Proceedings of ION GPS-95, Palm Springs, The Institue Of Navigation, Alexandria, VA*, 1995.

[MAC96] C. MACABIAU. Comparison of the LSAST and MAPAS methods for ambiguity resolution on-the-fly. In *Proceedings of the DSNS-96 conference, Russian Institute of Radionavigation and Time, Saint Petersburg, may 20-24*, volume 2, 1996.

[MAD92] G. MADER. Kinematic GPS phase initialization using the ambiguity function. In *6th International Geodetic Symposium on Global Positioning Systems in Geosciences, Columbus*, pages 712–719, 1992.

[MB96] C. MACABIAU and A. BENHALLAM. Analysis of the Error Probability and Stopping Time of the MAPAS Procedure. In *Proceedings of ION GPS-96, Kansas City, The Institute of navigation, Alexandria, VA, sept 17-20*, 1996.

[MB97] C. MACABIAU and A. BENHALLAM. Practical Evaluation of Performance of MAPAS for Application to Precision Landings. In *Proceedings of ION GPS-97, Kansas City, The Institute of navigation, Alexandria, VA, sept 16-19*, 1997.

[MBJ+97] C. MACABIAU, A. BENHALLAM, J-L. JONQUIERE, G. ALCOUFFE, and S. MAZOYER. Analysis of Characteristics of GPS AROF Procedures for Application to Precision Landings. In *Proceedings of GNSS-97, Munich, April 21-25*, 1997.

[MCL95] V. MENDES, J. COLLINS, and R. LANGLEY. The Effect of Tropospheric Propagation Delay Errors in Airborne GPS Precision Positioning. In *proceedings of ION GPS-95, Palm Springs*, September 12-15 1995.

[NAT93] NATO. *STANAG 4294*, première edition, Aout 1993.

[NIK94] I. NIKIFOROV. On the First-Order Optimality of an Algorithm for Detection of a Fault in the Vector Case. *Automation and Remote Control*, 55:68–82, 1994.

[NN95] NAPA and NRC. Charting the Future. Technical report, NAPA and NRC, may 1995.

[NVK93] I. NIKIFOROV, V. VARAVVA, and V. KIREICHIKOV. Application of Statistical Fault Detection Algorithms to Navigation Systems Monitoring. *Automatica*, 29(5):1275–1290, 1993.

[PAG54] E. PAGE. Continuous Inspection Schemes. *Biometrika*, 41:100–115, 1954.

[PKLJ97] C. PARK, I. KIM, J. LEE, and G. JEE. Efficient technique to fix GPS carrier phase integer ambiguity on-the-fly. *IEE proceedings on Radar, Sonar and Navigation*, 144(3):148–155, June 1997.

[POO94] H. POOR. *An Introduction to Signal Detection and Eestimation*. Springer-Verlag, 1994.

[PSAE96] B. PARKINSON, J. SPILKER, P. AXELRAD, and P. ENGE. *Global Positioning System: Theory and Applications*. AIAA, 1996.

[REM84] B. REMONDI. *Using the Global Positioning System (GPS) phase observable for relative geodesy: modeling, processing, and results*. PhD thesis, University of Texas at Austin, mai 1984.

[REM91] B. REMONDI. Pseudo-kinematic GPS Results Using the Ambiguity Function Method. *Journal of the Institute of Navigation*, 38(1):17–36, 1991.

[ROC88] C. ROCKEN. *The Global Positioning System: A New Tool for Tectonic Studies*. PhD thesis, University of Colorado, 1988.

[SAA73] J. SAASTAMOINEN. Contributions to the Theory of Atmospheric Refraction. *Bulletin Géodésique*, 107:13–34, 1973.

[SAL97] G. SALUT. Personal conversations with the author. May 1997.

[SPI96a] J. SPILKER. *Global Positioning System: Theory and Applications*, volume 1, chapter 'Signal Structure and Theoretical Performance', pages 57–119. AIAA, 1996.

[SPI96b] J. SPILKER. *Global Positioning System: Theory and Applications*, volume 1, chapter 'Tropospheric Effects on GPS', pages 515–545. AIAA, 1996.

[TEU94] P. TEUNISSEN. A New Method for Fast Carrier Phase Ambiguity Estimation. In *Proceedings of IEEE PLANS-94, Las Vegas, NEVADA*, April 1994.

[TRE68] H. VAN TREES. *Detection, Eestimation, and Modulation Theory*. Wiley, 1968.

[VK96] V. VARAVVA and V. KIREICHIKOV. DSNS Cycle Slips Detection Based on Statistical Change Detection Algorithm. In *5th Conference on Differential Satellite Navigation Systems, St petersburg*, pages 1–5, 1996.

[WDR95] D. WALSH, P. DALY, and T. ROWE. An Analysis of Using Carrier Phase to Fulfill Cat III Required Navigation Performance. In *Proceedings of ION GPS-95, Palm Springs*, September 1995.

[WOO82] M. WOODROOFE. *Non Linear renewal Theory in Sequential Analysis*. SIAM Books, 1982.

[WS95] M. WEI and K-P. SCHWARZ. Fast Ambiguity Resolution Using an Integer Non Linear Programming Method. In *Proceedings of ION GPS-95, Palm Springs, The Institute of Navigation, Alexandria, VA*, 1995.

[XIA92] R. XIA. Determination of Absolute Ionospheric Error Using a Single Frequency GPS Receiver. In *proceedings of ION GPS-92, Albuquerque, New Mexico*, September 1992.

[ZB96] J. ZUMBERGE and W. BERTIGER. *Global Positioning System: Theory and Applications*, volume 1, chapter 'Ephemeris and Clock Navigation Message Accuracy', pages 585–599. AIAA, 1996.